SENSING, DESIGN OPTIMIZATION, AND MOTION PLANNING FOR AGILE PNEUMATIC ARTIFICIAL MUSCLE-DRIVEN ROBOTS

A Dissertation
Presented to
The Academic Faculty

By

Lucas Tiziani

In Partial Fulfillment
of the Requirements for the Degree
Doctor of Philosophy in the
School of Mechanical Engineering

Georgia Institute of Technology

August 2021

SENSING, DESIGN OPTIMIZATION, AND MOTION PLANNING FOR AGILE PNEUMATIC ARTIFICIAL MUSCLE-DRIVEN ROBOTS

Thesis committee:

Dr. Frank L. Hammond III
School of Mechanical Engineering & Dept. of Biomedical Engineering
Georgia Institute of Technology

Dr. Jun Ueda
School of Mechanical Engineering
Georgia Institute of Technology

Dr. Frank Dellaert
College of Computing
Georgia Institute of Technology

Dr. Aaron Young
School of Mechanical Engineering & Dept. of Biomedical Engineering
Georgia Institute of Technology

Dr. Daniel Goldman
School of Physics
Georgia Institute of Technology

Date approved: June 10, 2021

ACKNOWLEDGMENTS

I would like to first thank my advisor, Dr. Frank Hammond, for his guidance and mentorship over the last six years, from before we even had a lab space. Thank you to Dr. Frank Dellaert for encouraging me to examine this research from an alternative perspective. Thanks to Dr. Aaron Young for his support on both research and teaching and for reminding me to always consider the broader context of my work. And to my other committee members, Dr. Daniel Goldman and Dr. Jun Ueda, I thank them for their insight and advice throughout this research. To my labmates, thank you for countless brainstorming sessions and for scrutinizing my approach every step of the way—this undoubtedly strengthened my work. Thanks to Jeff Ward for his tireless effort on the knee exoskeleton design and across many other projects. Thank you to Yetong Zhang for his close collaboration throughout the trajectory optimization work that was critical to this thesis. Finally, I owe a special thank you to my parents for their support throughout my studies.

TABLE OF CONTENTS

Acknowledgments iii

List of Tables vii

List of Figures viii

Summary xv

Chapter 1: Introduction 1

Chapter 2: Liquid Metal Strain Sensor 6

2.1 Methodology 7
2.1.1 Design and fabrication 8
2.1.2 Sensorized muscle characterization & calibration 11
2.2 Experiments and Results 15
2.2.1 Static force experiment 16
2.2.2 Joint stiffness experiment 17
2.3 Discussion 18
2.4 Significance 19

Chapter 3: Optical Reflectance Sensor 21

3.1 Methodology 22
3.1.1 Design and fabrication 22
3.1.2 Control and data acquisition 28
3.1.3 Sensorized muscle characterization 29
3.1.4 Sensorized muscle calibration 32
3.2 Experiments and Results 33
3.2.1 Kinematics estimation experiments. 37
3.2.2 Dynamics estimation experiments. 39
3.2.3 Sensor disturbance experiment 44

3.3 Discussion . . . 46
3.3.1 Simplifications . . . 46
3.3.2 Potential issues . . . 47
3.3.3 Observations . . . 48
3.4 Significance . . . 50

Chapter 4: Muscle-Driven Robot Modeling and Control . . . 52

4.1 Pressure control strategy . . . 53
4.2 Pneumatic system dynamics . . . 54
4.3 Muscle dynamics . . . 62
4.4 Rigid body dynamics . . . 65
4.5 Discussion . . . 68
4.6 Significance . . . 68

Chapter 5: Jumping Robot Trajectory Optimization . . . 69

5.1 Methodology . . . 72
5.1.1 Factor graph framework . . . 72
5.1.2 Multi-phase trajectory optimization . . . 73
5.1.3 Robot dynamics . . . 76
5.1.4 Joint torque dynamics . . . 76
5.2 Experiments and Results . . . 80
5.3 Discussion . . . 85
5.4 Significance . . . 89

Chapter 6: Design Optimization Insights & Future Directions . . . 92

6.1 Knee Exoskeleton Case Study . . . 96
6.2 Methodology . . . 98
6.2.1 Variable moment arm . . . 99
6.2.2 Series elasticity . . . 102
6.3 Experiments and Results . . . 103
6.3.1 Series elasticity . . . 103
6.3.2 Angle-dependent moment arm optimization . . . 110
6.3.3 Combined optimization . . . 119
6.4 Discussion . . . 119
6.5 Significance . . . 123

Chapter 7: Conclusion . . . 124

7.1 Research contributions . . . 124
7.2 Application of pneumatic muscles . . . 127
7.3 Summary . . . 129

Appendices 131

Appendix A: Jumping Robot Simulation Description File 132

References 137

LIST OF TABLES

3.1 Surface fit metrics for muscle length and force versus optical sensor data. 34

3.2 Optical sensor end-effector position estimation error statistics for elliptical trajectories at three speeds with 10 trials at each speed. . . . 40

3.3 Static force experimental results: optical sensor joint torque and end-effector force estimation error statistics for experiment 1 (commanded displacement) and experiment 2 (fixed antagonist pressure). 44

3.4 Effects of 2- and 4-Newton external disturbances on sensorized muscle length estimation: deviation from nominal contraction length estimate (mm) at three locations along muscle. 46

3.5 Effects of 2- and 4-Newton external disturbances on sensorized force length estimation: deviation from nominal contraction force estimate (N) at three locations along muscle. 46

4.1 Muscle volume polynomial coefficients for 'mesh' muscle design. . . . 60

5.1 Jumping robot link masses. 72

5.2 Average RMS error between simulated and experimental joint data over three trials for each target jump height. 86

5.3 Average error between simulated and experimental trajectories over three trials for each target jump height. 86

6.1 Optimal hip and knee cam parameters for maximum jump height. . . 111

LIST OF FIGURES

1.1 Pneumatic artificial muscle: vented muscle at nominal length (top), inflated muscle near max contraction length (bottom). 2

2.1 **(a)** Pneumatic artificial muscle with radial EGaIn liquid metal strain sensor; **(b)** section view of muscle showing axial EGaIn sensor. Large spacing is used between muscle constraining threads (yellow). 9

2.2 Sensor fabrication process: **(a)** cast two sensor layers; **(b)** bond layers, inject with EGaIn, and cast in cylindrical mold. For radial sensor, **(c)** bond sensor ends with silicone in mold. **(d)** Radial sensor band. . . . 10

2.3 Pneumatic muscle fabrication process: **(a)** cast half-thickness silicone bladder with embedded end plug, **(b)** wrap bladder with Kevlar threads, **(c)** cast second layer of silicone onto bladder to encapsulate Kevlar fibers, **(d)** add sensor and end plug. 11

2.4 Pressure control schematic: blue lines represent fluidic connections, green lines represent signal connections, and black lines represent power connections. 12

2.5 Pneumatic muscle blocked force data: third-order polynomial curves fit to raw data. 13

2.6 Pneumatic muscle prototype sensor characterization: **(a)** muscle contraction and **(b)** corresponding axial sensor response; **(c)** diametral expansion and **(d)** corresponding radial sensor response. 14

2.7 Third-order calibration curves for axial sensor-muscle contraction and radial sensor-diametral expansion. 15

2.8 Muscle diametral expansion versus pressure for a range of fixed muscle contraction lengths. 16

2.9 One degree-of-freedom experimental test setup actuated by an antagonistic pair of pneumatic muscles with EGaIn liquid metal sensors. . 16

2.10 Sensor-estimated end-effector force versus ground truth measurement for **(a)** 0 deg linkage angle and **(b)** 10 deg linkage angle. 17

2.11 (a) Sensor-estimated end-effector force (circle marker) versus ground truth measurement (line) for 0 deg initial linkage angle; estimates are averages between two antagonistic muscles. (b) Sensor-estimated muscle pressures (circle marker for extension muscle, x marker for contraction muscle) versus controlled pressure (line). 18

2.12 Sensor-estimated end-effector force (circle marker) versus ground truth measurement (line) for 5 deg initial linkage angle linkage angles; estimates are averages between two antagonistic muscles. 19

3.1 Optical length and pressure sensor assemblies for integration with pneumatic artificial muscle: **(a)** cross-section of muscle showing locations of sensor assemblies; **(b)** length sensor end cap assembly; **(c)** pressure sensor end cap assembly; **(d)** sensor circuit board. 23

3.2 Operating principle of optical sensors: red represents IR light emitted by LED and blue represents IR light reflected by diaphragm back to photodiode. **(a)** Unpressurized muscle with sealed diaphragm for pressure measurement and vented diaphragm for length measurement; **(b)** pressurized muscle showing sealed diaphragm deflected under pressure and vented diaphragm stretched/translated toward length sensor end cap. **(c)** Specular reflection by sealed diaphragm before muscle pressurization (top) and after pressurization (bottom); **(d)** diffuse reflection by vented diagram before muscle pressurization (top) and after pressurization (bottom). 24

3.3 Fabrication steps for sensorized pneumatic artificial muscle: **(1)** cast half-thickness muscle bladder with helical grooves for thread placement; **(2)** add end-connectors and wrap Kevlar threads; **(3)** cast second layer around bladder, encapsulating Kevlar threads at mid-bladder; **(4)** cast two-color vented diaphragm; **(5)** cast one-color sealed diaphragm; **(6)** add end caps and seal length sensor end cap in place. 27

3.4 Pressure control and data acquisition schematic: blue lines represent fluidic connections, green lines represent signal connections, and black lines represent power connections. 30

3.5 Optical sensor characterization for 10 muscle actuation cycles: **(a)** test setup with muscle fixed at one end; **(b)** muscle pressure versus optical pressure sensor voltage for single muscle; **(c)** muscle contraction length versus optical length sensor voltage for single muscle; **(d, e)** comparison of optical sensor data for four muscles with 10-cycle data for each muscle fit to a third-order polynomial—solid lines represent inflation, whereas dashed lines represent deflation. 31

3.6 Blocked force testing: **(a)** test setup with muscle fixed at one end and connected to the Instron crosshead at the other; **(b)** muscle contraction force versus contraction length at fixed pressures between 5 and 55 kPa for four muscles. 33

3.7 Optical sensor length calibration: muscle contraction length versus optical sensor voltages with polynomial surface fit for muscle length estimation. 34

3.8 Optical sensor force calibration: muscle contraction force versus optical sensor voltages with polynomial surface fit for muscle force estimation. 34

3.9 Two degree-of-freedom arm evaluation platform with two antagonistic pairs of sensorized pneumatic artificial muscles. 35

3.10 Optical sensor-estimated and true positions of two-DOF arm end-effector for 16 points in workspace over 10 trials; nominal arm configuration is shown in gray. 38

3.11 Optical sensor-estimated versus true end-effector location and joint angles for open-loop elliptical trajectory at three different end-effector speeds. 39

3.12 Static force experiment 1 results for 10 trials at left end-effector location: estimated versus true joint torques and end-effector forces for 20 cm commanded displacement input. 41

3.13 Static force experiment 2 results for 10 trials at left end-effector location: estimated versus true joint torques and end-effector forces for agonist muscle pressure ramp input (fixed antagonist pressure). . . . 43

3.14 Dynamic force experimental results for 2-DOF arm: **(a)** estimated versus true joint torques and **(b)** estimated versus true end-effector forces, where solid lines represent filtered data; **(c)** corresponding end-effector trajectory in shaded workspace moving from light to dark. . . 45

4.1 Pneumatic muscle-drive robot system dynamics. 52

4.2 Air pressure/density ratio versus pressure. 58

4.3 Air density and viscosity versus pressure. 59

4.4 Muscle volume versus muscle contraction for mesh muscle: experimentally-measured data and third-order polynomial fit. 60

4.5 Pneumatic muscle pressure step response: simplified tube pressure drop model vs. MATLAB Pipe model. 62

4.6 Pneumatic muscle pressure step response comparing experimental data (circle markers) to MATLAB Pipe model (dashed line) and custom model (solid line): **(a)** nominal tube diameter, **(b)** tube diameter reduced by 0.03 in. 63

4.7 Third-order surface fit to pneumatic muscle blocked force versus pressure and contraction data. 65

5.1 Planar two-legged jumping robot test platform. 71

5.2 Factor graph representing the jumping robot vertical jump trajectory, formulated as a multi-phase optimization problem using hybrid direct collocation: the first phase (Δt_1) represents the jumping robot dynamics with both feet in contact with the ground, while the second phase represents the aerial jumping robot dynamics. 74

5.3 Rigid body dynamics representation of the jumping robot in a factor graph. The red factors are active when the corresponding robot foot is in contact with the ground: pose, twist, and acceleration constraints enforce fixed foot position (point contact); wrench constraints enforce no torque transmission from the ground to the foot. The blue factors are active for the aerial phase and enforce zero interaction wrench between the foot and the ground. 77

5.4 Joint torque sub-factor graph, from left to right: the pneumatic source tank state (blue), shared by all joint torque sub-graphs; the airflow dynamics constraint between the source tank and pneumatic muscle; the pneumatic muscle state; and the constraints between muscle force/joint torque and robot state. 77

5.5 Use of sigmoids to smoothly connect valve open/close airflow dynamics: **(a)** large c_o and c_c resulting in smoother change between sets of dynamics, **(b)** small c_o and c_c resulting in faster change between sets of dynamics. 79

5.6 Comparison of robot poses in simulated and real jumps at multiple times throughout 0.2-m target jump (1.5-m torso height). 82

5.7 Comparison of simulated and real jumps for 0.2-m target jump height: **(a)** Pneumatic muscle pressures, **(b)** robot joint angles. Circle markers represent experimental data and solid/dashed lines represent simulation data—note that simulated pressures and angles are symmetric on the right and left legs, so simulated data for knee joints and hip joints, respectively, overlap. 82

5.8 Comparison of robot torso trajectory in real and simulated jumps for 0.2-m target jump; circle markers represent experimental data and solid/dashed lines represent simulation data. 83

5.9 Comparison of robot poses in simulated and real jumps at multiple times throughout 0.4-m target jump (1.5-m torso height). 84

5.10 Comparison of simulated and real jumps for 0.4-m target jump height: **(a)** Pneumatic muscle pressures, **(b)** robot joint angles. Circle markers represent experimental data and solid/dashed lines represent simulation data—note that simulated pressures and angles are symmetric on the right and left legs, so simulated data for knee joints and hip joints, respectively, overlap. 84

5.11 Comparison of robot torso trajectory in real and simulated jumps for 0.4-m target jump; circle markers represent experimental data and solid/dashed lines represent simulation data. 85

6.1 **(a)** Active (left), passive (right), and total (blue) biological muscle force-length curves, where $\tilde{l}^M$ is the muscle length at which the muscle develops peak isometric active force $\tilde{f}^M$; **(b)** biological muscle force-velocity curve, where $\tilde{v}^M$ is the muscle lengthening velocity [89]. . . . 93

6.2 Pneumatic artificial muscle force-length curve. 94

6.3 **(a)** Bilateral pneumatic knee exoskeleton; **(b)** exoskeleton knee assistance force profile. 96

6.4 Assistance torque versus knee flexion angle comparing 5-cm pulley and lever arm configurations: **(a)** 5-cm lever arm at various mounting angles; **(b)** various lever arm lengths at 0-deg mounting angle. 98

6.5 Muscle-cam geometry parameters. 99

6.6 (a) Cam moment arm solution for ϕ less than ϕ_{min}; (b) cam moment arm solution for ϕ greater than ϕ_{max}. 101

6.7 Jump height contour plot for varied hip and knee tendon stiffnesses: increasing jump height from dark to light; blue marker indicates maximum jump height. 104

6.8 Comparison of robot joint dynamics for jump with stiff joint tendons versus jump with compliant tendons: **(a)** knee muscle contraction, **(b)** knee muscle volume, **(c)** knee muscle pressure, **(d)** knee muscle force. Solid lines represent knee joint and dashed lines represent hip joint; vertical lines represent foot liftoff times 105

6.9 Comparison of robot center-of-mass power for jump with stiff joint tendons versus jump with compliant tendons. Vertical lines represent foot liftoff times. 106

6.10 Jump height versus hip muscle activation offset time for 10 kN/cm tendon stiffness. 106

6.11 Comparison of robot joint dynamics for jump with hip activation 50 ms before knee activation versus jump with simultaneous hip and knee activation at time zero, both with stiff tendons: **(a)** joint angle, **(b)** linear displacement, **(c)** muscle pressure, **(d)** muscle force. Solid lines represent knee joint and dashed lines represent hip joint; vertical lines represent foot liftoff times. 107

6.12 Comparison of robot joint dynamics for jump with knee activation 50 ms before hip activation versus jump with simultaneous hip and knee activation at time zero, both with stiff tendons: **(a)** joint angle, **(b)** linear displacement, **(c)** muscle pressure, **(d)** muscle force. Solid lines represent knee joint and dashed lines represent hip joint; vertical lines represent foot liftoff times. 108

6.13 Comparison of robot center-of-mass power: **(a)** jump with hip activation 50 ms before knee activation versus jump with simultaneous hip and knee activation at time zero; **(a)** jump with knee activation 50 ms before hip activation vs jump with simultaneous activation. Vertical lines represent foot liftoff times. 109

6.14 Jump height versus hip muscle activation offset time for true robot tendon stiffnesses. 110

6.15 Jump height versus pulley radius, with the same pulley for both hip and knee joints. 111

6.16 Comparison of robot joint dynamics for jump with 4.5-cm pulleys versus jump with optimized cams: **(a)** joint angle, **(b)** muscle contraction, **(c)** muscle pressure, **(d)** muscle volume, **(e)** muscle force, **(f)** joint torque. Solid lines represent knee joint and dashed lines represent hip joint; vertical lines represent foot liftoff times. 112

6.17 Comparison of robot center-of-mass power for jump with 4.5-cm pulleys versus jump with optimized cams. Vertical lines represent foot liftoff times. 113

6.18 Comparison of robot joint dynamics for jumps with pulleys versus optimized cams, with 2x-length muscles: **(a)** joint angle, **(b)** muscle contraction, **(c)** muscle pressure, **(d)** muscle volume, **(e)** muscle force, **(f)** joint torque. Solid lines represent knee joint and dashed lines represent hip joint; vertical lines represent foot liftoff times. 114

6.19 Comparison of robot center-of-mass power for jumps with pulleys versus optimized cams, with 2x-length muscles. Vertical lines represent foot liftoff times. 115

6.20 Comparison of robot joint dynamics for jump with 2x-length muscles versus jump with nominal-length muscles: **(a)** joint angle, **(b)** muscle contraction, **(c)** muscle pressure, **(d)** muscle volume, **(e)** muscle force, **(f)** joint torque. Solid lines represent knee joint and dashed lines represent hip joint; vertical lines represent foot liftoff times. . . . 117

6.21 Comparison of robot center-of-mass power for jump with 2x-length muscles versus jump with nominal-length muscles. Vertical lines represent foot liftoff times. 118

SUMMARY

Mechanical compliance in robotic systems facilitates safe human-robot interaction and improves robot adaptation to environmental uncertainty. Several promising compliant actuator technologies have emerged from the field of soft robotics, in particular the pneumatic artificial muscle—a soft, lightweight actuator that contracts under pressure. The pneumatic muscle's passive compliance eliminates the need for precise high-bandwidth actuator control to simulate mechanical impedance. However, the pneumatic muscle is limited in practical robot applications—particularly, without sacrificing robot agility—due to several key challenges: development of compatible soft sensors, translation of conventional high-level control and planning techniques to pneumatic muscle-driven systems, and limitations in pneumatic muscle pressurization rate and force generation capabilities.

This work seeks to address these challenges, via a threefold approach, to access the benefits of compliant robot actuation while maximizing the robot's dynamic capabilities. The first objective targets the development of a pneumatic muscle design with integrated sensing to enable kinematic and dynamic state estimation of muscle-actuated robots without hindering muscle compliance. The second objective focuses on the construction of a trajectory optimization framework for planning dynamic robot maneuvers using 'burst-inflation' muscle pressure control. Finally, the third objective explores a design optimization strategy utilizing biological joint mechanisms to compensate for pneumatic muscle limitations and maximize robot agility.

CHAPTER 1
INTRODUCTION

Soft robotics is an emergent research area within the robotics field that promises safer and more robust solutions to challenges in human and machine mobility. Traditionally, roboticists devise sophisticated strategies relying on precise sensing to control rigid motor-driven robots in an attempt to simulate animal-like flexibility and grant robots a gentler touch. Conversely, soft robotics seeks to build mechanical intelligence into robots using soft, flexible, and lightweight materials (like those found in living organisms) that adapt to humans and their surroundings. In this way, soft robotics enables simpler control, safer human-robot interaction, and increased resilience in uncertain environments.

This work focuses on coupling one of the most well-known soft robot actuators—the pneumatic artificial muscle—with rigid structures to enhance robot adaptability while maintaining some of the advantages of traditional robotic systems, namely, high force transmission capabilities and robust rigid body dynamics modeling techniques. The pneumatic artificial muscle is a low-mass linear actuator composed of an elastomeric bladder constrained by helically-wrapped fibers that contracts up to thirty percent when pressurized, as shown in Figure 1.1. A single muscle or an antagonistic pair can be connected to a pulley or lever arm to actuate a hinge joint (replacing an electric motor), providing mechanical compliance with high torque capability. Consider the benefits of soft actuation in the following applications:

1. Inherent safe contact dynamics: an assistive mobile manipulator with a **flexible robot arm** to help physically-impaired individuals with activities of daily living, like feeding and dressing. The low mass of pneumatic muscles significantly reduces arm inertia, lessening the consequences of collisions, while the intrinsic

compliance facilitates safe physical interaction between human and robot.

2. Biomechanical compatibility: a **lower-body exoskeleton** that provides assistance at the knee joint to reduce metabolic cost during locomotion while carrying a heavy load. The compliant actuators used on this device apply smooth, biologically-similar assistive forces that safely and comfortably augment the user's leg muscles. Replacing motors and gearboxes with pneumatic muscles also allows for a substantial reduction in distal mass along the leg, which, in a wearable device, can reduce user fatigue during prolonged use.

3. Environmental adaptation: a **legged exploration robot** designed to navigate challenging and hazardous environments with irregular terrain and unpredictable obstacles. In these settings, legs significantly improve robot mobility versus wheels, but are more difficult to control: each step must be carefully planned to ensure robot stability. With soft actuators built into each leg, however, the robot can exploit leg compliance to mechanically adapt to the terrain rather than rely on complex control algorithms.

Figure 1.1: Pneumatic artificial muscle: vented muscle at nominal length (top), inflated muscle near max contraction length (bottom).

While the morphological approach to robot adaptation illustrated in these three examples has been shown effective for simple systems, soft robot technologies are still quite limited in practical applications. The most substantial challenges are: compatible soft sensing technologies, limitations in soft actuator speed and force generation capabilities, and application of conventional robot planning and high-level control

techniques to soft robotic systems [1]–[6]. Consequently, this thesis seeks to ***improve the performance of pneumatic muscle-driven robots, specifically to enable the fast dynamics capabilities required in assisted human locomotion and for propulsion of human-scale legged mobile robots***. A threefold approach is taken to address these challenges:

1. **Objective 1:** Develop a pneumatic muscle design with integrated sensing to enable kinematic and dynamic state estimation of muscle-driven robots without sacrificing the muscle's compliant nature.

2. **Objective 2:** Develop a modeling approach for pneumatic muscle-driving rigid body robots using a combination of analytical and data-driven models. Incorporate this model into a trajectory optimization framework for planning dynamic robot motions that can be executed on a real robot with pneumatic control hardware suited for mobile systems.

3. **Objective 3:** Investigate the use of biologically-inspired joint mechanisms to maximize robot performance by compensating for pneumatic muscle limitations in force versus contraction length and inflation speed.

This thesis addresses the three objectives over the next five chapters, further motivating each objective by examining the current state-of-the-art in the field. Chapter 2 outlines pneumatic muscle sensing technologies that have previously been investigated, highlighting the lack of combined position and force sensing capabilities. The design of a pneumatic muscle with integrated room-temperature liquid metal strain sensors for muscle length and contraction force estimation is then detailed and sensorized muscle performance is evaluated on a single degree-of-freedom (DOF) linkage. The deficiencies of this sensing approach spur the development of a novel optical reflectance sensor in Chapter 3. The optical sensors are integrated into a new pneumatic muscle design for improved kinematic and dynamic muscle state estimation.

Two antagonistic pairs of sensorized muscles are configured on a planar 2-DOF arm to evaluate sensing performance.

In chapter 4, a complete pneumatic muscle-driven robot model is developed. The selection of 'burst inflation' robot control strategy is first explained, as this largely dictates pneumatic system dynamics. A range of techniques for modeling pneumatic system and muscle dynamics are then laid out, and an approach is chosen to balance model accuracy with simplicity. Additionally, the formulation of rigid body dynamics used in this work is reviewed. The muscle-driven robot model laid out in this section is utilized in the subsequent chapters for trajectory planning and design optimization.

Chapter 5 builds a trajectory optimization framework for pneumatic muscle-driven robot motion planning using factor graphs. The pneumatic system, muscle, and rigid body models are incorporated into a robot trajectory factor graph as constraint factors and the graph is solved to calculate the valve open and close times that achieve a desired robot trajectory or target state. To evaluate this approach, a two-legged pneumatic muscle-driven jumping robot is designed and fabricated. A trajectory factor graph is constructed for the jumping robot and used to plan a range of vertical jumps. Pneumatic system dynamics and robot kinematics are then compared for simulated and experimental jumps run using optimized valve timing sequences.

In chapter 6, biological muscle force transmission mechanisms in animal jumping are reviewed: specifically, the effects of series elasticity (tendons) and joint angle-dependent mechanical advantage (resulting from musculoskeletal structure) on jumping biomechanics are considered. Inspired by animal morphology, this chapter investigates whether series elasticity and variable mechanical advantage can similarly improve the performance of pneumatic muscle-driven robots. A sequence of design optimizations are run for the jumping robot to characterize the impacts of series elasticity and joint angle-dependent moment arm on jump height; the study includes consideration for the interaction of pneumatic muscle activation timing and nominal

muscle length with stiffness and moment arm design parameters.

Finally, Chapter 7 summarizes the overall research contributions of this thesis and elucidates the context in which pneumatic muscles may be best utilized for mobile robotic systems. Significant conclusions and lessons learned are highlighted for each of the three objectives addressed in this work, and future research directions are laid out for pneumatic artificial muscle-driven robots.

CHAPTER 2
LIQUID METAL STRAIN SENSOR

For human-robot interaction applications, position and force sensing are critical to safe and robust robot control but are challenging to implement for soft robot actuators. Specifically, it is difficult to incorporate traditional position and force sensors without sacrificing the soft, compliant nature of the actuator. Thus, the first objective of this work is to develop and integrate compatible soft sensors into one of the most utilized soft actuators—the pneumatic artificial muscle—to provide compliant actuation with built-in kinematic and dynamic sensing capabilities.

Recent literature has explored various methods of integrating soft sensors directly into pneumatic muscles, including resistive sensors using conductive silicones, liquid metals, and braided threads [7]–[10], inductive sensors via conductive wires wrapped around muscles [11], [12], and optical sensors [13]. Most sensing methods focus on measuring muscle displacement and rely on external pressure transducers for approximating muscle force [12], [14], [15]. Alternatively, one group measured muscle pressure only, as a proxy to force output measurement [16]. However, there are several advantages to measuring both muscle length and pressure (or equivalently, length and force) via muscle-integrated sensing:

- The number of external sensors is reduced (no external pressure transducer), and less pneumatic connections are required, making it easier to incorporate sensing and actuation into robotic systems.

- Pressure measurement directly at the muscle is more temporally accurate than measurement via external transducers upstream that do not capture the transient pressure dynamics of downstream components. This is especially impor-

tant for fast robot dynamics with rapid muscle inflation, as well as for high-bandwidth force estimation.

While these benefits motivate the integration of both length and force sensing into pneumatic muscle designs, only one investigation was found in which both muscle contraction force and length were estimated from integrated sensing [17]. This was achieved by measuring the inductance and resistance of conductive wire braids woven around the muscle. The authors evaluated only position estimation on a 1-DOF system.

The approach detailed in this chapter seeks to achieve position and force sensing via the use of eutectic gallium indium (EGaIn) liquid metal sensing: two EGaIn sensors are incorporated into each muscle to measure both contraction and pressure [18]. While preliminary sensor results are promising, muscle force estimation accuracy suffers in practice due to poor pressure sensing resolution. Furthermore, several issues inherent to EGaIn sensors limit their potential outside of a laboratory setting, including complexity of sensor fabrication, oxidization of EGaIn causing sensor baseline drift over time, circuit disconnection at the EGaIn-wire lead interface, and EGaIn leakage out of the sensor.

2.1 Methodology

A number of pneumatic bending actuator designs have demonstrated the use of room-temperature liquid metal strain sensors to measure actuator curvature [19]–[21]. Similarly, a pneumatic muscle was designed with a liquid metal-filled helical microchannel embedded in the muscle bladder to measure muscle contraction [9]; this helical microchannel design, along with several other non-liquid strain sensor concepts [8], [10], relies on the coupling between muscle length and diameter to infer length change from overall muscle expansion.

The sensorized muscle detailed here utilizes the liquid metal strain sensor to mea-

sure both muscle contraction and force [18]. Instead of estimating muscle contraction via muscle diameter, a linear strain sensor is enclosed inside the muscle along its axis to measure muscle length directly. To infer muscle force, a second strain sensor is wrapped around the outer circumference of the muscle, measuring the combination of overall muscle diameter and local muscle bladder deformation between muscle threads. By spacing the helically-wrapped threads that constrain muscle geometry further apart, the muscle bladder increasingly balloons out between threads as internal pressure is increased, such that muscle length and diameter are effectively decoupled. Muscle force can then be inferred from muscle pressure-length-force characterization data.

Design overview. The pneumatic artificial muscle design consists of a cylindrical silicone elastomer bladder embedded with Kevlar threads to constrain the motion of the bladder under pressure. The use of discrete threads—rather than the more typical woven thread mesh sleeved around the muscle bladder—allows for customizable thread spacing and orientation, as well as a reduction in friction between the constraining threads and the muscle bladder material. A eutectic gallium-indium (EGaIn) strain sensor wraps around the outer diameter of the bladder at the midpoint along the muscle axis to measure the radial bladder deformation (Figure 2.1a). A second EGaIn sensor is enclosed in the muscle bladder and positioned along the muscle's axis of contraction to measure length (Figure 2.1b). The use of both axial and radial sensors enables estimation of muscle length and pressure solely from muscle sensor data.

2.1.1 Design and fabrication

Axial sensor. The axial sensor inside the muscle is comprised of a 300-μm microchannel filled with EGaIn (Sigma-Aldrich Co.) that is encapsulated in an Ecoflex

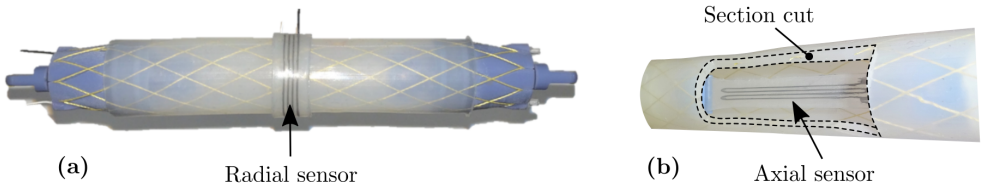

Figure 2.1: (a) Pneumatic artificial muscle with radial EGaIn liquid metal strain sensor; **(b)** section view of muscle showing axial EGaIn sensor. Large spacing is used between muscle constraining threads (yellow).

30 platinum-cure silicone substrate (Smooth-on Inc.). Ecoflex 30 has a low elastic modulus, minimizing the force required to strain the sensor; the maximum tensile force exerted by the axial sensor at the full length of the pneumatic muscle is 0.67 N.

The sensor is fabricated using conventional soft lithography techniques [22]: two silicone sheets are cast using 3D-printed molds; one of the molds contains a raised channel feature to imprint the channel geometry into the silicone sheet, while the other mold produces a flat sheet (Figure 2.2a). The two sheets are bonded using Sil-Poxy silicone adhesive (Smooth-on Inc.). Then, the embedded channel is filled with EGaIn via a hypodermic needle, and wire leads are attached to the ends of the channel (Figure 2.2b). 3D-printed grips with threaded features for connection inside the muscle are connected to both ends of the sensor. The nominal resistance of the axial sensor design, prior to being installed inside the muscle in a pre-strained state, is approximately 0.7 ohms.

Radial sensor. The radial sensor is fabricated in a manner similar to the axial sensor, with one additional step: after creating the sensor and filling its channel with EGaIn, the sensor is placed in a cylindrical mold and silicone is added to connect the ends of the sensor together (Figure 2.2c). This produces a cylindrical sensor band that fits snugly around the outer diameter of the pneumatic muscle. The nominal resistance of the radial sensor design is approximately 1 ohm.

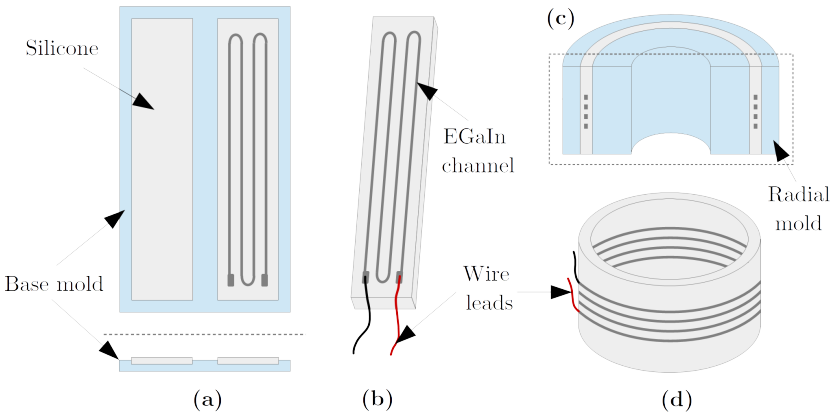

Figure 2.2: Sensor fabrication process: **(a)** cast two sensor layers; **(b)** bond layers, inject with EGaIn, and cast in cylindrical mold. For radial sensor, **(c)** bond sensor ends with silicone in mold. **(d)** Radial sensor band.

Pneumatic muscle. The pneumatic artificial muscles are fabricated over four steps, as shown in Figure 2.3, by casting Dragon Skin 10 SLOW platinum-cure silicone (Smooth-On Inc.) into 3D-printed molds (Objet30 Prime, Stratasys) and intermediately embedding structural components:

1. Silicone is injected into mold assembly 1 around a cylindrical inner mold to create a half-thickness muscle bladder (Figure 2.3a). As part of this step, one of the end plugs is embedded at one end of the muscle. Additionally, raised features on the inner surfaces of the outer molds created helical grooves on the outer surface of the bladder.

2. The helical grooves are then used for guidance in wrapping the Kevlar threads (0.36 mm diameter) around the muscle bladder (Figure 2.3b). Slots in the embedded end plug and in the base of the inner mold are used to constrain the threads. Eight threads each are added in the clockwise and counterclockwise directions, respectively, at $\pm$ 22° from the muscle axis. This angle was chosen to achieve a balance between axial contraction and radial expansion of the muscle [23].

3. A second layer of silicone is cast around the inner muscle bladder and Kevlar

threads, encapsulating the threads at the mid-thickness of the muscle outer wall (Figure 2.3c). Extra thread length at the free end of the muscle is tucked into an opening at the bottom of the inner mold so that the threads can be subsequently connected to the second end plug in step 4.

4. The axial sensor is connected inside the muscle; the sensor wires are routed through two passages in the end plug and the holes are sealed with Sil-Poxy. The extra Kevlar thread lengths from step 3 are connected to the second end plug and the plug is sealed into the open end of the muscle (Figure 2.3d). To securely fix the threads at both ends of the muscle, conical inserts are screwed into the tops of both end plugs

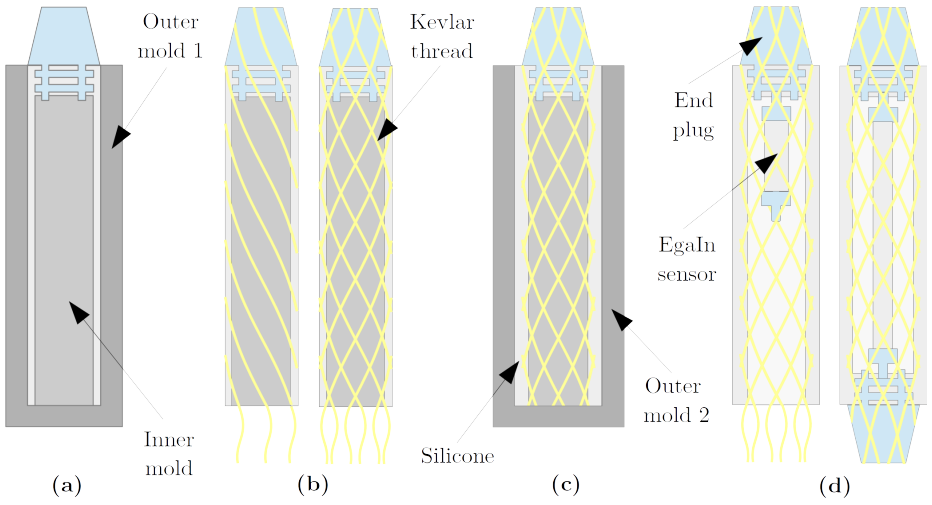

Figure 2.3: Pneumatic muscle fabrication process: **(a)** cast half-thickness silicone bladder with embedded end plug, **(b)** wrap bladder with Kevlar threads, **(c)** cast second layer of silicone onto bladder to encapsulate Kevlar fibers, **(d)** add sensor and end plug.

2.1.2 Sensorized muscle characterization & calibration

Control and data acquisition. For muscle and sensor characterization, as well as experimental evaluation in the subsequent section, pneumatic muscle pressure control was performed using solenoid valve pulse-width modulation to control airflow from

a diaphragm pump to the muscle (Figure 2.4). A proportional-derivative controller implemented on an Arduino MEGA 2560 was used to modulate the PWM duty cycle of the valve based on pressure transducer feedback and the desired pressure setpoint. The Soft Robotics Toolkit was used as a reference in selecting pump and valve components for the controller [24].

EGaIn sensor voltages were recorded via an NI myDAQ device (National Instruments Co.). Sensors were configured in a voltage divider circuit and the sensor voltage was amplified using an operational amplifier with a nominal gain of 470. Additionally, a capacitive filter was added to filter high frequency sensor noise.

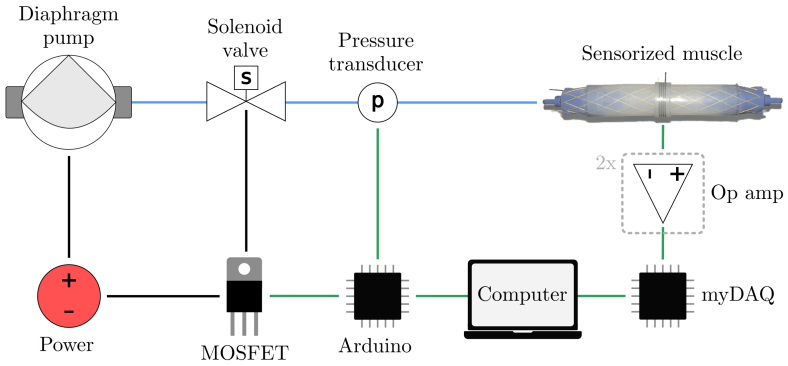

Figure 2.4: Pressure control schematic: blue lines represent fluidic connections, green lines represent signal connections, and black lines represent power connections.

Muscle characterization. Each pneumatic muscle was characterized over a set of blocked force tests, in which the muscle was fixed in an Instron electromechanical test frame and allowed to contract slowly under a fixed internal pressure. Tests were performed at pressures between 3.4 kPa (0.5 psi) and 41.4 kPa (6 psi), stepped by 3.4 kPa (0.5 psi) increments. Before each test, the muscle was connected to the Instron crosshead and the load cell was zeroed; the muscle was then preloaded to 0.44 N (0.1 lbf) in its unpressurized (maximum length) state to ensure all slack was removed. Throughout each run, the pressure controller maintained a constant pressure setpoint, while the Instron crosshead moved in the direction of muscle contraction at a rate

of 20 mm/minute. The test stopped when the applied force dropped below 0.44 N (0.1 lbf). The average peak force generated by this pneumatic muscle design at 41.4 kPa (6 psi) was 64.1 N (14.4 lbf). Across the four muscles tested, the maximum force variation was 5.8 N (1.3 lbf); blocked force results are shown in Figure 2.5.

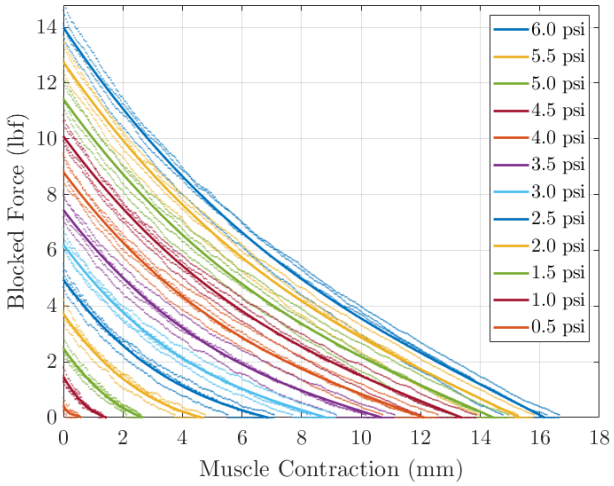

Figure 2.5: Pneumatic muscle blocked force data: third-order polynomial curves fit to raw data.

Sensor characterization. Sensor response was characterized over the full operating range of the pneumatic muscle. Each muscle was inflated from 0 to 55.2 kPa (8 psi) and deflated back to 0 kPa for ten cycles. Muscle length and diameter were measured at each pressure using fiducial markers attached to the muscle. The average axial contraction across all four muscles tested was approximately 16.7 mm, or 23% of the inner muscle length (average of 73.3 mm). The average radial expansion was 16.3 mm, or 81% of the outer muscle diameter. The average voltage change for the axial sensor across the entire contraction range for all four muscle prototypes was 1.6 V, while the average change for the radial sensor was 2.2 V. The muscle prototype in Figure 2.6 showed the smallest axial and radial sensor voltage ranges across all four muscles.

Additional testing was performed to determine the sensitivity of the axial sensor

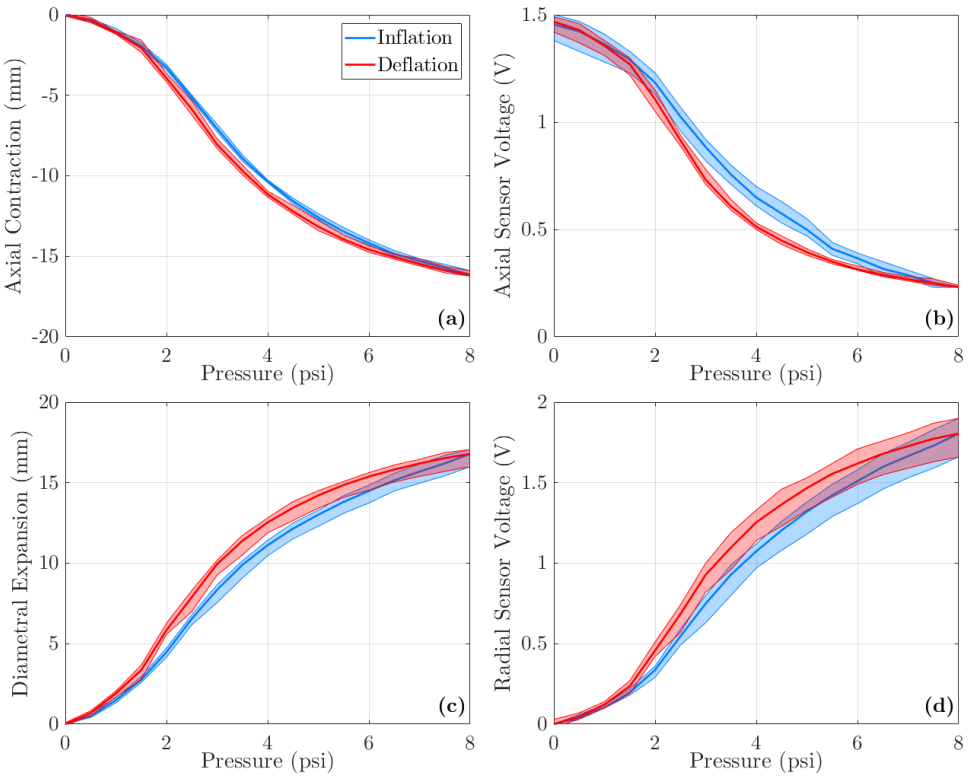

Figure 2.6: Pneumatic muscle prototype sensor characterization: **(a)** muscle contraction and **(b)** corresponding axial sensor response; **(c)** diametral expansion and **(d)** corresponding radial sensor response.

to ambient pressure inside the muscle. The axial sensor was electrically connected to a milliohm meter (GW Instek, Ltd.) and sealed inside a pressure vessel. The vessel was pressurized in 6.9 kPa (1 psi) increments up to 103 kPa (15 psi) and the sensor resistance was recorded at each pressure. Sensor resistance increased by only 0.007 ohms over the entire pressure range, about 1% above the nominal resistance.

Muscle length & force estimation. For each pneumatic muscle, third-order polynomial curves were fit to axial contraction versus axial sensor voltage data and diametral expansion versus radial sensor voltage data (Figure 2.7). The axial sensor curve allows for direct measurement of muscle length. Together, both sets of sensor characterization data allow for estimation of internal muscle pressure from contraction and diameter measurements, as shown in Figure 2.8. Then, muscle length and pressure

estimates can be used to estimate muscle contraction force from blocked force data (Figure 2.5).

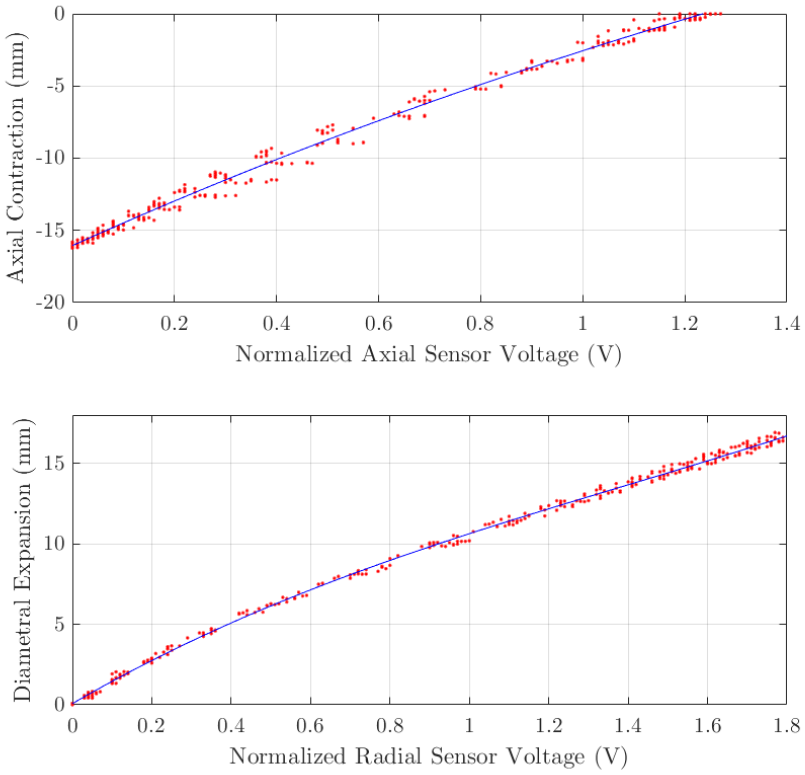

Figure 2.7: Third-order calibration curves for axial sensor-muscle contraction and radial sensor-diametral expansion.

2.2 Experiments and Results

To evaluate sensorized pneumatic muscle force estimation accuracy, experiments were performed with a single sensorized muscle and an antagonistic pair connected to a one degree-of-freedom hinge joint linkage. Axial and radial sensor data were used to estimate applied linkage end-effector force.

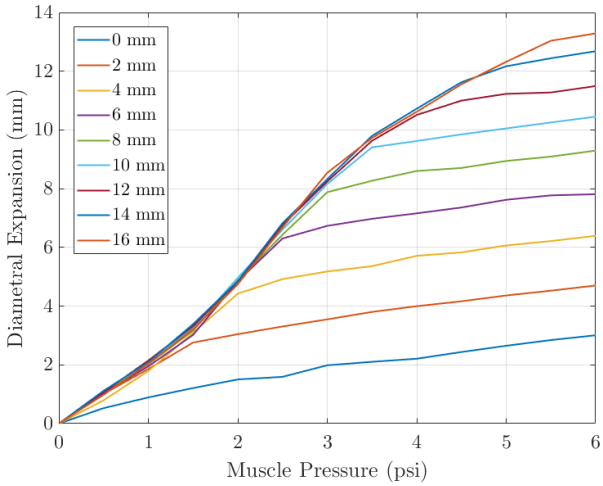

Figure 2.8: Muscle diametral expansion versus pressure for a range of fixed muscle contraction lengths.

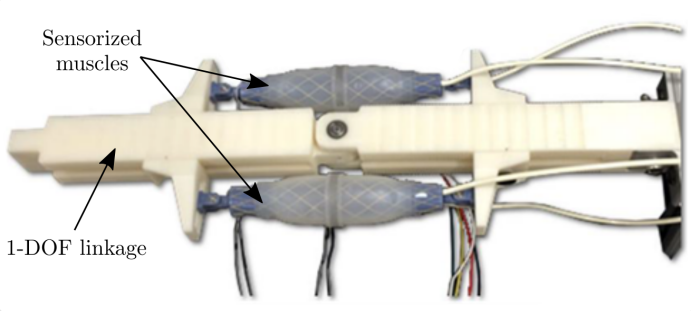

Figure 2.9: One degree-of-freedom experimental test setup actuated by an antagonistic pair of pneumatic muscles with EGaIn liquid metal sensors.

2.2.1 Static force experiment

Static force testing was performed with a single muscle connected to the linkage by measuring the end-effector force as the end-effector was held fixed and the muscle was pressurized. The muscle was configured on the linkage to achieve a range of motion from 0 degrees at maximum muscle length to approximately 25 degrees at full contraction (55.2 kPa, 8 psi). Tests were performed at 0 and 10 degrees, with muscle pressures from 0 to 41.4 kPa (6 psi). At each test pressure, the reaction force at the end-effector was measured via a low-friction pulley system connecting the end-effector to the Instron load cell. The linkage was set up in the horizontal

plane to eliminate gravitational effects. Axial and radial sensor voltages were both recorded throughout each test and used to estimate end-effector force. As shown in Figure 2.10, end-effector force predictions were relatively noisy but generally tracked measured force.

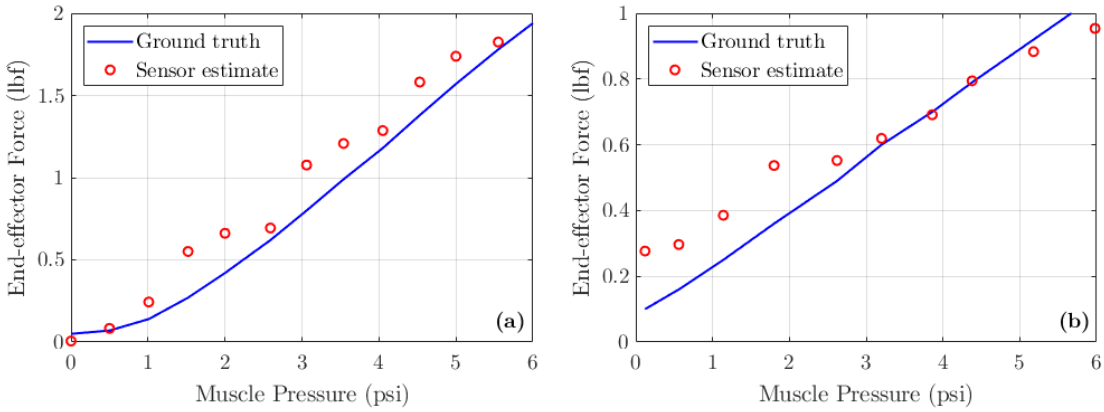

Figure 2.10: Sensor-estimated end-effector force versus ground truth measurement for **(a)** 0 deg linkage angle and **(b)** 10 deg linkage angle.

2.2.2 Joint stiffness experiment

Stiffness testing was performed with two muscles connected to the linkage in an antagonistic configuration (Figure 2.9), such that the linkage angle range was approximately ±12.5 degrees. After pressurizing each muscle to achieve the desired linkage angle, the end-effector was displaced a fixed distance using the Instron pulley setup. End-effector reaction force was measured over the full range of displacement. Testing was performed at 0 degrees with both muscles connected to the same pressure source and at 5 degrees with each muscle connected to its own pressure source. The axial and radial sensor voltages were recorded throughout each test and used to estimate end-effector force. As shown in Figures 2.11 and 2.12, end-effector force estimates generally trended with ground truth measurements, but accuracy significantly suffered with the addition of the second muscle.

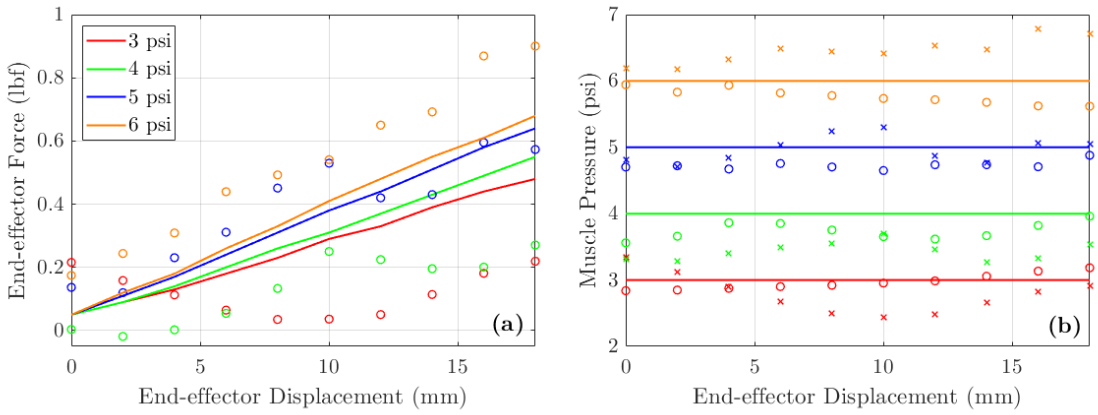

Figure 2.11: (a) Sensor-estimated end-effector force (circle marker) versus ground truth measurement (line) for 0 deg initial linkage angle; estimates are averages between two antagonistic muscles. (b) Sensor-estimated muscle pressures (circle marker for extension muscle, x marker for contraction muscle) versus controlled pressure (line).

2.3 Discussion

Overall, the limiting factor to muscle force estimation accuracy is the sensitivity of muscle pressure estimates to variation in muscle diameter measurements. To show this, the pressure estimates for both muscles during the 0-degree stiffness angle test are plotted in Figure 2.11b: the trends in pressure estimation error directly correspond to fluctuations in linkage end-effector force estimation. Muscle pressure estimation is particularly sensitive to diameter estimation because the magnitude of muscle diameter expansion per unit pressure change is small. Thus, any error in the radial sensor measurement is amplified when correlated to muscle pressure.

Additionally, muscle force estimates are very sensitive to any baseline voltage shift of the EGaIn sensors. If the baseline voltage measured for either the axial or radial sensor prior to use does not accurately represent the sensor baseline throughout subsequent operation, force prediction accuracy will suffer.

Furthermore, robustness issues limit the use of liquid metal sensors outside the lab. The EGaIn liquid metal in each sensor microchannel slowly oxidizes over the life of the sensor, causing the nominal sensor resistance to increase. While this can

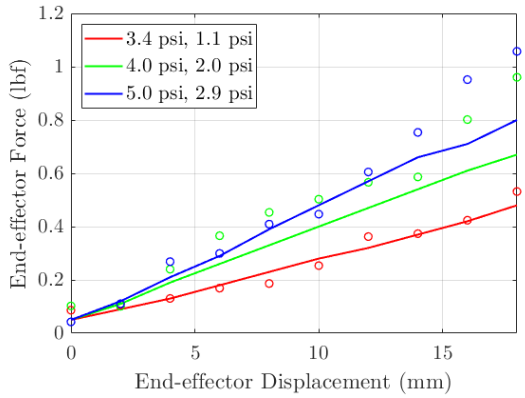

Figure 2.12: Sensor-estimated end-effector force (circle marker) versus ground truth measurement (line) for 5 deg initial linkage angle linkage angles; estimates are averages between two antagonistic muscles.

be compensated by periodic sensor calibration, oxidization can eventually lead to breakage in the microchannel conductive path. Sensors are prone to leaking, as well—over-straining the sensor, applying localized pressure to the sensor microchannel, or even normal repeated use tends to cause EGaIn leakage from the sensor microchannel at the wire lead interfaces over time. Finally, sensor fabrication complexity related to casting consistent microchannels, bonding silicone layers, injecting EGaIn into the microchannels, and attaching wire leads results in low sensor yield.

2.4 Significance

The ability to estimate both the force and displacement of pneumatic artificial muscles exclusively using muscle-integrated sensors eliminates the requirement for external sensors and encoders. This facilitates a more modular approach to the design of muscle-actuated robots, such as for wearable devices, wherein muscles can be configured to meet both the kinematic and dynamic requirements of the device without additional consideration for sensor placement.

However, the liquid metal sensor-embedded pneumatic muscles developed in this work were shown to have several issues that limit their capabilities in practical use.

While robustness issues related to sensor fabrication complexity may potentially be mitigated via alternate fabrication techniques, such as such as replacing cast microchannels with silicone tubing [19] or direct laser patterning of liquid metals [25], muscle force estimation accuracy is limited due to radial pressure sensing resolution. For a single sensorized muscle, accuracy may be acceptable in some applications; but, the cumulative error using an antagonistic pair of muscles is excessive.

CHAPTER 3
OPTICAL REFLECTANCE SENSOR

Recent advancements in soft sensing have focused on optical sensing methodologies, which do not require special conductive materials and are not designed specifically for one type of soft actuator. Stretchable optical waveguides have been used to measure the change in light transmission during bending, stretching, compression, etc. [26], [27]. Other sensing techniques measure the attenuation or reflection of light by diffusive particles embedded in an elastomer under various modes of deformation [28], [29]. Recently, a reflective elastomer foam sensor was developed to quantify twisting and bending [30].

Inspired by these approaches, a novel optical sensor design is developed that measures the light reflected by strategically designed silicone features that can be embedded in a variety of soft actuators [31], [32]. The sensor is straightforward to fabricate, composed of inexpensive off-the-shelf electronics, and is versatile—it can measure multiple deformation modes with the same basic design in various soft actuators or structures. Several advantages of this sensor over the previous liquid metal design include:

- **Robustness**: no oxidization or leaking issues common to conductive liquid sensors.
- **Production yield**: silicone casting and shape deposition-based fabrication achieves high reproducibility; no intricate cast features like microchannels are required
- **Plug-and-play**: sensor electronics can be easily swapped in and out of an actuator with no modification

A pneumatic artificial muscle was designed with two integrated optical sensors to measure the contraction length and force of the muscle. The sensorized muscle can be readily incorporated into a robotic system to provide compliant actuation with kinematic and dynamic feedback—the only additional requirements are a pneumatic pressure source and a microcontroller capable of reading analog signals

In this chapter, the sensor and pneumatic muscle design are first detailed. Next, optical sensor response is characterized for muscles under no load. The process of calibrating sensors to muscle contraction length and force is then described. Muscle sensor performance is subsequently evaluated on a two-degree-of-freedom (2-DOF) arm with two antagonistic sensorized muscle pairs: arm kinematics and dynamics are estimated from optical sensor measurements over several tests. Additionally, the impact of external disturbances on sensor performance is evaluated.

3.1 Methodology

3.1.1 Design and fabrication

Optical sensor. The optical sensor uses an infrared light-emitting diode (LED) (IF E91D; Industrial Fiber Optics, Inc.) and photodiode (IF D91; Industrial Fiber Optics, Inc.) to measure the amount of light reflected by a corresponding silicone diaphragm within a soft actuator: The LED is directed at the surface of the diaphragm and light reflected directly back from the diaphragm passes into the photodiode. The typical peak wavelength of the LED is 870 nm, and the typical peak of the photodiode is 880 nm. A 100-ohm potentiometer (3312J; Bourns, Inc.) is used in series with the LED to adjust its light output, allowing for the sensitivity of each optical sensor to be tuned after it is connected into an actuator. An operational amplifier (TLV2460; Texas Instruments) is used to amplify the photodiode signal for measurement by a microcontroller.

These sensors are utilized in a pneumatic muscle by integrating two sensors into

each of the muscle's two end cap assemblies—one for contraction length sensing and the other for pressure sensing. As shown in Figure 3.1, a LED-photodiode sensor pair are housed in the 3D-printed muscle end cap at each end of the muscle. A small piece of 0.25-mm thick aluminum is positioned between the LED and photodiode to block light emitted at the side of the LED from passing directly into the photodiode. Each sensor's circuit board (containing the potentiometer and operational amplifier) is mounted directly to the end cap (Figure 3.1d). A shielded three-lead cable is soldered to each board for power, ground, and signal connections.

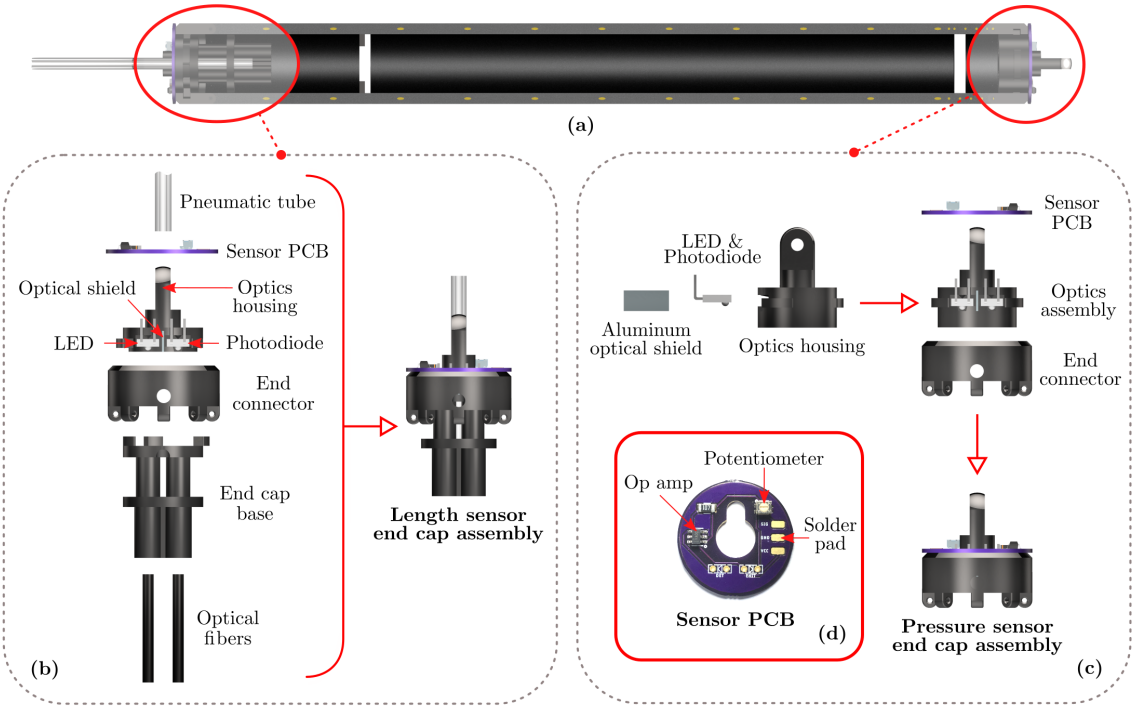

Figure 3.1: Optical length and pressure sensor assemblies for integration with pneumatic artificial muscle: **(a)** cross-section of muscle showing locations of sensor assemblies; **(b)** length sensor end cap assembly; **(c)** pressure sensor end cap assembly; **(d)** sensor circuit board.

On the pressure sensor side of the muscle, the end cap is not sealed in place; instead, the pneumatic seal is achieved by the pressure sensor diaphragm. This allows for easy replacement of pressure sensor electronics by simply removing the end cap. On the length sensor side of the muscle, the end cap is separated into two pieces

(Figure 3.1b): the first piece is sealed in place with silicone and contains optical fibers for transmitting and receiving light; the second piece contains the sensor electronics and is removable. This again facilitates replacement of the length sensor without modification of the muscle.

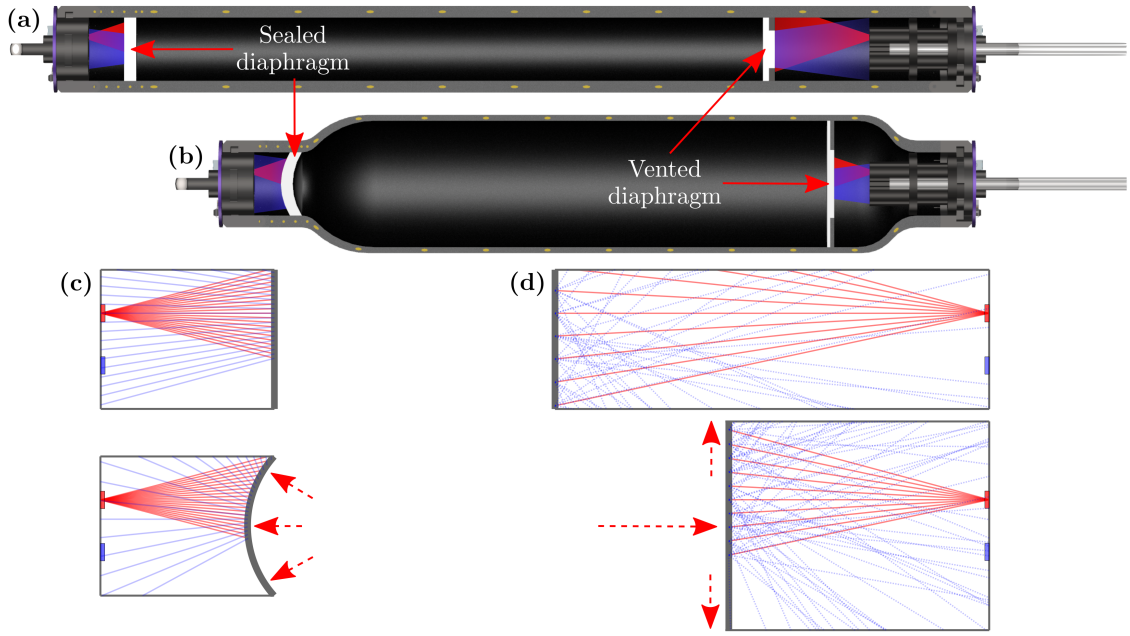

Figure 3.2: Operating principle of optical sensors: red represents IR light emitted by LED and blue represents IR light reflected by diaphragm back to photodiode. **(a)** Unpressurized muscle with sealed diaphragm for pressure measurement and vented diaphragm for length measurement; **(b)** pressurized muscle showing sealed diaphragm deflected under pressure and vented diaphragm stretched/translated toward length sensor end cap. **(c)** Specular reflection by sealed diaphragm before muscle pressurization (top) and after pressurization (bottom); **(d)** diffuse reflection by vented diagram before muscle pressurization (top) and after pressurization (bottom).

Sensor operation. The optical pressure sensor, with its corresponding sealed diaphragm in the pneumatic muscle, utilizes the mechanism of specular reflection: for a light ray reflected by a mirror-like surface, the angle of reflection is the same as the angle of incidence. Initially, the sealed diaphragm surface is flat and reflects a nominal amount of light from the LED to the photodiode based on the distances between the LED, the photodiode, and the diaphragm surface (Figure 3.2a). As muscle pressure

increases, the sealed diaphragm balloons out along the muscle axis toward the end cap (Figure 3.2b), such that the diaphragm surface normal is no longer constant along the diaphragm surface. This spreads the distribution of specularly-reflected light rays over a broader angular range, reducing the amount of light reflected into the photodiode. Geometric ray tracing is used in Figure 3.2c to elucidate this mechanism, showing a decrease in the number of specularly reflected rays received by the photodiode with the diaphragm deflected.

To prevent the sealed diaphragm from stretching radially during inflation, Kevlar fibers are wrapped circumferentially around the diaphragm section of the muscle, as detailed in the muscle fabrication process (Figure 3.3, step 2). To maximize optical reflectivity, white silicone pigment is added to the sealed diaphragm. The thickness of the sealed diaphragm was tuned in preliminary testing to achieve sensor response over the entire pressure operating range of the muscle; a thicker diaphragm deflects less and reduces sensitivity at low pressures, whereas a thinner diaphragm deflects more and stops reflecting any light back to the photodiode at high pressures.

The optical length sensor and corresponding vented diaphragm utilize the mechanism of diffuse reflection——incident light rays are scattered from the reflecting surface at many angles. Light from the LED is reflected by a flat vented diaphragm in many directions, and some of that light is received by the photodiode. As the muscle contracts, the diaphragm translates closer to the LED-photodiode pair and stretches radially, but no deflection along the muscle axis occurs because the diaphragm is vented (Figure 3.2b). With translation of the diaphragm, the aspect ratio of photodiode lens to photodiode–diaphragm distance increases and the photodiode lens spans a larger angular range of reflected light. Geometric ray tracing is again used in Figure 3.2d to visualize this mechanism, showing an increase in the number of diffusely reflected rays received by the photodiode with the diaphragm translated closer to the photodiode. To be clear, both specular and diffuse reflection play a role in the two

types of optical sensors detailed here, but one mechanism in particular is exploited for each sensor.

The optical length sensor diaphragm is composed mainly of white-pigmented silicone to enhance reflectivity, but also includes a 3-mm-wide black-pigmented silicone annulus to improve sensor response characteristics: in preliminary testing, length sensor response increased monotonically throughout contraction with the black annulus; however, an initial dip in length sensor response during contraction was observed without the annulus. A hypothesis for this behavior is that the deformation of the silicone diaphragm at the inner muscle wall interface results in an initial decrease in the amount of light reflected back to the photodiode before the translation of the diaphragm toward the photodiode has the net effect of increasing the amount of light reflected back.

Pneumatic muscle. The pneumatic artificial muscle designed in this study is primarily composed of platinum-cure silicone rubber (Smooth-On, Inc.) embedded with helically-wrapped Kevlar threads that constrain muscle deformation under pressure. The nominal length and outer diameter of the unpressurized muscle are 22 and 2.2 cm, respectively. As previously described, two silicone diaphragms are integrated into the muscle for sensing. A 3-mm thick vented silicone diaphragm, with two holes allowing the passage of air through the diaphragm, is located 5 cm away from one end of the muscle. A 3-mm thick sealed silicone diaphragm (no holes) is positioned 1.7 cm away from the other end of the muscle and provides the pneumatic seal for that end of the muscle. White and black silicone pigments (Silc Pig; Smooth-On, Inc.) are used in the internal diaphragms and the muscle bladder to enhance optical sensor performance, as detailed above. Additionally, the main bladder of the pneumatic muscle uses black pigmented silicone to minimize the optical reflectivity of the inner muscle wall and to block ambient infrared light from affecting optical sensor baseline

signals. Pigment is mixed into uncured silicone at 3% by weight of the silicone, per the upper limit specified by Smooth-On.

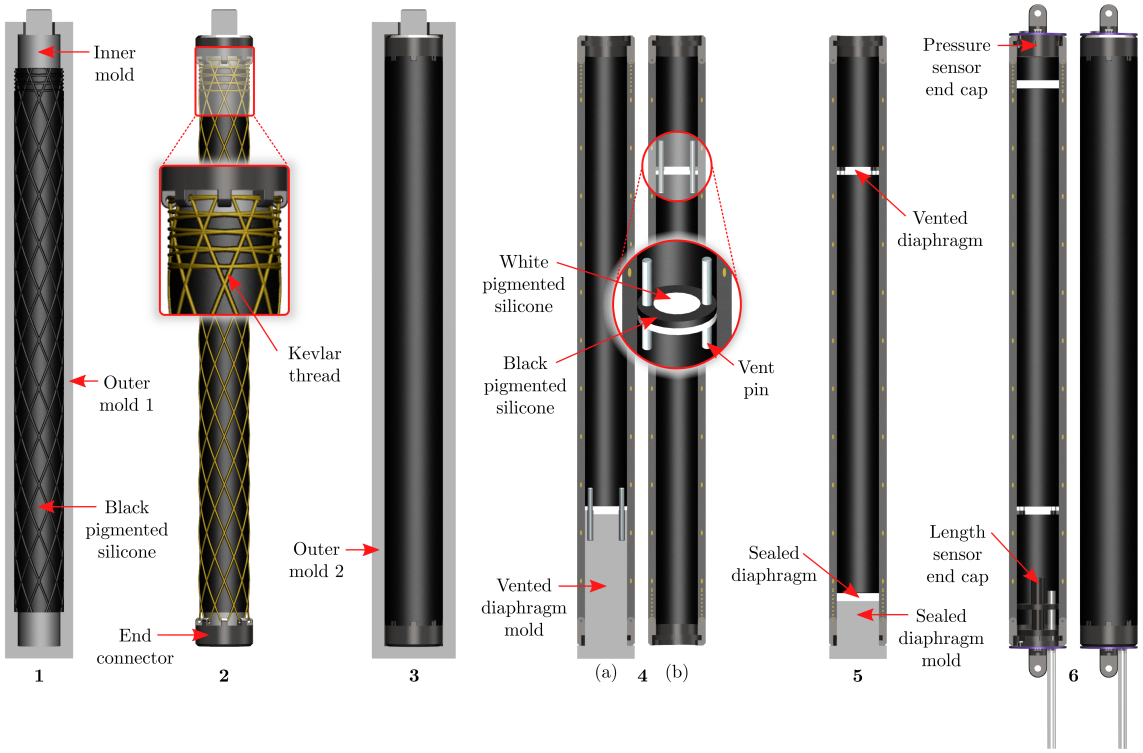

Figure 3.3: Fabrication steps for sensorized pneumatic artificial muscle: **(1)** cast half-thickness muscle bladder with helical grooves for thread placement; **(2)** add end-connectors and wrap Kevlar threads; **(3)** cast second layer around bladder, encapsulating Kevlar threads at mid-bladder; **(4)** cast two-color vented diaphragm; **(5)** cast one-color sealed diaphragm; **(6)** add end caps and seal length sensor end cap in place.

Each muscle is fabricated over a six-step process illustrated in Figure 3.3 and described as follows:

1. Cast the first layer of the muscle bladder up to half-thickness using Dragon Skin 10 NV mixed with black pigment. The outer molds contain extruded helical features that create helical grooves in the half-thickness silicone layer.

2. Attach the thread end-connectors to the inner mold using alignment pins and wrap the half-thickness muscle bladder with Kevlar threads along the guide grooves embedded in the silicone bladder. The muscle is wrapped eight times in each direction (clockwise and counterclockwise) with one continuous Kevlar

thread—each end-connector contains eight eyelets through which the thread is routed.

3. Cast the second layer of the muscle bladder (up to the full muscle thickness) using Dragon Skin 10 NV mixed with black pigment; this encapsulates the Kevlar thread midway through the muscle bladder. After the silicone has cured, remove the inner mold from the muscle bladder.

4. Cast the vented diaphragm with black annulus:

   (a) Insert the vented diaphragm mold with vent pins and cast 0.37 mL of Dragon Skin 10 NV mixed with white pigment by injecting silicone through the muscle bladder onto the mold via a hypodermic needle and syringe. Remove the mold but leave the vent pins in place.

   (b) Flip the muscle and cast 0.23 mL of Dragon Skin 10NV mixed with black pigment, via hypodermic needle, into the annular void left by the vented diaphragm mold. Remove the vent pins.

5. Flip the muscle, insert the sealed diaphragm mold, and cast 0.6 mL of Dragon Skin 30 mixed with white pigment via hypodermic needle. Remove the sealed diaphragm mold.

6. Attach the optical pressure sensor end cap assembly to the sealed diaphragm side of muscle. Attach the optical length sensor end cap assembly to the vented diaphragm side of the muscle and seal in place by injecting Dragon Skin 10 NV silicone into the hole in the end-connector.

3.1.2 Control and data acquisition

For sensorized muscle characterization and subsequent experiments, pneumatic pressure control was performed by pulse-width modulation of up to four solenoid valves

(VQ100 Series; SMC Corp.), one per muscle. A proportional-integral (PI) plus feed-forward controller for each muscle was run on an MSP432 microcontroller (Texas Instruments) at 100 Hz to regulate muscle pressure. Integral anti-windup was added to prevent the integral term from exceeding ±50% duty cycle. In addition, valve dead zone compensation was implemented to maintain the duty cycle at or above 10%—at duty cycles less than 10%, there is insufficient time for the valve to open, so no airflow occurs.

Pressurized air was supplied by two diaphragm pumps (BTC-IIS; Parker Hannifin) connected to a 1-L pressure accumulator chamber. To connect all pneumatic components, 1/8-inch inner diameter tubing was used. On-off control of the diaphragm pumps maintained the accumulator chamber pressure between 12 and 14 psi, providing a relatively constant pressure source for the pneumatic control system.

The MSP432 microcontroller sampled analog pressure transducer and optical sensor data at 100 Hz with 14-bit ADC resolution. To mitigate the effects of pressure oscillations resulting from opening and closing of the solenoid valves, pressure data was low-pass filtered through a 20th-order finite-impulse response filter with a cutoff frequency of 10 Hz. The microcontroller communicated via UART with a computer running a Python script to record sensor data and update PI controller pressure setpoints at 30 Hz. The system schematic is shown in Figure 3.4.

3.1.3 Sensorized muscle characterization

To verify sensorized muscle functionality, optical sensor response and muscle contraction range were characterized by performing repeated actuation cycles under no load. Over each cycle, the muscle was slowly pressurized from 0 to 55 kPa and then vented back down to 0 kPa at the same rate over 32 seconds. The length of the muscle was measured using an electromagnetic (EM) tracker system (3DGuidance trakSTAR; ATC) with 1.4 mm root mean square (RMS) position accuracy. The muscle was

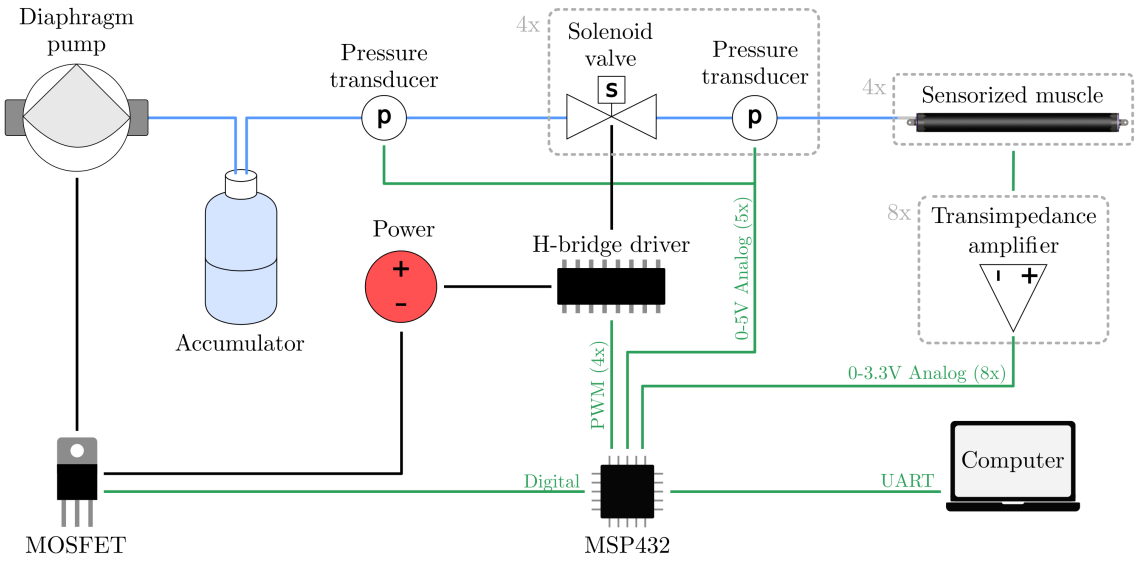

Figure 3.4: Pressure control and data acquisition schematic: blue lines represent fluidic connections, green lines represent signal connections, and black lines represent power connections.

suspended from one end with its axis oriented vertically and the EM tracker sensor was fixed to the free end of the muscle, as shown in Figure 3.5a. Muscle pressure was measured using an analog pressure transducer (Honeywell ASDXAVX030PGAA5). Throughout the test, the voltages of the optical length and optical pressure sensors were recorded, along with ground-truth muscle length and pressure measurements.

Several preliminary inflation–deflation cycles were run for each muscle and the LED brightness of each sensor was adjusted (via its corresponding potentiometer) to maximize the voltage range of each sensor over the full pressure/length range of the muscle without saturating at the limits. Each muscle was then characterized over 10 inflation–deflation cycles. As shown in Figure 3.5b, optical pressure sensor measurements were consistent across cycles 2–10. However, for the first cycle of each muscle, a slightly higher sensor response curve during inflation was observed. This phenomenon was consistent across separate trials and different muscles and may be the result of the stiff, viscoelastic Dragon Skin 30 diaphragm settling to a slightly different resting configuration over an extended period after actuation. In addition, a hysteresis loop

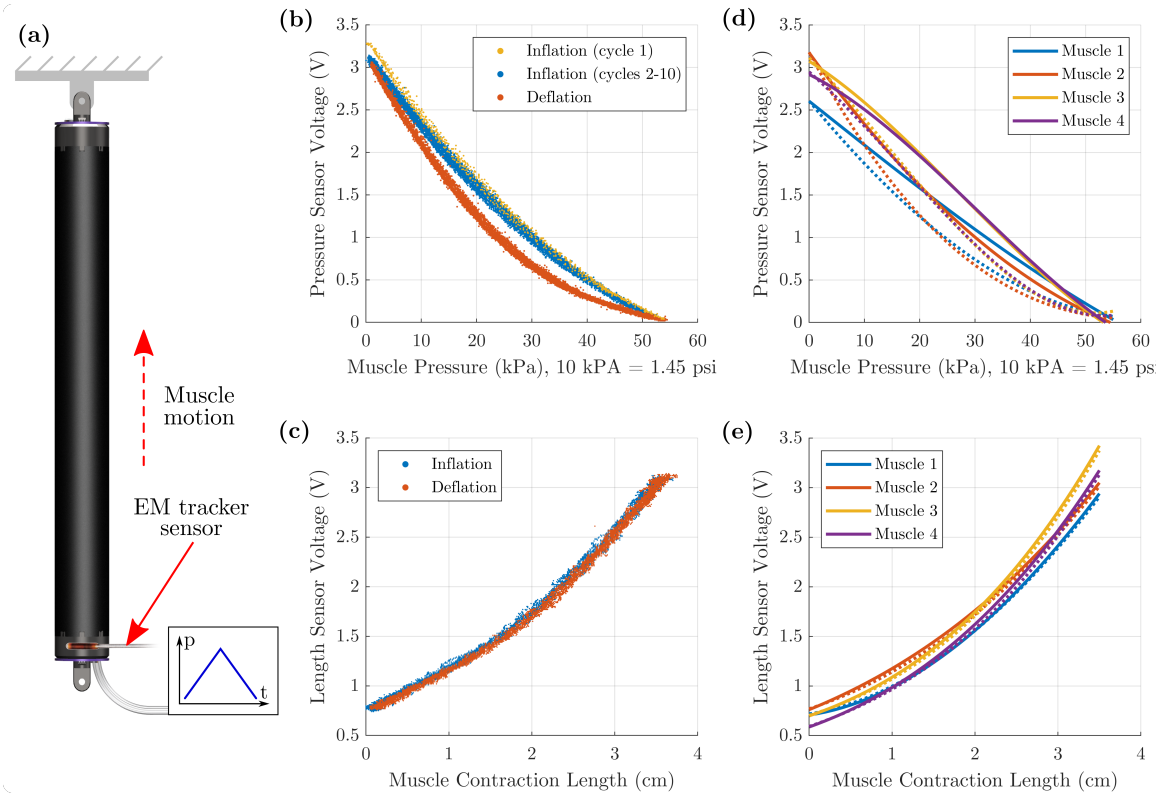

Figure 3.5: Optical sensor characterization for 10 muscle actuation cycles: **(a)** test setup with muscle fixed at one end; **(b)** muscle pressure versus optical pressure sensor voltage for single muscle; **(c)** muscle contraction length versus optical length sensor voltage for single muscle; **(d, e)** comparison of optical sensor data for four muscles with 10-cycle data for each muscle fit to a third-order polynomial—solid lines represent inflation, whereas dashed lines represent deflation.

was exhibited by the optical pressure sensor for each pressurization–depressurization cycle; this behavior is also attributable to the viscoelastic properties of the pressure sensor diaphragm.

Optical length sensor measurements were consistent across all cycles, with no divergent behavior observed for the initial cycle of each test (Figure 3.5c). In addition, there appeared to be minimal hysteresis for the optical length sensor. This is to be expected, as the length sensor response mechanism is relative diaphragm position change, not diaphragm deformation. The sensor response curves for both pressure and length sensors were similar across all four muscles, as shown in Figure 3.5d and 3.5e, though length sensor response was more consistent from muscle to muscle

compared with pressure sensor response.

Muscle contraction was repeatable over 10 cycles, with an average standard deviation of 0.5 mm contraction for 1 kPa data bins. Maximum muscle contraction at 55 kPa was approximately 3.8 cm. Over the 32-second pressurization–depressurization cycle, the hysteresis loop width was approximately 4 mm. Over a faster cycle, hysteretic effects would be expected to increase.

3.1.4 Sensorized muscle calibration

The optical sensor calibration data necessary to estimate pneumatic muscle contraction length and force was collected over a set of blocked force tests for each of four muscles. Each muscle was connected to an Instron mechanical test frame (5965 Universal Testing System) and preloaded to 1 N to remove any slack in the test setup. In each test, muscle pressure was maintained at a fixed setpoint while the Instron crosshead moved in the direction of contraction at 80 mm/min, as shown in Figure 3.6a. The contraction force applied by the muscle to the crosshead was measured at 10 Hz. Blocked force tests were run with fixed pressures between 5 and 55 kPa in 5 kPa increments.

Pneumatic muscle force versus contraction length was consistent across all four muscles tested, as shown in Figure 3.6b. The maximum difference in contraction force between any two muscles was 7.7 N, occurring for near-zero contraction length (near-maximum force) at the maximum test pressure of 55 kPa. The maximum contraction force across all four muscles was 120 N at full muscle length and 55 kPa.

While the optical pressure sensor responded mainly to muscle pressure change and the optical length sensor responded mainly to muscle length change, blocked force data also showed a small degree of coupling between both sensors (the optical length sensor is slightly sensitive to actuator pressure and the optical pressure sensor is slightly sensitive to actuator length). Therefore, to account for the small coupling

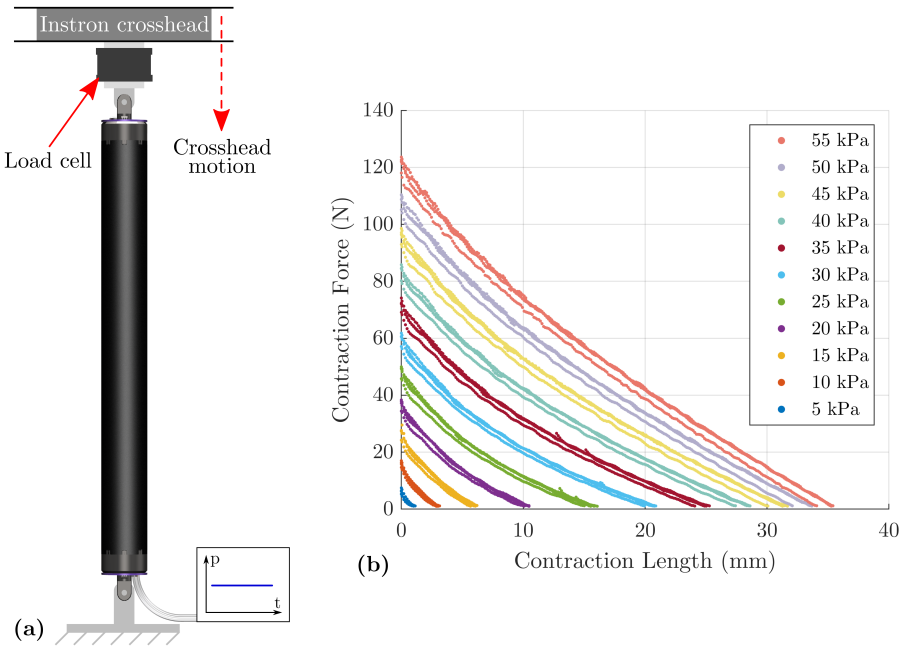

Figure 3.6: Blocked force testing: **(a)** test setup with muscle fixed at one end and connected to the Instron crosshead at the other; **(b)** muscle contraction force versus contraction length at fixed pressures between 5 and 55 kPa for four muscles.

effects and maximize estimation accuracy, both optical sensor measurements were utilized for muscle length estimation and likewise for muscle force estimation.

To estimate length, a 2D polynomial surface of degree three in both dimensions was fit to muscle contraction length versus optical length and pressure sensor voltage, as shown in Figure 3.7. Similarly, a surface was fit to muscle contraction force versus optical sensor voltages, as shown in Figure 3.8. Surface fit metrics are shown in Table 3.1: the poorest coefficients of determination for the length and force surface fits of any muscle were 0.997 and 0.989, respectively; the largest root mean square errors were 0.49 mm and 2.95 N, respectively.

3.2 Experiments and Results

Evaluation platform. To evaluate sensorized muscle length and force estimation capabilities, four calibrated muscles were configured on a planar 2-DOF arm, with one antagonistic muscle pair per joint, as shown in Figure 3.9. The arm was constructed

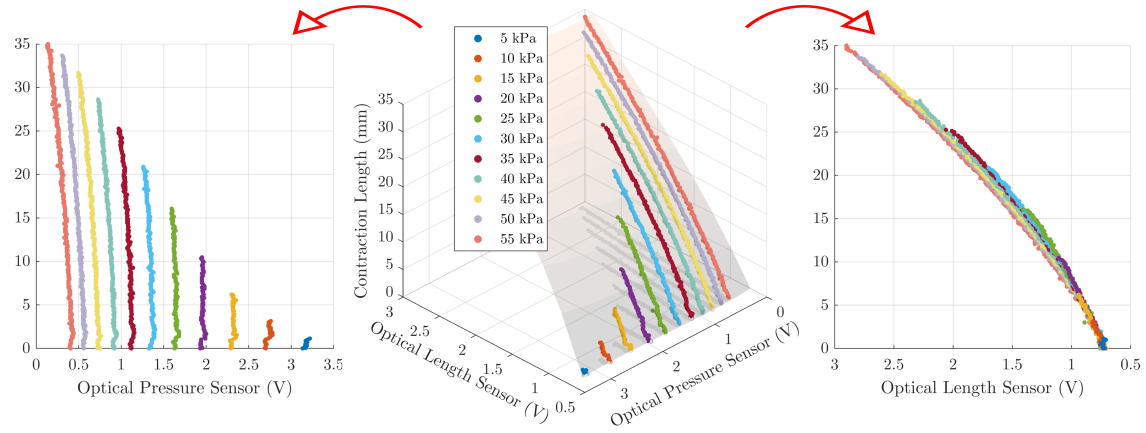

Figure 3.7: Optical sensor length calibration: muscle contraction length versus optical sensor voltages with polynomial surface fit for muscle length estimation.

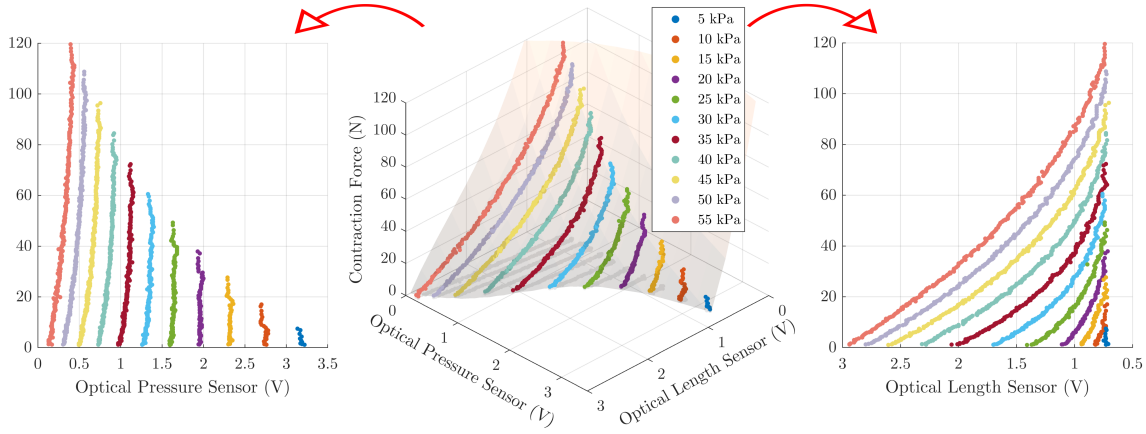

Figure 3.8: Optical sensor force calibration: muscle contraction force versus optical sensor voltages with polynomial surface fit for muscle force estimation.

Table 3.1: Surface fit metrics for muscle length and force versus optical sensor data.

Muscle	Length		Force	
	R^2	RMSE (mm)	R^2	RMSE (N)
1	0.997	0.49	0.990	2.8
2	0.999	0.27	0.996	1.8
3	0.998	0.35	0.992	2.4
4	0.997	0.47	0.989	2.9

of extruded ABS links connected by 3D-printed hinge joints with low-friction ball bearings. Each joint included an encoder for ground-truth angle measurement with a resolution of 0.043 deg. Each pair of muscles was connected at one end to a 4-

cm diameter pulley at the respective join. The other end of the muscle pair was connected to the proximal link of the joint through a ratcheting tensioner that was used to finely adjust muscle tension and nominal joint angle. The arm was positioned in the horizontal plane to eliminate gravitational loading about the joints.

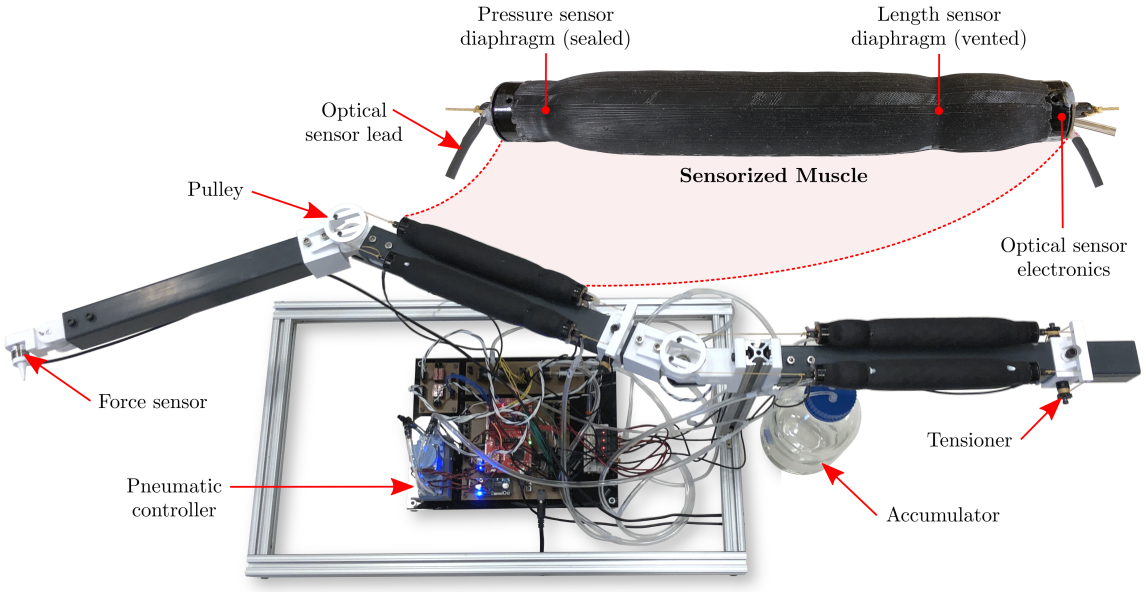

Figure 3.9: Two degree-of-freedom arm evaluation platform with two antagonistic pairs of sensorized pneumatic artificial muscles.

Arm configuration. Four sensorized muscles were connected on the 2-DOF arm, two at each joint. Based on joint pulley radius and maximum muscle contraction, the angle range for each joint was ±45 deg. The muscles were configured to achieve nominal joint angles—the angles corresponding to equal pressures in antagonistic muscle pairs—of -22.5 deg at joint 1 and 45 deg at joint 2; the corresponding nominal arm position is shown in Figure 3.10. This configuration was chosen to provide a more two-dimensional workspace (larger range along x-direction) with a larger area than the arc-shaped workspace corresponding to 0-deg nominal joint angles.

The four muscles were each pre-tensioned on the arm to 7.5 N to prevent any of the muscles from becoming slack during testing. This was an important consideration for accurate estimation of arm position from optical sensors, as the contraction length of

a muscle no longer directly corresponds to joint angle once the muscle becomes slack. Pre-tensioning was performed by inflating all four muscles simultaneously to pressures corresponding to 50% maximum contraction (about 1.75 cm) at 7.5 N loading; the pressure for each muscle was calculated from a third-order polynomial regression of blocked force—contraction length data. The two muscles at each joint were then tensioned simultaneously until both muscles were 50% contracted and the desired nominal joint angle was concurrently achieved.

Arm initialization. Before each test within an experiment, a brief initialization procedure was performed. First, each muscle was inflated up to full pressure and vented back to zero gauge pressure. This was done to account for the inconsistent behavior observed in muscle sensor characterization, in which the first of 10 inflation–deflation cycles showed a slightly higher pressure sensor signal than the subsequent 9 cycles. Next, the muscles were pressurized according to the nominal arm configuration—corresponding to 50% contraction with 7.5 N tension—and 5 seconds were provided for arm motion to settle. Muscle contraction length estimates from optical sensors were recorded over the subsequent 5 seconds and the initial contraction length of each muscle was then set as the average estimated contraction over the 5-second window. In addition, the initial ground-truth arm angles were set to the corresponding average encoder angles over the same time window.

Experimental progression. Over the first two experiments, the arm's end-effector position was estimated from optical muscle sensors for both static end-effector points and elliptical trajectories in the workspace. Over the next two experiments, end-effector forces and joint to torques were estimated from optical sensors for static points and semi-random trajectories in the workspace. Finally, the effect of external disturbances on sensing performance was evaluated.

3.2.1 Kinematics estimation experiments.

Joint angle estimation. To compute 2-DOF arm joint angles from muscle length and pressure sensor measurements, the contraction length of each muscle was first estimated through its associated sensor voltage–contraction length surface fit (Figure 3.7). Change in joint angle was then computed from pulley radius (2 cm) and change in muscle length (versus initial length). Finally, each joint angle was calculated as the average of the two angle estimates from both muscles at the joint.

Static position experiment. End-effector static position was estimated from optical sensor measurements at multiple points distributed throughout the arm's workspace and compared to ground-truth position calculated from joint encoder angles. Four target muscle pressures were generated (one per muscle) for each end-effector position using muscle blocked force calibration data. Consistent with the initial arm configuration procedure, pressures were generated to maintain 7.5 N of tension in each muscle throughout testing. For each end-effector pressure configuration, a 5-second settling time was provided to ensure the arm was static.

Ten trials were run with 16 end-effector positions per trial for a total of 160 individual test positions. The maximum error from optical sensor position estimates over all 10 trials was 3.4 cm, while the average error was 1.3 cm. Position estimates and true positions are shown for these 10 trials in Figure 3.10. A small amount of variation in the true (and estimated) end-effector position for the same point over multiple trials is observed because of the open-loop nature of the testing——muscle pressure control was closed-loop but there was no end-effector position feedback control. In addition, small oscillations from the pressure control system resulted in corresponding joint and end-effector oscillations.

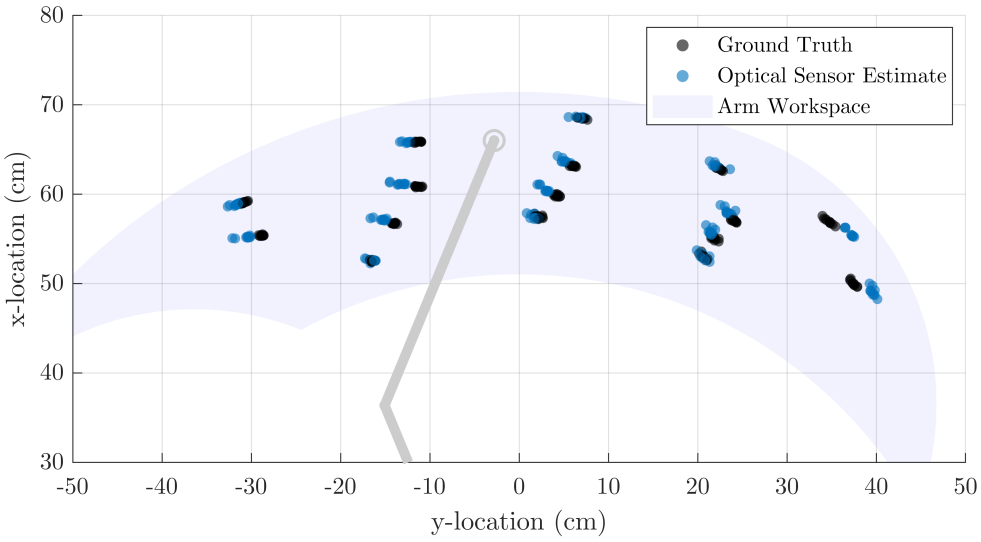

Figure 3.10: Optical sensor-estimated and true positions of two-DOF arm end-effector for 16 points in workspace over 10 trials; nominal arm configuration is shown in gray.

Trajectory experiment. End-effector trajectories were estimated from optical sensor measurements to characterize sensing accuracy for dynamic arm movements. Elliptical trajectories were generated for constant end-effector speeds of 4, 8, and 16 cm/s. Similar to static position tests, end-effector trajectories were run open-loop by generating corresponding pressure trajectories from 7.5 N length-pressure curves and modulating muscle pressures only.

Ten tests were run for each of the three trajectory speeds; results are shown in Figure 3.11. Of all 30 trials, the maximum end-effector estimation error—calculated as the Euclidean distance between the end-effector position estimate and the true position—was 7 cm. The largest average error over 10 trials was 1.2 cm and the largest standard deviation over 10 trials was 0.6 cm, as reported in Table 3.2. The relatively low standard deviation suggests that the number of estimation errors close to the 7 cm maximum was very small. Upon closer examination of raw optical sensor data, infrequent spikes in sensor signals were found. These are likely the result of electrical noise in the pressure control/data acquisition setup. The largest estimation error occurred for the 4 cm/s trajectory test: for this test, only 17 of 9640 data point

errors (<0.2%) were greater than 3 cm, and only 4 (<0.1%) were greater than 4 cm.

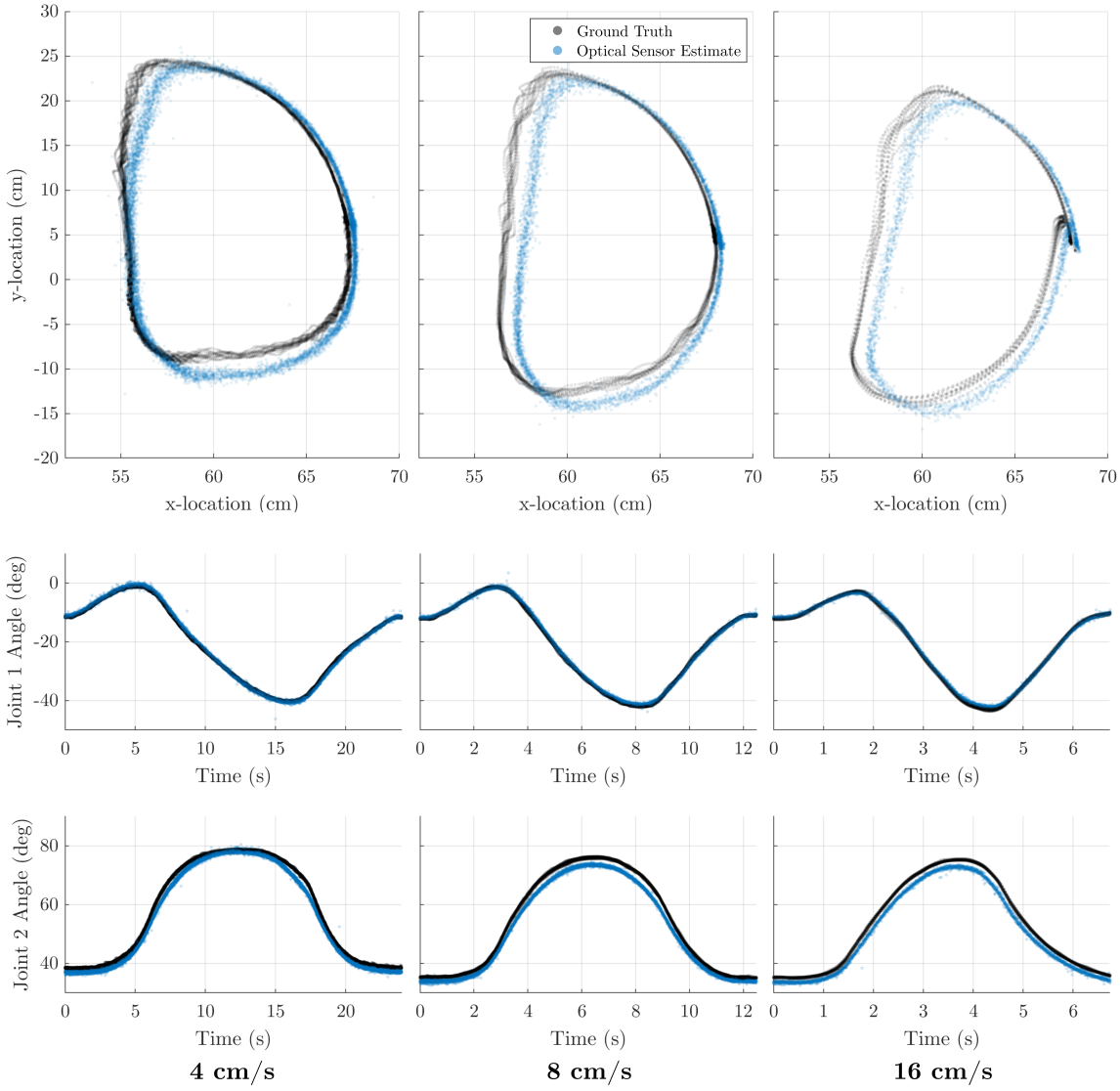

Figure 3.11: Optical sensor-estimated versus true end-effector location and joint angles for open-loop elliptical trajectory at three different end-effector speeds.

3.2.2 Dynamics estimation experiments.

Static force experiment 1. Static end-effector forces were estimated from optical sensor measurements at four locations near the top, left, right, and bottom of the arm workspace. At each location, the end-effector was placed in contact with a fixed obstacle. Muscle pressures were then commanded to displace the end effector 20 cm

Table 3.2: Optical sensor end-effector position estimation error statistics for elliptical trajectories at three speeds with 10 trials at each speed.

Speed (cm/s)	Max Error (cm)	Avg. Error (cm)	Std. Dev. (cm)
4	7.0	1.0	0.6
8	5.4	1.2	0.5
16	6.5	1.2	0.5

along a linear trajectory approximately perpendicular to the fixed obstacle; the commanded displacement lasted 10 seconds and was then reversed over the subsequent 10 seconds. For ground-truth measurement of end-effector forces, a Nano17 force/torque sensor (ATI Industrial Automation) was mounted to the end of the arm; a conical end effector was attached to the Nano17 to ensure point contact with the obstacle.

Joint torques were estimated from muscle sensor signals by estimating the tensile force of each muscle from its respective sensor voltage–contraction force surface fit, and then calculating the resultant torque based on the pulley radius at each joint as

$$\tau_i = (f_{l,i} - f_{r,i})\, r_i \tag{3.1}$$

where τ_i is the ith joint torque, $f_{l,i}$ and $f_{r,i}$ are the left and right muscle forces of the ith joint, and r_i is the pulley radius. At the beginning of each test, before end-effector contact with the obstacle, muscle force estimates were baselined to 7.5 N, corresponding to the nominal muscle pretension during setup of the arm. End-effector forces were then estimated using the inverse Jacobian of the arm at the test configuration

$$\begin{bmatrix} f_x \\ f_y \end{bmatrix} = (J^T)^{-1} \begin{bmatrix} \tau_1 \\ \tau_2 \end{bmatrix} \tag{3.2}$$

where f_x and f_y are the end-effector forces in the x- and y-directions and J is the

arm geometric Jacobian. All calculations were carried out in the arm base coordinate frame, with the x-axis along the outstretched arm at zero-degree joint angles.

Overall, measured and sensor-estimated force data showed significantly more variance than measured and sensor-estimated joint angle data. Therefore, end-effector force and joint torque test data were post-processed using a moving average filter with a window of ±100 data points, corresponding to approximately ±0.3 s. The maximum and average joint torque and end-effector force estimation errors across all four workspace locations are reported in Table 3.3. Maximum errors were computed from moving-average filtered data to exclude outliers caused by optical sensor noise. Estimated joint torques generally tracked the true torques, but consistently under-predicted peak torques for all four end-effector workspace locations. Consequently, estimated end-effector forces also fell below the true forces at higher force magnitudes. This is shown in Figure 3.12 for static force estimation at the left workspace location.

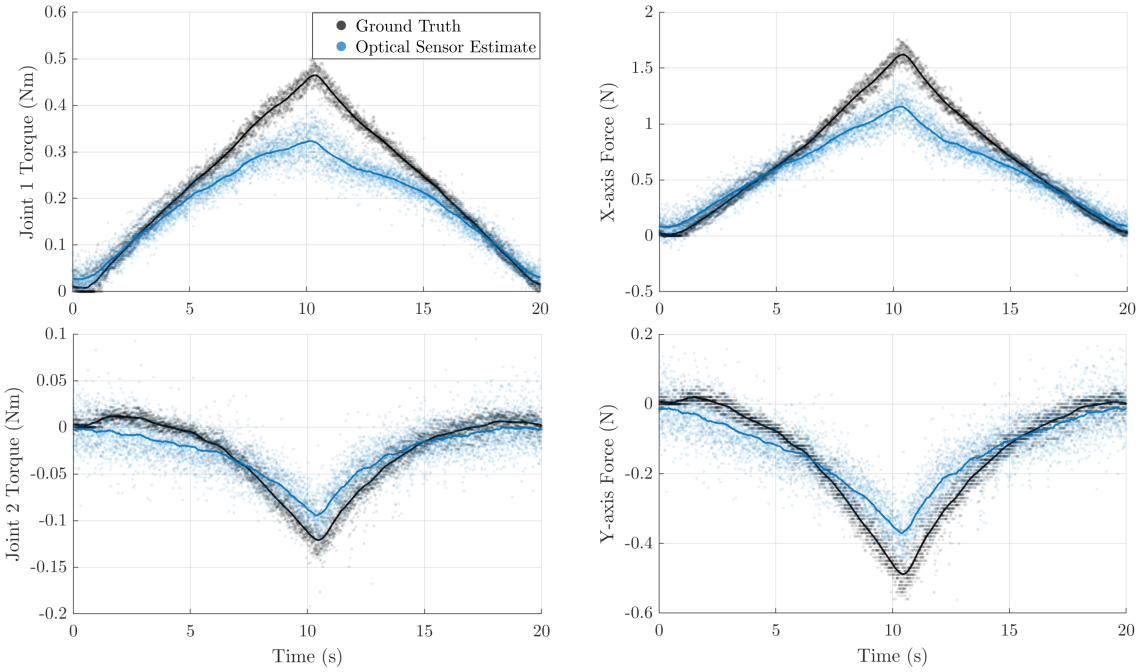

Figure 3.12: Static force experiment 1 results for 10 trials at left end-effector location: estimated versus true joint torques and end-effector forces for 20 cm commanded displacement input.

During testing, it was observed that the antagonist muscle at each joint became slack during the latter part of the commanded displacement, owing to the control scheme used: for a commanded end-effector displacement, the controller decreased antagonist muscle pressure in proportion to increased agonist muscle pressure (based on muscle pressure versus contraction length data). However, because the end effector was fixed during static testing, the decrease in antagonist pressure without joint rotation allowed the antagonist muscle to become slack during the 10-s commanded displacement.

It was also observed that when the antagonist muscles were slack (no applied contraction force), optical sensor force estimates were still greater than zero, thus resulting in underestimated joint torques. This force estimation error for slack muscles is likely due to two factors. First, there is less muscle force versus optical sensor calibration data for the low pressure, small contraction operating region corresponding to a slack muscle, and existing data are noisy, resulting in poorer surface fit quality for this region; in Figure 3.8, this corresponds to the high pressure sensor voltage, low length sensor voltage region of the pressure-length-force plot. Second, contraction force estimation is most sensitive for smaller muscle contractions—this is highlighted by the steep slope of the force versus length sensor curves at lower sensor voltages (smaller contractions) shown in the right plot of Figure 3.8.

Consequently, it was hypothesized that the reduced force estimation accuracy of the slackened antagonistic muscles was responsible for the underestimated joint torques during static testing. Therefore, the static force experiment was repeated with a second control scheme to avoid muscle slackness.

Static force experiment 2. For the second static force experiment, agonist muscle pressures were again ramped over 10 seconds, but antagonist muscle pressures remained fixed. Maximum agonist muscle pressures were increased for each end-effector

workspace location to achieve end-effector forces similar in magnitude to those observed during the first static force experiment. The joint torque and end-effector force estimation errors for the second static force experiment are again summarized in Table 3.3. Joint 1 torque and x-axis force estimates from optical sensor data were more accurate with fixed antagonist pressure versus commanded displacement. Joint 2 torque and y-axis force estimates were similar for both control schemes. Overall, the updated control scheme resulted in more accurate estimates of peak torques and forces, as shown in Figure 3.13 for the fixed antagonist pressure static force test at the left workspace location.

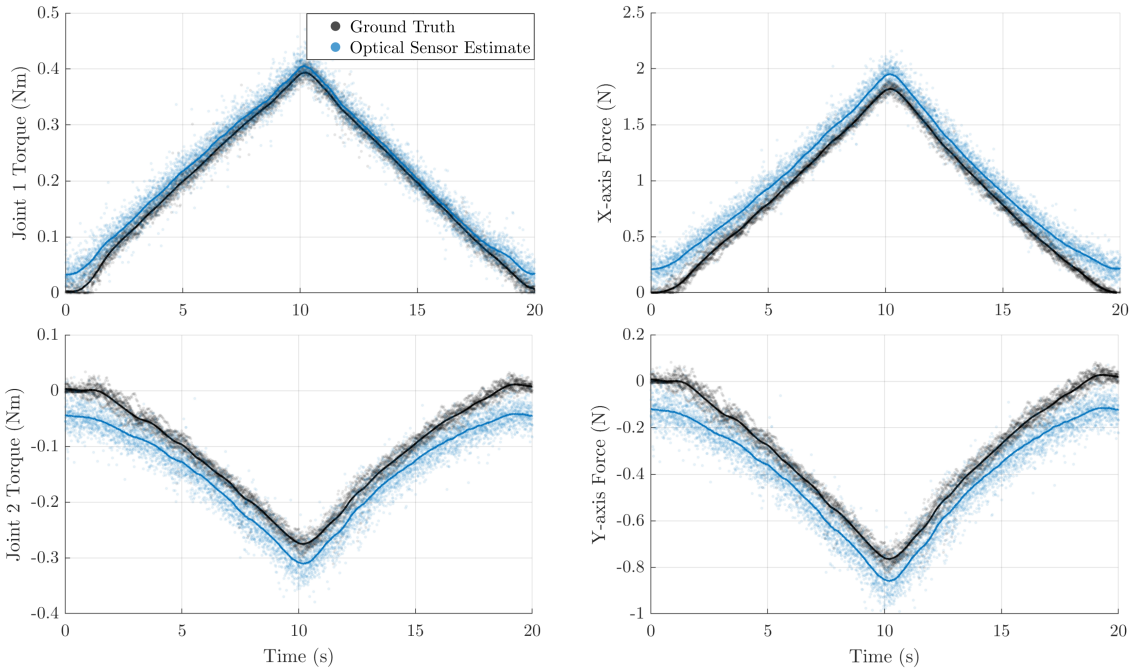

Figure 3.13: Static force experiment 2 results for 10 trials at left end-effector location: estimated versus true joint torques and end-effector forces for agonist muscle pressure ramp input (fixed antagonist pressure).

Dynamic force experiment. Dynamic force testing was performed by estimating end-effector forces while manually moving the end-effector around in the workspace. The muscles were initially pressurized to attain the same nominal arm position as before (joint angles 1 and 2 at -22.5 deg and 45 deg, respectively). The conical

Table 3.3: Static force experimental results: optical sensor joint torque and end-effector force estimation error statistics for experiment 1 (commanded displacement) and experiment 2 (fixed antagonist pressure).

Measurement	Experiment 1		Experiment 2	
	Max Error	Avg. Error	Max Error	Avg. Error
Joint 1 Torque (Nm)	0.15	0.04	0.04	0.02
Joint 2 Torque (Nm)	0.07	0.03	0.06	0.03
X-Axis Force (N)	0.67	0.24	0.33	0.15
Y-Axis Force (N)	0.13	0.06	0.14	0.06

end-effector attached to the force/torque sensor was then moved by hand through approximately elliptical paths at different speeds over 40 seconds. For the dynamic test shown in Figure 3.14, joint 1 moved through a range of about 35 deg, while joint 2 moved through about 40 deg; joint 1 reached a maximum angular velocity of 20 deg/s, while joint 2 reached a maximum velocity of 27 deg/s. Because of the relatively low joint speeds and the low inertia of the lightweight 2-DOF arm, inertial effects were negligible and static force calculations were considered a valid approximation.

Joint torque and end-effector force data were post-processed using a moving average filter with a 20-data-point window (0.6 seconds). Estimated joint torques generally tracked actual torques; however, as shown in Figure 3.14, joint 1 torque estimates generally overpredicted, whereas joint 2 torque estimates underpredicted for negative torques. This resulted in good overall agreement between actual and estimated end-effector forces but led to overprediction in x-axis forces and underprediction in negative y-axis forces. The average x- and y-axis force errors for filtered data were 4.9% and 3.9% of the maximum x- and y-axis forces, respectively.

3.2.3 Sensor disturbance experiment

Sensor disturbance testing was performed to determine the effects of external muscle contacts on contraction length and force estimates from sensor measurements. In

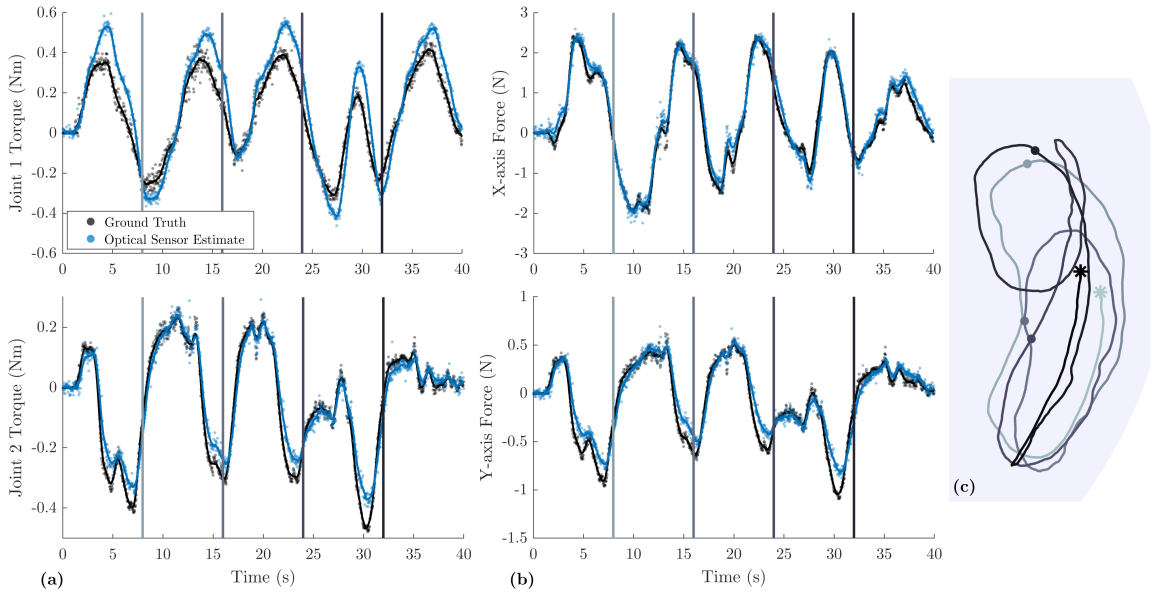

Figure 3.14: Dynamic force experimental results for 2-DOF arm: **(a)** estimated versus true joint torques and **(b)** estimated versus true end-effector forces, where solid lines represent filtered data; **(c)** corresponding end-effector trajectory in shaded workspace moving from light to dark.

each test, the muscle was inflated and maintained at one of several target pressures. The muscle was contacted by a 3-cm diameter hemispheric tool up to a maximum force of either 2 or 4 N, as measured by a Nano17 force/torque sensor connected to the tool. Contact was ramped up to maximum force over approximately 3 seconds. The muscle was supported from the non-contact side by a flat surface; this represents the worst-case scenario, as muscle deformation is more localized than without the supporting surface.

Results for contraction length estimation disturbances are summarized in Table 3.4 and results for contraction force estimation disturbances are summarized in Table 3.5. Minimal impact on length and force estimation accuracy was observed for contact at the middle of the muscle (away from optical sensor diaphragms). The largest effects were observed for contact at the length diaphragm. Contact with the muscle at the length diaphragm deflects the diaphragm axially (similar to the intended mode of deformation of the pressure diaphragm). This significantly reduces the amount of

reflected light, causing a negative change in contraction length estimate. Length and force estimates were less affected for pressure diaphragm disturbances—this is likely because of the increased stiffness in this region of the muscle that results from the circumferential Kevlar thread wrap used to prevent radial deformation of the muscle (Figure 3.3 step 2). Overall, the optical sensors are most sensitive at lower muscle pressures; at higher pressures, the muscle becomes stiffer and less deformation of sensing diaphragms by external contact forces is possible.

Table 3.4: Effects of 2- and 4-Newton external disturbances on sensorized muscle length estimation: deviation from nominal contraction length estimate (mm) at three locations along muscle.

Muscle Pressure (kPa)	Mid-muscle		Length Diaphragm		Pressure Diaphragm	
	2 N	4 N	2 N	4 N	2 N	4 N
14	-0.82	-1.38	-3.60	-11.26	0.37	0.90
28	0.31	-1.07	-0.92	-4.19	0.41	0.38
55	0.39	0.18	-0.16	-0.86	0.16	0.31

Table 3.5: Effects of 2- and 4-Newton external disturbances on sensorized force length estimation: deviation from nominal contraction force estimate (N) at three locations along muscle.

Muscle Pressure (kPa)	Mid-muscle		Length Diaphragm		Pressure Diaphragm	
	2 N	4 N	2 N	4 N	2 N	4 N
14	2.48	4.36	11.31	36.24	0.92	3.96
28	-0.78	3.69	3.20	14.20	1.31	5.32
55	-1.24	-0.56	0.52	2.69	-0.54	-0.99

3.3 Discussion

3.3.1 Simplifications

Several noteworthy simplifications were imposed throughout testing. For static and dynamic force experiments, encoder angles (rather than optical sensor-estimated angles) were used for Jacobian calculations to convert between joint torque and end-

effector force domains. While optical sensor estimates of joint angles in kinematic experiments were quite accurate, joint angle error would further increase end-effector force estimation error by an average of approximately 8%.

At the beginning of each force test (with the arm in its nominal configuration), the baseline force estimate for each muscle was set to the muscle pre-tension value with which the arm was initially configured (7.5 N). This reduced the impact of any shifts in sensor baselines after initial sensor calibration that may have occurred over time. A similar baseline procedure could be completed at each startup for other systems that would use these sensorized muscles, as follows: move the system into the nominal configuration at which the muscles were originally pre-tensioned and set the current length and force estimates to the corresponding pre-tension values.

3.3.2 Potential issues

Sensor hysteresis. Hysteretic behavior was observed for the optical pressure sensor during characterization of optical sensor response in no-load testing. It is plausible that the stiffer Dragon Skin 30 used for the pressure sensor diaphragm, as opposed to the Dragon Skin 10 NV used for the rest of the muscle, dissipates more energy during muscle pressurization. It may be possible to reduce this pressure sensor hysteresis by using Dragon Skin 10 NV or another less hysteretic silicone. However, the use of a lower-stiffness silicone would require a thicker diaphragm to maintain the pressure operating range of the sensor.

Muscle slack. Experiments on the 2-DOF arm elucidated the importance of maintaining tension in muscles for accurate kinematic and dynamic arm measurements. For joint angle and end-effector position estimation, reduced accuracy was observed when one or more muscles became slack. This is because the muscle no longer constrains the joint once the muscle becomes slack and therefore muscle length does not

dictate joint angle. Reduced accuracy was also observed for joint torque and end-effector force estimation when the antagonist muscle became slack. Antagonist muscle force estimates are poorer in the slack state because of two factors: the force versus length sensitivity of the optical length sensor is highest for small contraction lengths, and the length-pressure-force surface fit quality is poorer in the small contraction length/low pressure operating region because of limited and noisy data. These findings suggest that with the proposed optical sensors, it is beneficial to prevent both muscles at each joint from becoming slack to maximize kinematic and dynamic arm estimation accuracy. This may be achieved by implementing a control scheme that prevents all muscles from dropping below a prescribed minimum force threshold.

Physical disturbances. One of the main issues with the optical sensor design presented is its susceptibility to physical disturbances. Although the optical sensor is relatively insensitive to muscle contact away from the sensor diaphragms, significant contact at the diaphragm locations can cause additional diaphragm deformation and reduce length and force estimation accuracy. This was shown to be most significant for the length sensor diaphragm. However, test results also suggested that sensor estimation error caused by external muscle contacts can be mitigated by operating at higher pressures. Additionally, for a use case in which physical disturbances are more likely, it may be best to only use sensor data from the higher-pressure muscle of the antagonistic pair at each point in time.

3.3.3 Observations

Throughout this work, several observations were made that may be relevant to other researchers performing related research. During the initial design stage, it was assumed that using the black plastic material 3D-printed on the Objet30 Prime (RGD875 VeroBlackPlus) would be sufficient to block IR light. However, significant

IR light transmission through 3D-printed parts several millimeters thick was observed. Therefore, it was necessary to include additional design features, such as an aluminum shield between the LED and photodiode in the muscle end cap, to prevent undesired light transmission.

Black and white silicone pigments were used strategically in the muscle design to improve sensor response characteristics. White pigment significantly increased the IR reflectivity of silicone versus no pigment, whereas black pigment significantly decreased the IR reflectivity. In testing, it was found that silicone with the maximum recommended amount of black pigment was still slightly reflective at close sensor distances (about 1 cm) for this sensor design.

Radial stretching of the length sensor diaphragm during muscle inflation seemed to reduce the reflectivity of the diaphragm. This observation was made after comparing the sensor response with and without the use of a thin strip of tape as a radial constraint at the diaphragm. By constraining the muscle diameter at the length diaphragm, the overall length sensor response was significantly larger (higher peak sensor voltage at maximum contraction). It is plausible that the stretching of the diaphragm allowed some light to pass through the diaphragm material, instead of reflecting back. The radial constraint was not used on the sensorized muscles in this work because it slightly reduces the contraction range of the muscle; instead, the IR LED brightness was tuned to increase length sensor range.

Early length sensor testing showed an undesired response in which the length sensor signal first decreased slightly before increasing throughout the remainder muscle contraction. A black annulus of silicone was added to the outer edge of the length sensor diaphragm to mitigate any unintended reflectance effects at the diaphragm-muscle interface. This eliminated the initial dip in length sensor signal and achieved a monotonically increasing signal versus muscle contraction length.

3.4 Significance

The optical sensor-embedded pneumatic muscles developed in this study were utilized to estimate the end-effector position of a 2-DOF arm with less than 1.4 mm-average error for various end-effector speeds and locations in the workspace. Static and dynamic end-effector force estimation using the optical sensors was also demonstrated with average errors of 0.16 N or less for maximum forces in the 2-N range. For additional degrees of freedom, angle and torque estimation errors at each joint would compound end-effector position and force estimation errors, as is the case for any other serial manipulators with joint-level sensing. Although these levels of accuracy cannot match those of off-the-shelf encoders and force sensors, they may be sufficient for bioinspired and wearable robotics applications. Consider as an example a wearable upper body exosuit used to augment the strength of a warehouse worker manipulating heavy materials. For this type of lower-precision task, accuracy on the centimeter/Newton scale may be acceptable.

The optical sensors presented in this work offer several key advantages over traditional solid-state sensing. Because these sensors are designed into the muscle, there is no engineering effort required to integrate sensing into a muscle-actuated device, nor is there additional external sensing hardware that may constrain device design. For the upper body exosuit application, it would be challenging to outfit such a device with encoders and force sensors without limiting range of motion and encumbering the user via additional weight and rigid components. Optical sensor-integrated muscles can potentially overcome these challenges by providing position and force sensing in a flexible, low-mass actuator.

Additionally, the cost of each optical sensor for all components aside from the 3D-printed end fittings is less than $20, with components purchased in single quantities. Much of this cost is attributed to the LED/photodiode plastic housing (for

connection with optical fibers) that is not used in the sensor design. For similar LEDs/photodiodes without housings, the single-quantity sensor cost drops to less than $8. Compared with the several thousand-dollar force/torque sensor used in testing, or similarly expensive force sensors, the optical sensors described here present a substantially more cost-efficient alternative for measuring and controlling forces in pneumatic-muscle powered devices.

Optical sensor-embedded muscle measurement performance is comparable to a few of the other more accurate sensorized muscle designs that quantify accuracy. The muscle length estimation calibration for the sensorized muscle in this work resulted in approximately 0.5-mm RMS estimation error for the 22-cm long muscle (contraction range of about 7 cm). This falls in the same range as other pneumatic muscle length sensing approaches that similarly quantify measurement error of less than 1 percent of total muscle length [8], [13], [17]. The 3-N RMS force estimation calibration error measured for the sensorized muscle in this work is also similar to the force resolution reported for the only other sensorized muscle found that incorporates both length and force estimation [17]. However, a significant benefit of the optical sensor developed here is its straightforward adaptability to measurement of other soft actuator deformation modes, such as for estimation of soft bending actuator displacement [32].

CHAPTER 4
MUSCLE-DRIVEN ROBOT MODELING AND CONTROL

The second and third objectives of this work, detailed in the following chapters, focus on design optimization and motion planning for pneumatic muscle-driven robots. Critical to both of these objectives is the development of a sufficiently accurate system model. The components of a complete system model for a muscle-driven robot include: pneumatic system dynamics, muscle dynamics, and robot dynamics.

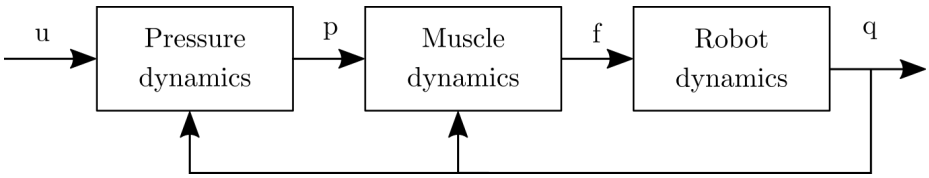

Figure 4.1: Pneumatic muscle-drive robot system dynamics.

Unlike robots actuated by electric motors in which available motor torque is ideally independent of motor position, the muscle force output of pneumatic muscle-driven robots is coupled with robot joint state. Robot motion is produced by muscle forces (as well as external forces). Muscle force is a function of joint angle since muscle force depends not only on pressure, but also on length. Muscle pressure is a function of both the control input (valve state) and joint angle, since muscle volume depends muscle length. The dependency of the pressure dynamics and muscle force output on robot kinematic state results in a complex overall system model, as shown in Figure 4.1.

In this chapter, the low-level muscle pressure control approach is first outlined to motivate the choice of pneumatic system dynamics model. Each component of the overall system dynamics is then addressed individually; they are subsequently connected in the following chapters to model a muscle-driven robot system.

4.1 Pressure control strategy

Pneumatic muscle pressure control strategy informs the development of the pneumatic dynamics model. As detailed in Section 4.3, muscle force output is a function of muscle pressure and contraction length. Since contraction length is constrained by robot pose, muscle-driven robots are controlled solely by modulation of muscle pressure. Therefore, it is crucial to select a low-level pressure control approach best-suited for the category of robots targeted in this work: mobile systems capable of high-speed motion. For high-speed robot motion, fast muscle pressurization is an essential requirement of the controller Additionally, for mobile robotic systems that must carry their control hardware, minimizing the mass of control hardware is also critical. These factors are considered for several potential pressure control approaches.

Continuous control of muscle pressure can be performed using a proportional valve. Proportional valves precisely modulate airflow via continuously variable position spools or armatures, but are significantly more expensive than discrete valves. More critically, proportional valves are much heavier than discrete valves with equivalent max flow rates. And with one valve required to control each pneumatic muscle, this mass quickly adds up, limiting the performance of mobile robot systems that must carry their control hardware.

A discrete valve can be operated by pulse-width modulation (PWM) to more coarsely regulate pressure in a continuous fashion, provided the valve has sufficiently fast open/close response times. However, as the valve and associated pneumatic tubing are sized up to reduce muscle response time for higher-speed robot motion, the faster airflow dynamics make smooth pressure regulation a challenge. Without very fast valve response times that are not feasible for larger valves, large pressure oscillations become unavoidable. Consequently, PWM pressure control is not feasible for high-flow systems.

Based on these issues, a simple on-off 'burst-inflation' control approach is instead chosen for this work, in which a high-flow discrete valve is fully opened in one direction to quickly pressurize the muscle, closed to seal the muscle, and fully opened in the other direction to vent the muscle. A corresponding trajectory planning strategy is developed for burst-inflation control in Chapter 5 to determine valve open/close time sequences for performing a desired robot maneuver. These valve control sequences are easily implemented on a robot and do not unrealistically rely on accurate pressure control via PWM. Additionally, system mass is reduced by avoiding proportional valves. And while burst-inflation control is not as precise as closed-loop pressure modulation, robot compliance inherent to pneumatic muscles can be leveraged to compensate for uncertainty in robot trajectory—as long as the muscle-driven robot executes a desired trajectory just 'accurately enough', the robot can rely on mechanical adaptation, rather than precise feedback control, to account for deviation from nominal trajectory.

4.2 Pneumatic system dynamics

Background. With the choice of muscle pressure control strategy laid out, several approaches to modeling pneumatic system dynamics can be considered. The simplest approach is to fit a curve to experimental muscle pressure versus time data. This provides a very accurate muscle pressure response in simulation for a fixed pneumatic system configuration, which includes source tank size, source pressure, tubing length, diameter, tube fittings, etc. However, for any changes to the pneumatic system configuration, additional experiments must be run to re-characterize the muscle pressure response curve. Furthermore, this purely data-driven approach treats muscle pressure as uncoupled from the rest of the robotic system, contrary to the interaction between muscle, pressure, and robot dynamics shown in Figure 4.1. Thus, any change in robot dynamics from the characterization experiment to subsequent robot maneuvers would

again require re-characterization of muscle pressure response.

Several research groups have instead approximated pneumatic dynamics with lumped-parameter pneumatic circuit models [33], [34]. System volume (source tank and muscle) is modeled as a capacitor using the ideal gas law, while pressure loss due to viscous effects is modeled by a linear or nonlinear resistor; resistance values are empirically determined from experimental data. Gas inertia is sometimes included via an inductor element, as well.

Another common approach is to derive a differential equation for the evolution of internal muscle pressure in time from Boyle's law—for an ideal gas undergoing an isothermal process, the product of pressure and volume is constant. Boyle's law is applied by equating the product of muscle air pressure and volume at atmospheric pressure to the pressure-volume product at the elevated internal muscle pressure [35], [36]

$$\begin{aligned} p_a V_a &= p_m V_m \\ p_m &= \frac{p_a V_a}{V_m} \end{aligned} \tag{4.1}$$

where p_a is atmospheric pressure, V_a is muscle air volume at atmospheric pressure, p_m is internal muscle pressure, and V_m is internal muscle volume. Muscle pressure is then differentiated in time

$$\begin{aligned} \dot{p}_m &= \frac{\dot{\cancel{p_a}} V_a}{V_m} + \frac{p_a \dot{V}_a}{V_m} - p_m \frac{\dot{V}_m}{V_m} \\ &= \frac{p_a \dot{V}_a}{V_m} - p_m \frac{\dot{V}_m}{V_m} \\ &= p_m \left(\frac{\dot{m}}{m} - \frac{\dot{V}_m}{V_m} \right) \end{aligned} \tag{4.2}$$

where $\dot{m}$ is the mass flow rate of air into/out of the the muscle. To integrate the above differential equation for muscle pressure in time, muscle volume, rate of change of muscle volume ($\dot{V}_m$), and mass flow rate are required. Flow rate is frequently mod-

eled using an empirical valve equation with one or more experimentally-determined coefficients [36]–[38].

Muscle volume and volumetric rate of change can be determined geometrically, assuming the pneumatic muscle is a cylinder [37]

$$V_m = \frac{(b^2 L - L^3)}{4\pi n^2} \tag{4.3}$$

$$\dot{V}_m = \frac{(b^2 - 3L^2)}{4\pi n^2}\dot{L} \tag{4.4}$$

where b is the length of the helically-wound threads in the muscle, L is muscle length, and n is the number of thread turns around the muscle. L and $\dot{L}$ are state variables of the robotic system. This equation is typically modified to account for distortion from cylindrical shape at the ends of the muscle, such as in [39]. Alternatively, muscle volume can be empirically modeled using experimental data for best accuracy [35], [40].

Approach. The high-flow discrete valve selected for this work has a large orifice to maximize airflow rate for fast robot dynamics; therefore, the dominant flow restriction in the pneumatic system is attributed not to the valve restriction, but to the frictional pressure drop along the tubing connecting the valve to the muscle. Consequently, the chosen strategy was to model the mass flow rate of air into the muscle by adapting the Darcy-Weisbach equation for tube pressure loss to a compressible fluid. The mass flow rate through the tube can be expressed as

$$\dot{m} = \rho v A \tag{4.5}$$

where ρ is the fluid density, v is the fluid velocity, and A is the cross-sectional area of the tube. The Darcy-Weisbach equation is given by [41]:

$$\Delta p = f_D \frac{L}{D} \frac{\rho v^2}{2} \tag{4.6}$$

where Δp is pressure drop, f_D is the Darcy friction factor, L is tube length, and D is tube inner diameter. The Darcy friction factor is approximated via the Haaland equation

$$f_D = \left[-1.8 log_{10} \left(\frac{6.9}{Re} + \left(\frac{\epsilon}{3.7D} \right)^{1.11} \right) \right]^{-2} \tag{4.7}$$

where ϵ is the tube surface roughness, and Re is the Reynolds number

$$Re = \frac{\rho u D}{\mu} \tag{4.8}$$

in which μ is the dynamic viscosity, and u is the average fluid velocity.

The assumption of an ideal gas undergoing an isothermal process allows for simplification of the analysis, such that the ratio of pressure to density is a constant, and therefore, gas density is proportional to pressure

$$\frac{p}{\rho} = R_s T \Rightarrow \rho = \frac{p}{R_s T} \tag{4.9}$$

where R_s is the specific gas constant ($R_s = R/M$, R is the ideal gas constant, M is the molar mass) and T is gas temperature. The pressure-density ratio for air is plotted against constant $R_s T$ for increasing pressure in Figure 4.2. At low pressures between 200-1000 kPa, the pressure-density ratio closely matches the ideal gas law.

Fluid velocity can then be expressed in terms of pressure and mass flow rate

$$\dot{m} = (kp)VA \Rightarrow V = \frac{\dot{m}}{kpA}. \tag{4.10}$$

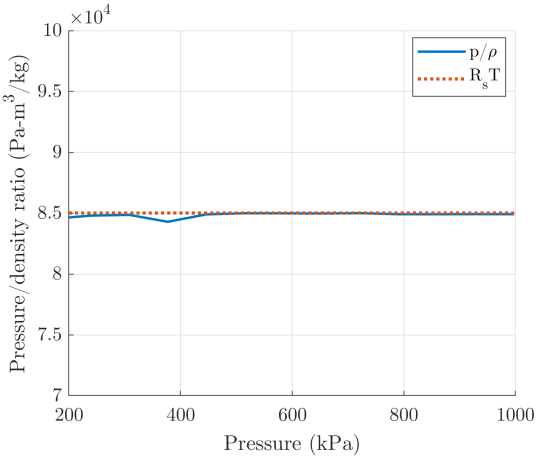

Figure 4.2: Air pressure/density ratio versus pressure.

By expressing the differential pressure drop along the tube using the Darcy-Weisbach equation and substituting Equations 4.9 and 4.10, the differential pressure drop along the tube can be expressed as

$$dp = -f_D \frac{\dot{m}^2}{2kpA^2D} dL \tag{4.11}$$

A second simplification is made by treating air viscosity as constant over the length of the tube. As shown in Figure 4.3, air density varies significantly with pressure, but air viscosity is relatively constant at low pressures—for the 200-1000 kPa input pressure range of the valve, air viscosity changes only by approximately 0.5%. With constant air viscosity, the Darcy friction factor becomes a function of mass flow rate only

$$f_D = \left[-1.8 log_{10} \left(\frac{6.9\pi D\mu}{4\dot{m}} + \left(\frac{\epsilon}{3.7D} \right)^{1.11} \right) \right]^{-2}. \tag{4.12}$$

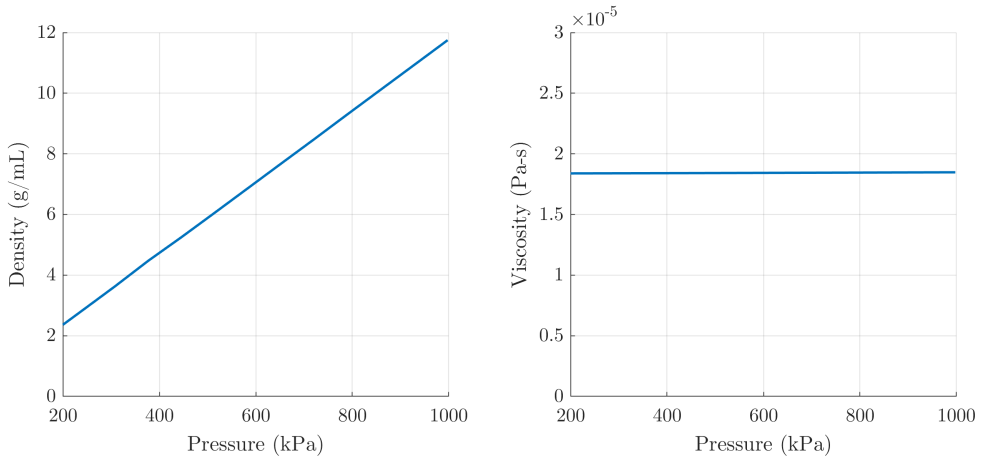

Figure 4.3: Air density and viscosity versus pressure.

Finally, by assuming a uniform mass flow rate through the tube, it is possible to integrate pressure drop along the length of the tube from the source pressure, p_s, to the muscle pressure, p_m, as

$$L = -\int_{p_s}^{p_m} \frac{2A^2D}{f_D\dot{m}^2R_sT}p\ dp = \frac{kA^2D}{f_D\dot{m}^2}(p_s^2 - p_m^2) \tag{4.13}$$

$$\dot{m}^2 = \frac{A^2D}{f_DLR_sT}(p_s^2 - p_m^2). \tag{4.14}$$

Equation 4.14 is implicit in $\dot{m}$, as f_D is a function of mass flow rate, so $\dot{m}$ is solved for numerically. At each simulation timestep, the mass flow rate into each pneumatic muscle is integrated and the corresponding muscle pressure is calculated from the ideal gas law.

Pneumatic muscle volume is modeled from experimental data. For the 'mesh' muscle design used in Chapters 5 and 6, a prototype muscle was completely filled with water at several lengths between full extension and full contraction and the mass of water was measured by subtracting empty muscle mass from filled muscle mass. Water mass was converted to volume using water density at room temperature. A third-order polynomial was fit to measured muscle volume versus contraction fit data,

shown in Figure 4.4, as

$$V = \beta_0 + \beta_1 c + \beta_2 c^2 + \beta_3 c^3. \tag{4.15}$$

where c is muscle contraction. The polynomial coefficients for the mesh muscle design are provided in Table 4.1.

Table 4.1: Muscle volume polynomial coefficients for 'mesh' muscle design.

β_0	β_1	β_2	β_3
42.43	31.41	-3.25	0.13

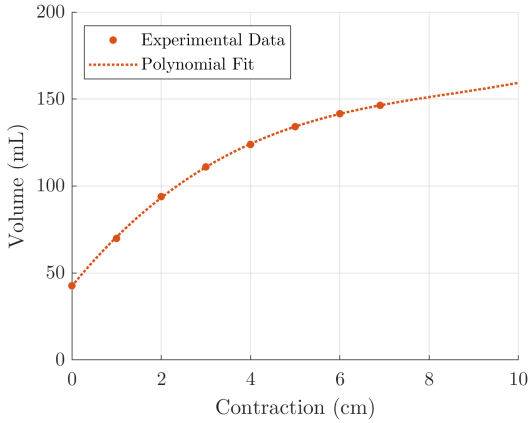

Figure 4.4: Muscle volume versus muscle contraction for mesh muscle: experimentally-measured data and third-order polynomial fit.

Note that the final experimental data point in Figure 4.4 is at the maximum contraction length of the mesh muscle, at about at 7 cm contraction—this corresponds to the maximum muscle volume. Consequently, the polynomial fit beyond this point does not accurately represent muscle volume.

Assumptions. It is important to review the assumptions that were made to simplify analysis of muscle pressure dynamics. Treatment of air as ideal gas is valid for low muscle operating pressures (valve operation is limited to <1000 kPa) and relatively high temperatures around 300 K. With regard to the assumption of constant

air viscosity, there is negligible change in viscosity over the pressure operating range, assuming constant temperature. Even with a temperature drop from 23 °C to 0 °C, air viscosity only decreases approximately 6 percent—this results in only a 0.2 percent change in the friction factor (Equation 4.12).

The assumption of uniform mass flow rate along the length of the tube neglects transient airflow dynamics that occur right as the valve as opened and as it is closed, but should not significantly affect the overall shape of the muscle inflation curve. However, treatment of muscle inflation as an isothermal process is a significant simplification, since temperature drop along the tube as air expands is not negligible. Additionally, there are several other unmodeled pneumatic restrictions in the system beyond the valve-to-muscle tube friction, including pneumatic connectors between the air tank and valves, valve flow path, and tubing bends. Rather than drastically expanding the complexity of the pneumatic model by incorporating air temperature change and modeling all pneumatic components, unmodeled effects were incorporated by tuning the modeled tube diameter to match experimental airflow dynamics.

Evaluation. The tube pressure drop model developed above was evaluated against a more sophisticated model from MATLAB's 'Pipe' gas element. The Pipe model includes viscous friction losses and convective heat transfer between gas and tube wall and accounts for the evolution of gas temperature over the length of the tube. As shown in Figure 4.5, muscle inflation response is very similar between the two models, with the most noticeable difference right after the valve is opened—the initial pressure increase with the MATLAB Pipe model is more gradual.

The tube pressure drop model was then compared with experimental muscle pressure step response data. A 74-inch length of 3/16-inch inner diameter tubing was connected between the valve and the muscle. As shown in Figure 4.6a, the model resulted in faster muscle inflation than that observed experimentally. To empirically

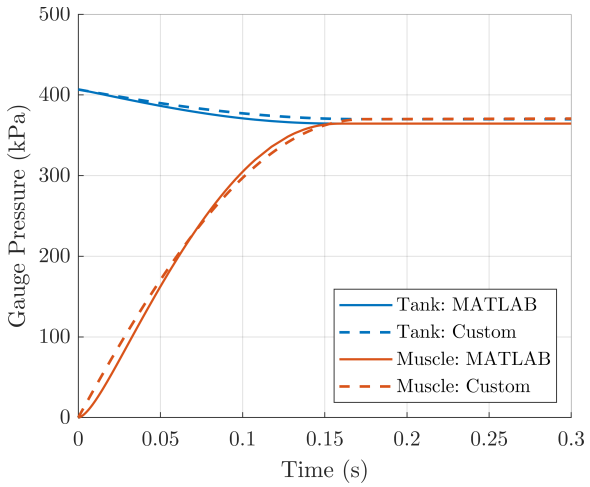

Figure 4.5: Pneumatic muscle pressure step response: simplified tube pressure drop model vs. MATLAB Pipe model.

include the unmodeled pneumatic restrictions (valve orifice, pneumatic fittings connecting the valve to the tube and the tube to the muscle, and bends in the tube) that contribute to slower muscle inflation, the modeled inner tubing diameter was reduced. As shown in Figure 4.6b, agreement between simulated and experimental step responses significantly improved with a diameter reduction of 0.03 in. Note that the experimental muscle shows a slower rise in muscle pressure over the first 25 ms of of the step response, before experimental pressure catches up with modeled pressures. It is possible that position of the pressure transducer at the far end of the muscle (opposite to muscle inlet) results in additional transient effects inside the muscle that are reflected in the experimental data.

4.3 Muscle dynamics

Background. Many types of force models—analytical, phenomenological, and empirical—have been developed for the pneumatic artificial muscle over the past several decades. The earliest and most frequent approach applies the principle of virtual work, equating muscle work out (muscle force applied over muscle contraction) to work in (change in muscle muscle volume via pressurization). The resulting model

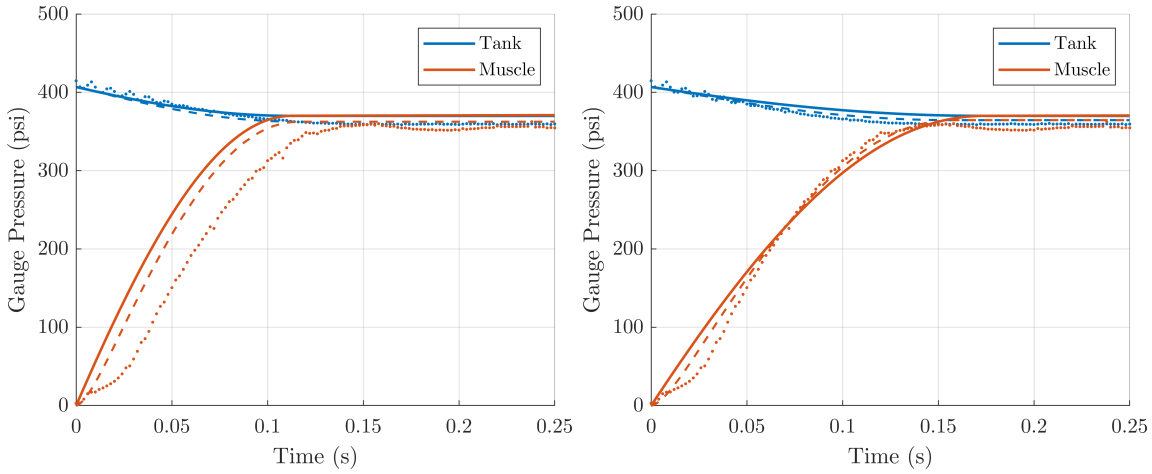

Figure 4.6: Pneumatic muscle pressure step response comparing experimental data (circle markers) to MATLAB Pipe model (dashed line) and custom model (solid line): **(a)** nominal tube diameter, **(b)** tube diameter reduced by 0.03 in.

yields muscle force that is proportional to pressure at a fixed contraction length, but decreases quadratically over the contraction range of the muscle

$$\begin{aligned} -FdL &= PdV \\ \Rightarrow F &= \frac{p}{4\pi n^2}\left(3L^2 - b^2\right) \end{aligned} \tag{4.16}$$

where F is muscle contraction force, p is muscle pressure, L is muscle length, b is the length of the helically-would threads around the muscle, and n is the number of thread turns. For this derivation, the muscle is assumed to be perfectly cylindrical in shape throughout contraction. This model excludes many physical phenomena.

Subsequent work has sought to add these unmodeled effects, including friction between woven mesh fibers and between the woven mesh and elastic bladder [23], [33], bladder elasticity [42], [43], mesh fiber elasticity [34], [43], divergence from cylindrical shape during inflation [38], [43], change in bladder thickness during inflation [43], and a general correction factor for force over-prediction [37]. Incorporating these features leads to relatively more accurate muscle force estimation accuracy, but with more complex models. It is important to note that most of these models use empirically-

determined parameters that require extensive experimental data.

Other work has directly analyzed the forces acting on the muscle bladder, similarly adding friction, bladder elasticity, and non-cylindrical shape effects to improve accuracy with similar results [39], [43]–[45]. Research groups have also explored the use of phenomenological models using empirically-tuned spring, damper, and force elements [37], [46]; a few have tried to represent the pneumatic muscle by adapting the Hill biological muscle model [35], [47].

As most of the above approaches already require experimental data to tune various model parameters, recent works have fit simpler empirical models between muscle contraction force, contraction length, and pressure directly to experimental data [31], [48]–[50]. Data is typically gathered via quasi-static tests which reflect most of the effects described above, such as bladder stiffness, fiber stiffness, and muscle deviation from cylindrical shape. Consequently, empirical models tend to be most accurate.

Approach. An empirical modeling approach is also used in this work. A comprehensive pressure-length-force characterization was performed for the mesh pneumatic muscle design by running a series of quasi-static blocked force tests, similar to the optical sensor characterization described in Chapter 3. The muscle was fixtured in an Instron materials testing system, maintained at a fixed pressure, and allowed to contract at a constant speed from its maximum (nominal length). Muscle length and force were recorded for fixed muscle pressures up to 345 kPa and a third-order surface was fit to contraction force versus pressure and contraction data

$$f_m = \beta_{00} + \beta_{10}c + \beta_{01}p_m + \beta_{20}c^2 + \beta_{11}cp_m + \beta_{30}c^3 + \beta_{21}c^2p_m. \tag{4.17}$$

where f_m is muscle force, p_m is muscle pressure, and c is muscle contraction; the surface fit is shown in Figure 4.7.

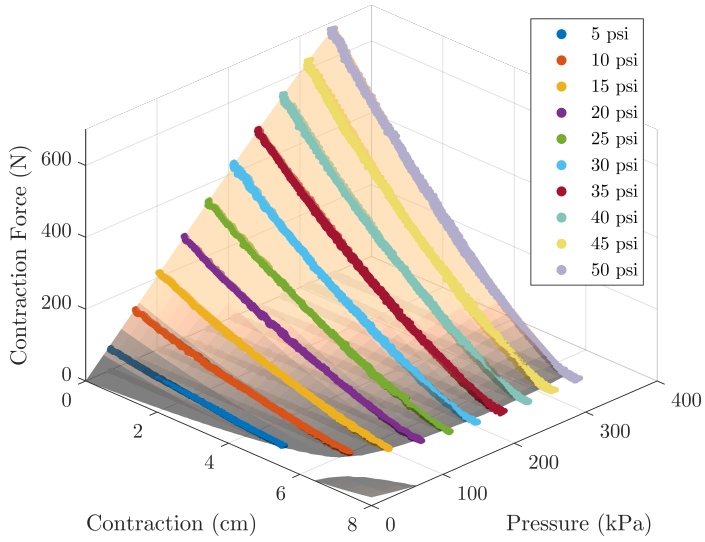

Figure 4.7: Third-order surface fit to pneumatic muscle blocked force versus pressure and contraction data.

Assumptions. While quasi-static tests do not fully capture the dynamic properties of the muscle—mainly, the hysteresis due to various frictional effects—this is not necessarily an issue for the dynamic robots that are the focus of this work. Explosive robot movements can only be achieved for the direction of muscle contraction; muscle elongation (deflation) is passive, and therefore slower, so elongation is not useful for high-speed robot movement. Thus, to most accurately model contraction force, muscle force was calibrated specifically for the direction of muscle contraction, rather than averaging between contraction and elongation force curves.

4.4 Rigid body dynamics

The use of a rigid robot frame to transmit pneumatic muscle forces allows for analysis with standard rigid body dynamics techniques. This work utilizes the modern geometric interpretation of classical screw theory, as in [51], in which rigid-body motions are expressed using matrix exponentials.

The twist-wrench formulation of Newton-Euler dynamics for a single rigid body

can be expressed in body frame coordinates {b} as

$$\mathcal{F}_b = \mathcal{G}_b\dot{\mathcal{V}}_b - [\mathrm{ad}_{\mathcal{V}_b}]^T\mathcal{G}_b\mathcal{V}_b$$

$$\mathcal{F}_b = \begin{bmatrix} \tau_b \\ f_b \end{bmatrix}, \mathcal{G}_b = \begin{bmatrix} \mathcal{I}_b & 0 \\ 0 & \mathfrak{m}I \end{bmatrix}, \mathcal{V}_b = \begin{bmatrix} \omega_b \\ v_b \end{bmatrix} \tag{4.18}$$

where $\mathcal{F}_b$ is the wrench acting on the body, $\mathcal{G}_b$ is the spatial inertia matrix of the body, $\mathcal{V}_b$ is the body twist, and $\dot{\mathcal{V}}_b$ is the body twist acceleration. Given two twists $\mathcal{V}_1$ and $\mathcal{V}_2$, the Lie bracket of $\mathcal{V}_1$ and $\mathcal{V}_2$ is defined as $[\mathrm{ad}_{\mathcal{V}_1}]\mathcal{V}_2$, where

$$[\mathrm{ad}_{\mathcal{V}}] = \begin{bmatrix} [\omega] & 0 \\ [v] & [\omega] \end{bmatrix} \tag{4.19}$$

in which $[\omega]$ and $[v]$ are the skew-symmetric matrix representations of angular and linear velocity vectors. The recursive formulas for the Newton-Euler dynamics formulation of an n-link open chain with body-fixed reference frame $\{i\}$ attached to center of mass of each link i are detailed, starting with the kinematics.

The configuration of frame $\{i\}$ relative to $\{i-1\}$ given the joint position θ_i between the two links is

$$T_{i,i-1}(\theta_i) = e^{-[\mathcal{A}_i]\theta_i}M_{i,i-1} \tag{4.20}$$

where $T_{i,i-1} \in SE(3)$ (the special Euclidean group of homogeneous transformation matrices) is the configuration of frame $\{i-1\}$ in $\{i\}$ for arbitrary joint angle, $M_{i,i-1} \in SE(3)$ is the configuration of frame $\{i-1\}$ in $\{i\}$ with the robot in its home position (all joint positions at zero), and $\mathcal{A}_i$ is the screw axis for joint i in frame $\{i\}$.

The twist and acceleration of link i are given by

$$\mathcal{V}_i = [\mathrm{Ad}_{T_{i,i-1}}]\mathcal{V}_{i-1} + \mathcal{A}_i\dot{\theta}_i \tag{4.21}$$

$$\dot{\mathcal{V}}_i = [\mathrm{Ad}_{T_{i,i-1}}]\dot{\mathcal{V}}_{i-1} + [\mathrm{ad}_{\mathcal{V}_i}]\mathcal{A}_i\dot{\theta}_i + \mathcal{A}_i\ddot{\theta}_i, \tag{4.22}$$

where $[\mathrm{Ad}_T]$ is the adjoint representation of the homogeneous transformation matrix T

$$[\mathrm{Ad}_T] = \begin{bmatrix} R & 0 \\ [p]R & R \end{bmatrix}, \tag{4.23}$$

in which R is the rotation matrix and $[p]$ is the skew-symmetric matrix representation of the translation vector p. The twist of link i is the sum of the twist of the previous link $\mathcal{V}_{i-1}$ and the twist due to the joint i velocity.

For each link i, the total wrench acting on the link is the sum of the wrench transmitted through joint i and the wrench applied through the subsequent joint $i+1$, or the wrench applied to the end-effector link n, as given by

$$\mathcal{F}_i - [\mathrm{Ad}_{T_{i+1,i}}]^T\mathcal{F}_{i+1} = \mathcal{G}_i\dot{\mathcal{V}}_i - [\mathrm{ad}_{\mathcal{V}_i}]^T\mathcal{G}_i\mathcal{V}_i. \tag{4.24}$$

The joint force or torque (depending on prismatic or revolute joint) at each joint is calculated from the wrench transmitted through joint i and the joint's screw axis

$$\tau_i = \mathcal{F}_i^T\mathcal{A}_i. \tag{4.25}$$

The recursive equations in (4.20)-(4.25) serve as kinodynamic constraints to enforce robot dynamics in the subsequent trajectory optimization and design chapters.

4.5 Discussion

As noted in Section 4.2, there are several key simplifications made in formulating the pneumatic system model, namely, the assumption of uniform mass flow rate along the length of the tube and the treatment of inflation as an isothermal process. Additionally, there are several other sources of airflow resistance in the pneumatic system, beyond that of the valve-to-muscle connecting tube, that are not modeled. Instead of significantly increasing model complexity, unmodeled airflow resistance effects are compensated by adjusting the modeled tubing diameter. With the tuned tubing diameter, agreement between simulated and experimental muscle inflation step responses is substantially improved. The pneumatic system model is further evaluated for a multi-muscle system in Chapter 5.

4.6 Significance

This chapter details airflow, pneumatic muscle, and rigid body dynamics subsystem models that are used together to construct a complete model for pneumatic muscle-driven robots. The overall model is vital to the muscle-driven robot trajectory planning approach laid out in Chapter 5 and to the robot design optimization strategy examined in Chapter 6.

CHAPTER 5
JUMPING ROBOT TRAJECTORY OPTIMIZATION

The second objective of this work is to develop a framework for planning high-speed maneuvers on mobile muscle-driven robots controlled by 'burst inflation,' in which high-flow solenoid valves are used to control the timing (but not rate) of rapid muscle pressurization. For this burst inflation control approach, planning a robot trajectory entails determining valve open and close timing sequences for each pneumatic muscle on the robot.

Recently, legged robots have become a significant research focus in the robotics community because of their versatility outside of a structured laboratory setting. Legs allow robots to step over small irregularities, leap over large obstacles, and jump onto elevated surfaces, making legged robots capable of traversing a broad range of unstructured terrains in which wheeled robots fail. Thus, legged robots have potential in a wide range of applications that involve navigation in unknown environments with unpredictable terrain, including search and rescue, military reconnaissance, and extraterrestrial exploration.

As the development of legged robots has evolved, increasing attention has been given to the incorporation of mechanical compliance into robot legs. Researchers have taken cues from biology, attempting to capture the benefits of mechanical compliance to improve legged robot agility, dynamic stability, power efficiency, and mechanical adaptation to environmental uncertainty [52]–[59]. One of the most studied compliance mechanisms is the series-elastic actuator, typically a motor in series with a spring [54], [57]–[59], while other designs utilize pneumatic springs [52], [60], or make the entire leg structure itself compliant [61]. Alternatively, the pneumatic artificial muscle represents a viable alternative for robot compliance. The pneumatic muscle's

low mass (in the range of 50 to 100 grams) minimizes distal inertia along the leg, while its passive compliance eliminates the need for active impedance control used with series-elastic actuators.

An important problem in the context of legged robots is planning control trajectories, especially for complex high-speed maneuvers like jumps. This planning capability, required to realize the agility capabilities of legged robots in practice, has not been adequately addressed for pneumatic muscle-driven robots. While several research groups have investigated the use of pneumatic muscles in legged robots, including for jumping [62]–[66], the majority of pneumatic muscle-driven jumping robot efforts have focused on maximizing jumping capabilities, with little consideration for jumping trajectory planning.

Though a few studies have shown that jumping directionality control is possible [67], [68], only one other work has been found that details jump trajectory planning for a pneumatic muscle-driven quadruped robot—the robot was controlled via continuous muscle pressure modulation using pneumatic proportional valves [69]. This is similar to optimal control approaches for pneumatic robot manipulators tethered to large banks of proportional valves [70]–[74]. Proportional valves allow for continuous control signals that are directly compatible with standard trajectory optimization approaches. However, as explained in Chapter 4, proportional valves are poorly-suited for mobile robots due to their size and weight; mass is particularly important for robots designed to be capable of fast dynamic motions like jumping and leaping.

Therefore, this work aims to enable trajectory planning of explosive maneuvers, such as jumping, for muscle-driven mobile robots controlled by high-flow discrete solenoid valves. In contrast with continuous pressure control approaches, 'burst inflation' is used to rapidly pressurize each pneumatic muscle based on an optimized valve timing sequence for a desired trajectory. A factor graph-based trajectory optimization approach is developed to model pneumatic muscle-driven robot dynamics

and to plan valve open and close times for a desired robot maneuver. As standard planning approaches assume continuous control input signals, the trajectory planner in this work accommodates the discrete nature of burst-inflation control. The efficacy of the planning framework is evaluated on a pneumatic muscle-driven legged jumping robot test platform.

Jumping robot test platform. The jumping robot test platform used in this work is a planar two-legged system actuated by four pneumatic muscles, as shown in Figure 5.1. Each leg of the robot consists of a 'shank' link and a 'thigh' link connected by the revolute 'knee' joint; the thigh is connected to a 'torso' link at the revolute 'hip' joint. All five links are 0.55 meters long. The robot design utilizes carbon fiber tubing for each link and 3D-printed polylactic acid (PLA) joints to minimize robot mass. A pneumatic muscle is connected at each joint via a pulley; the pulley radius determines the moment arm by which the muscle contraction force generates joint torque. Additionally, an elastic element is connected to a second pulley at each joint to form an antagonistic torsion spring that opposes leg swing—these torsion springs prevent leg collisions mid-air and return the legs back toward their starting pose after liftoff. Each pneumatic muscle is connected to a B3 Series (Parker Hannifin) solenoid valve for on/off burst-inflation control. All four valves then connect to a single

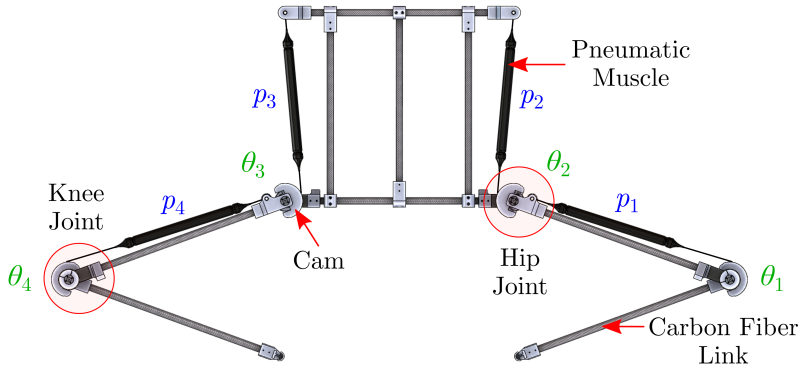

Figure 5.1: Planar two-legged jumping robot test platform.

pressurized carbon-fiber tank. For all testing, the valves and tank were positioned off-board the robot (tethered test setup).

Each link mass was measured by hanging the link from a load cell, with the corresponding pneumatic muscle and connecting hardware attached; link masses are listed below, in Table 5.1. The total mass of the tethered robot is approximately 2.3 kg. To calculate link inertias, each link was treated as a 2-cm radius cylinder with uniform density, corresponding to

$$J = \frac{1}{12} m \left(3r^2 + l^2\right) \tag{5.1}$$

where J is the link inertia of the cylinder about the axis through its center diameter, m is the link mass, r is the radius, and l is the link length. The Simulation Description Format (SDF) file describing the robot frame morphology and inertial properties is included as Appendix A.

Table 5.1: Jumping robot link masses.

Robot Link	Mass (kg)
Shank	0.285
Thigh	0.428
Torso	0.883

5.1 Methodology

5.1.1 Factor graph framework

The next three sections lay out an approach to planning pneumatic muscle-driven robot trajectories using factor graphs—a factor graph is a bipartite graph consisting of variable nodes and factor nodes, where each variable node represents an unknown variable and each factor node represents a constraint on the variables [75]. A factor graph can be constructed to represent the dynamics of a robot by simply specifying

the kinematic and dynamic equations of the robot as constraints between the corresponding robot state variables. For a pneumatic muscle-driven robot, the pneumatic model, muscle force model, and rigid body dynamics from Chapter 4 are encoded in a graph as constraints between pneumatic, muscle, and robot link states. Copies of the robot dynamics factor graph can then be connected in series via collocation constraints to transcribe a robot trajectory in time.

The overall trajectory factor graph can be utilized for multiple aspects of robot analysis and planning. In this chapter, a graph is constructed for a pneumatic muscle-driven jumping robot and is used to to plan and simulate jump trajectories, as well as to improve the accuracy of kinematics extraction from video test footage. The GTSAM library is used to build the factor graph and perform optimizations [76].

5.1.2 Multi-phase trajectory optimization

The general trajectory optimization problem is formulated as the minimization of an objective function

$$\min_{t_F, \mathbf{x}(t), \mathbf{u}(t)} J = \phi\big(t_F, \mathbf{x}(t_0), \mathbf{x}(t_F)\big) + \int_{t_0}^{t_F} L\big(\tau, \mathbf{x}(\tau), \mathbf{u}(\tau)\big) d\tau \tag{5.2}$$

with a boundary objective (term 1) and a path integral along the trajectory (term 2), where the decision variables are the final time t_f and the state and control trajectories $\mathbf{x}(t)$ and $\mathbf{u}(t)$. The optimization is subject to the system dynamics

$$\dot{\mathbf{x}}(t) = \mathbf{f}(t, \mathbf{x}(t), \mathbf{u}(t)) \tag{5.3}$$

as well as other constraints including: path constraints, boundary constraints, bounds on state and control, bounds on final state, and bounds on final time.

Direct collocation is used to transcribe the continuous trajectory optimization problem into a nonlinear program (NLP) by discretizing the state and control trajec-

tories at collocation points or nodes [77]; this discretized problem can be represented in a factor graph. The overall factor graph corresponding to a symmetric vertical jump (both feet leave the ground simultaneously) by the pneumatic muscle-driven jumping robot is shown in Figure 5.2. Each $\mathbf{x}_k$ in the factor graph represents the full state of the robot at the node corresponding to time t_k. It is important to note that for the bust inflation control approach in this work, the control signal is not continuous—the control inputs consist of discrete valve open and close times $\mathbf{t}_v = [t_{o,1}, t_{c,1}, ..., t_{o,n_m}, t_{c,n_m}]$ for each of the n_m muscles; this complication is addressed in Subsection 5.1.4.

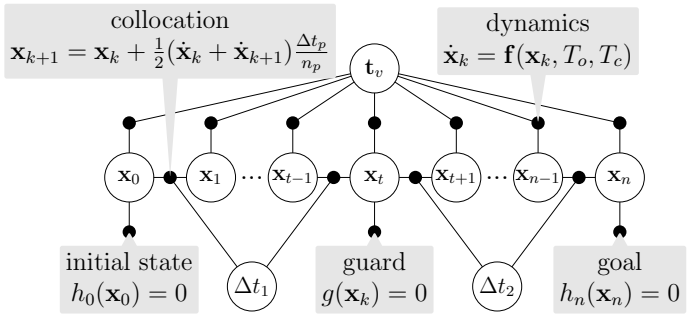

Figure 5.2: Factor graph representing the jumping robot vertical jump trajectory, formulated as a multi-phase optimization problem using hybrid direct collocation: the first phase (Δt_1) represents the jumping robot dynamics with both feet in contact with the ground, while the second phase represents the aerial jumping robot dynamics.

The hybrid direct collocation method [78] is applied to incorporate hybrid robot dynamics that describe robot contact mechanics, such as for the jumping robot where each foot is in contact with the ground for only a portion of the jump sequence. Given a desired contact sequence, multiple phases of the trajectory are explicitly modeled, where each phase represents a distinct set of dynamics. In this way, the overall trajectory optimization is formulated as a sequence of trajectory optimization sub-problems connected by inter-phase constraints. For the jumping robot, there are four sets of dynamics: both feet on ground, only left or right foot on ground, and aerial phase (no feet on ground). The switch between each phase is modeled as instantaneous: a boundary node is associated with each phase transition event

(making or breaking contact) that allows for velocity discontinuities. Each phase p has a duration of Δt_p, evenly dived into n_p steps so that each step with a phase has duration $\Delta t_p/n_p$; the duration of each phase is added as a decision variable to the optimization problem.

Guard constraints $g(\mathbf{x}_k)$ at the boundary nodes dictate phase switches: the guard event for each jumping robot foot leaving the ground is the reduction of the normal contact force to zero; the guard event for each foot contacting the ground is the reduction of foot-ground separation distance to zero. Additionally, inter-phase constraints at the boundary nodes require robot configuration to be maintained through a phase switch (no robot configuration discontinuity).

Robot dynamics constraints (pneumatic, muscle, and rigid body dynamics) are imposed at each node

$$\dot{\mathbf{x}}_k = \mathbf{f}(\mathbf{x}_k, T_o, T_c) = \mathbf{f}_k \tag{5.4}$$

and trapezoidal collocation constraints are imposed between consecutive robot states in time

$$\mathbf{x}_{k+1} = \mathbf{x}_k + \frac{1}{2}(\mathbf{f}_k + \mathbf{f}_{k+1})\frac{\Delta t_p}{n_p}. \tag{5.5}$$

Initial state constraints $h_0(\mathbf{x}_0)$ are set on the first state and target state constraints $h_n(\mathbf{x_n})$ are set on the final state. In the following two subsections, the factor representing the dynamics of the full robot state (Equation 5.4) is expanded into two sub-factor graphs, one for the rigid body dynamics of the robot frame, and the other for the joint torque dynamics dictated by pneumatic muscle and airflow dynamics.

5.1.3 Robot dynamics

Robot dynamics are represented in a sub-factor graph using the rigid body dynamics formulation in Section 4.4, where the recursive pose, twist, acceleration, and wrench equations become factors connecting consecutive robot links

$$T_{i,i-1}(\theta_i) = e^{-[\mathcal{A}_i]\theta_i} M_{i,i-1} \tag{5.6}$$

$$\mathcal{V}_i = [\mathrm{Ad}_{T_{i,i-1}}]\mathcal{V}_{i-1} + \mathcal{A}_i\dot{\theta}_i \tag{5.7}$$

$$\dot{\mathcal{V}}_i = [\mathrm{Ad}_{T_{i,i-1}}]\dot{\mathcal{V}}_{i-1} + [\mathrm{ad}_{\mathcal{V}_i}]\mathcal{A}_i\dot{\theta}_i + \mathcal{A}_i\ddot{\theta}_i \tag{5.8}$$

$$\mathcal{F}_i - [\mathrm{Ad}_{T_{i+1,i}}]^T\mathcal{F}_{i+1} = \mathcal{G}_i\dot{\mathcal{V}}_i - [\mathrm{ad}_{\mathcal{V}_i}]^T\mathcal{G}_i\mathcal{V}_i \tag{5.9}$$

$$\tau_i = \mathcal{F}_i^T\mathcal{A}_i. \tag{5.10}$$

The dynamics sub-factor graph representation of the jumping robot is shown in Figure 5.3, with five poses for the five robot links, and four joint angles for the four actuated robot joints. The red factors exist when the corresponding leg (either link 1 or 5) of the robot is in contact with the ground—these factors connect the leg link to an additional ground-fixed link through a revolute joint with zero torque transmission. Each blue factor exists when the corresponding leg is aerial, removing the revolute joint connecting the leg link to the ground link so that the interaction wrench between the two links is zero. Trapezoidal collocation factors connect the robot poses, twists, and accelerations between consecutive sub-factor graphs in overall trajectory graph.

5.1.4 Joint torque dynamics

The joint torque sub-factor graph shown in Figure 5.4 combines pneumatic system dynamics, muscle dynamics, and joint geometry to model the muscle-generated torque applied at each robot joint. Beginning at the left of the graph, the state of the

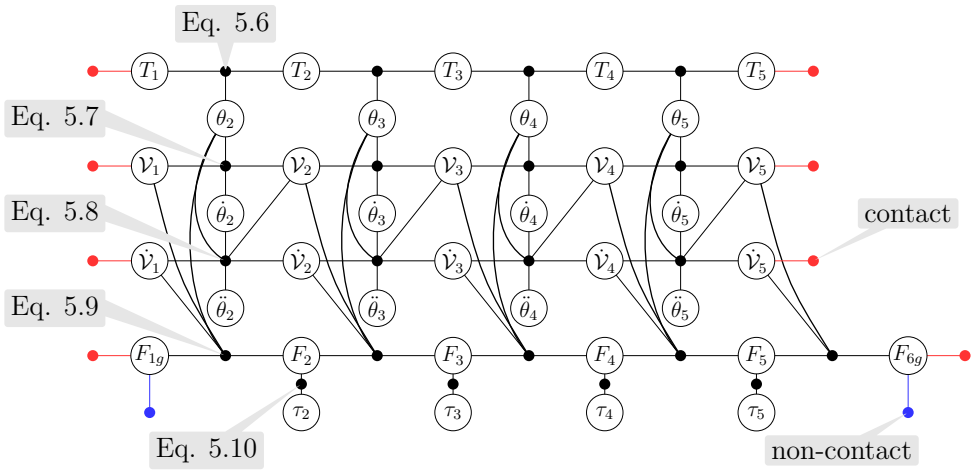

Figure 5.3: Rigid body dynamics representation of the jumping robot in a factor graph. The red factors are active when the corresponding robot foot is in contact with the ground: pose, twist, and acceleration constraints enforce fixed foot position (point contact); wrench constraints enforce no torque transmission from the ground to the foot. The blue factors are active for the aerial phase and enforce zero interaction wrench between the foot and the ground.

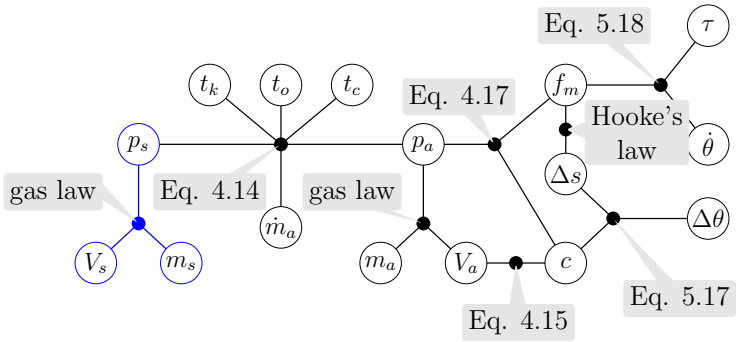

Figure 5.4: Joint torque sub-factor graph, from left to right: the pneumatic source tank state (blue), shared by all joint torque sub-graphs; the airflow dynamics constraint between the source tank and pneumatic muscle; the pneumatic muscle state; and the constraints between muscle force/joint torque and robot state.

pneumatic source tank that feeds all pneumatic muscles is comprised of source tank volume V_s and air mass m_s. An ideal gas law factor

$$p_s = \frac{m_s}{V_s R_s T} \tag{5.11}$$

connects the volume and mass to source tank pressure p_s, where R_s is the specific gas constant and T is the gas temperature.

The pneumatic solenoid valve opening and closing are discrete control events, represented by the valve control times t_o and t_c, that determine the underlying equation for air mass flow rate from source tank to muscle. For the open-valve state, the mass flow rate $\dot{m}_m$ from the source tank into the muscle is calculated given the current source pressure and muscle pressure p_m by integrating along the tube, as described in Section 4.2 (Equation 4.14). For the closed-valve state, the mass flow rate is zero.

Treating the pneumatic dynamics as hybrid dynamics with phase-switching events, like the robot dynamics, would significantly increase the complexity of the problem—the sequence of all valve phases, as well as the progression of valve phases relative to robot dynamics phases, would be required to set up the trajectory optimization problem. Therefore, a soft model is instead used to smoothly approximate the step function using the sigmoid function

$$S(x) = \frac{1}{1 + e^{-x}}. \tag{5.12}$$

The air mass flow rate dynamics are modeled using multiple sigmoids time-shifted by the valve open and close times

$$\dot{m}_m = S(\frac{t_k - t_o}{c_o}) - S(\frac{t_k - t_c}{c_c})\dot{m}_{m,o} \tag{5.13}$$

where $\dot{m}_{m,o}$ is the mass flow rate assuming the valve is open and c_o, c_c are constants that dictate the rate of change between the two sets of pneumatic dynamics.

The source tank volume V_s, air mass m_s, and pressure p_s nodes are shared by all joint torque sub-factor graphs, as one tank feeds all muscles on the robot. A trapezoidal collocation factor connects consecutive source tank air mass nodes in

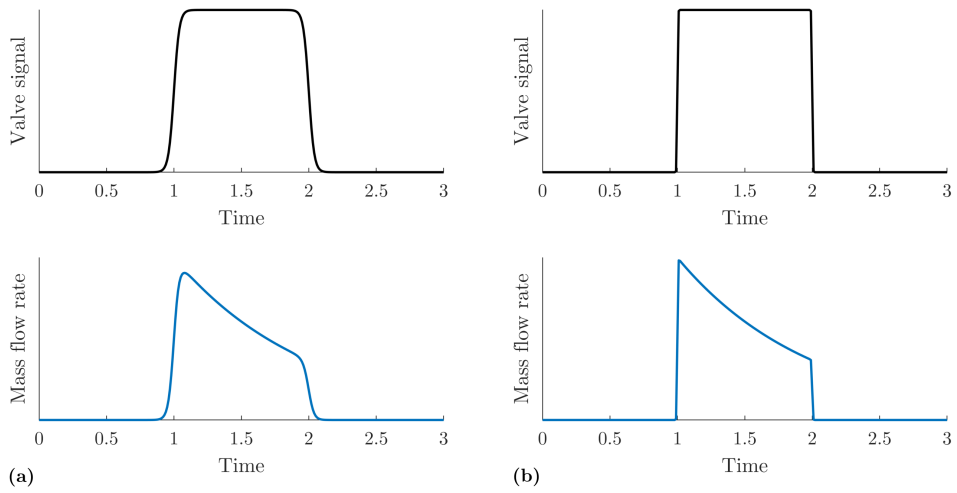

Figure 5.5: Use of sigmoids to smoothly connect valve open/close airflow dynamics: **(a)** large c_o and c_c resulting in smoother change between sets of dynamics, **(b)** small c_o and c_c resulting in faster change between sets of dynamics.

time

$$m_{s,k+1} = m_{s,k} - \sum_{m=1:n_m} \frac{1}{2}(\dot{m}_{m,k} + \dot{m}_{m,k+1})\frac{\Delta t_p}{n_p}, \tag{5.14}$$

$$\tag{5.15}$$

such that the total air mass flow out of the source tank is the sum of air mass flow rates into all muscles. Muscle volume V_m and air mass m_m make up each muscle pneumatic state, connected to muscle pressure through an ideal gas law factor. Muscle volume V_m is a function of muscle contraction Δx, per the experimentally-fit Equation 4.15. Additional trapezoidal collocation factors connect consecutive muscle air mass nodes in time

$$m_{m,k+1} = m_{m,k} + \frac{1}{2}(\dot{m}_{m,k} + \dot{m}_{m,k+1})\frac{\Delta t_p}{n_p}. \tag{5.16}$$

The factor between muscle force f_m, muscle pressure, and muscle contraction is based on the third-order muscle force surface fit detailed in Section 4.3 Equation 4.17

such that force is a function of muscle pressure p_m and muscle contraction c. A linear stiffness spring element is added to the joint model in series with the muscle to represent muscle connector compliance and robot frame compliance; thus, a Hooke's law factor connects spring displacement Δs and muscle force. Accordingly, a factor connecting joint displacement $\Delta\theta$, spring elongation Δs, and muscle contraction constrains the total joint displacement to be the difference between spring elongation and muscle contraction,

$$r\Delta\theta = \Delta s - c \tag{5.17}$$

where r is the radius of the cam through which the muscle force is converted to joint torque. Finally, the joint torque factor

$$\tau = f_m r - c\dot{\theta} \tag{5.18}$$

is added, such that the applied torque is the difference between the torque generated by the muscle through r and the viscous joint damping torque. For the jumping robot, there are four joint torque sub-factor graphs within the overall graph, corresponding to the four pneumatic muscle-driven joints.

5.2 Experiments and Results

Experiments were performed with the two-legged jumping robot to evaluate the efficacy of this factor graph-based planning approach. The jumping robot has two legs with two joints per leg, each driven by a single pneumatic muscle, so for a single inflation cycle of each pneumatic muscle, eight valve control times must be planned (t_o and t_c for each muscle). In each test, valve open and close commands—corresponding to the valve control times determined from trajectory optimizations—were sent via UART from a PC running a timer loop in ROS to an MSP432 microcontroller (Texas

Instruments). Based on these commands, the microcontroller activated each valve via an H-bridge circuit; the microcontroller also recorded muscle and tank pressures at 100 Hz.

For all experiments, robot kinematics were extracted from video by tracking fiducial markers on the robot, with two markers attached to each robot link. Jumps were filmed at 240 frames per second and a custom HSV filter was implemented in MATLAB to measure the pixel location of each marker in every video frame. The robot poses throughout each jump were first calculated directly from pixel measurements, assuming the robot was perfectly planar relative to camera throughout the jump, with no camera distortion. Then, the kinematics portion of the jumping robot factor graph (link poses, twists, and twist accelerations) was utilized to improve the accuracy of robot pose estimates by optimizing for fiducial marker positions subject to the kinematics constraints; to accomplish this, several additional variable and factor nodes were included.

Camera pose and camera calibration variable nodes were added to the graph to represent the position, orientation, and intrinsic properties of the camera. The pose of the camera in the jumping robot test setup was measured in the laboratory, while camera focal length and distortion parameters were estimated from a collection of checkerboard calibration images processed using OpenCV. Camera pose and intrinsic parameter priors were added as unary factors with low uncertainty. Fiducial marker location variables were added for each marker on each link, with a factor connecting each marker location to the pose of the respective robot link. Finally, a projection factor for fiducial marker location based on camera pose, camera calibration model, and pixel measurement was added for each marker on each link of the robot. This fiducial marker-based kinematics optimization compensated for robot translation and rotation out of the video plane, as well as camera misalignment and distortion.

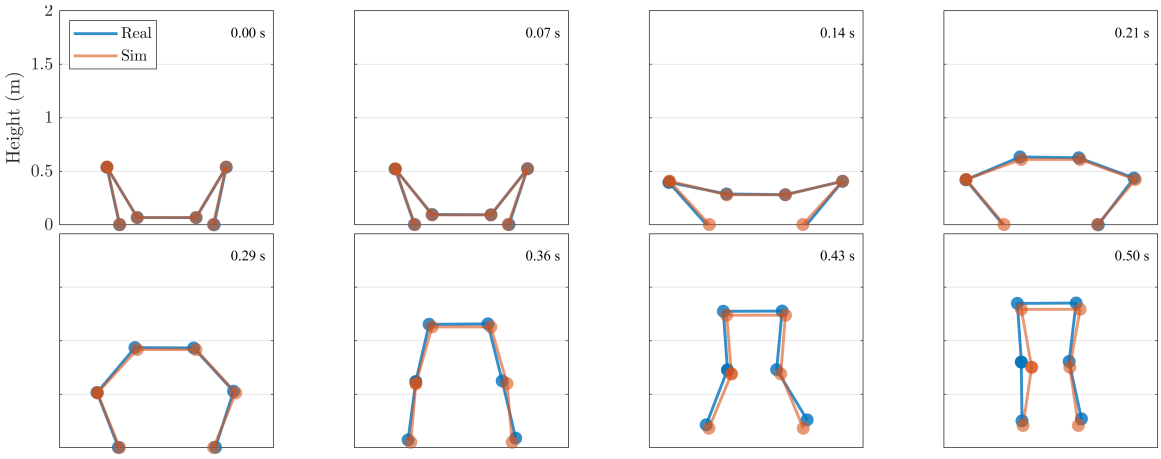

Figure 5.6: Comparison of robot poses in simulated and real jumps at multiple times throughout 0.2-m target jump (1.5-m torso height).

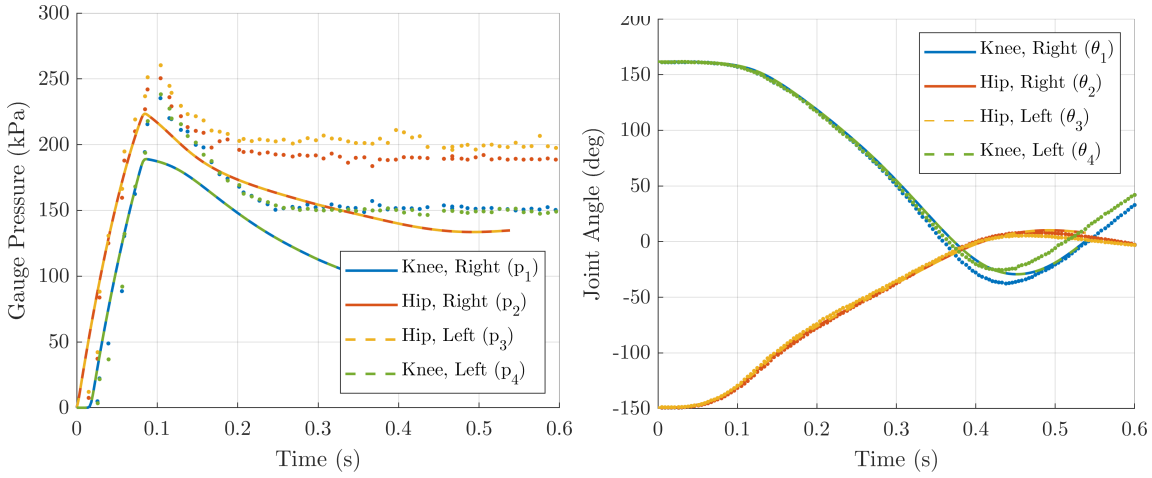

(a) **(b)**

Figure 5.7: Comparison of simulated and real jumps for 0.2-m target jump height: **(a)** Pneumatic muscle pressures, **(b)** robot joint angles. Circle markers represent experimental data and solid/dashed lines represent simulation data—note that simulated pressures and angles are symmetric on the right and left legs, so simulated data for knee joints and hip joints, respectively, overlap.

Vertical jumping. Valve control times were planned for four vertical jump height objectives, ranging from 0.1 to 0.4 m, where jump height was measured relative to the standing pose of the robot [79]. A goal constraint was added to the final robot state of the jumping robot factor graph to specify desired jump height; the twist of the torso link at the final state was constrained to be zero, corresponding to maximum jump height.

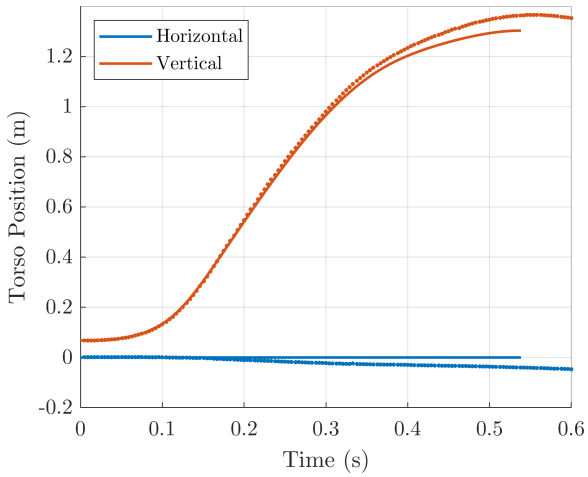

Figure 5.8: Comparison of robot torso trajectory in real and simulated jumps for 0.2-m target jump; circle markers represent experimental data and solid/dashed lines represent simulation data.

Before planning and evaluating jumping trajectories, several test jumps were used to tune several model parameters. Three key parameters—muscle connection stiffness, pneumatic tubing diameter, and joint damping—were adjusted to improve model agreement with experimental results; all other parameters were maintained at their nominal values. Muscle connection stiffness was set to 80 kN/m to account for the compliance of the materials connecting each muscle to the robot frame and joint pulley, as well as the compliance of the robot joint and frame components. Tubing diameter was decreased by 15 percent from the nominal 3/16-in diameter to compensate for unmodeled pneumatic restrictions. Finally, joint damping of approximately 0.03 N-m-s/rad was estimated.

To initialize values for the trajectory optimization, a jumping trajectory was simulated with arbitrary valve control times. Optimization over the factor graph was then performed using the GTSAM library, and the optimized valve control times were subsequently evaluated in experimental jumps with the real robot. Three jumps were performed for each of the four target heights.

The error between simulated and experimental trajectories for all jumps is summarized in Tables 5.2 and 5.3. Simulated trajectories generally underpredicted experimentally-

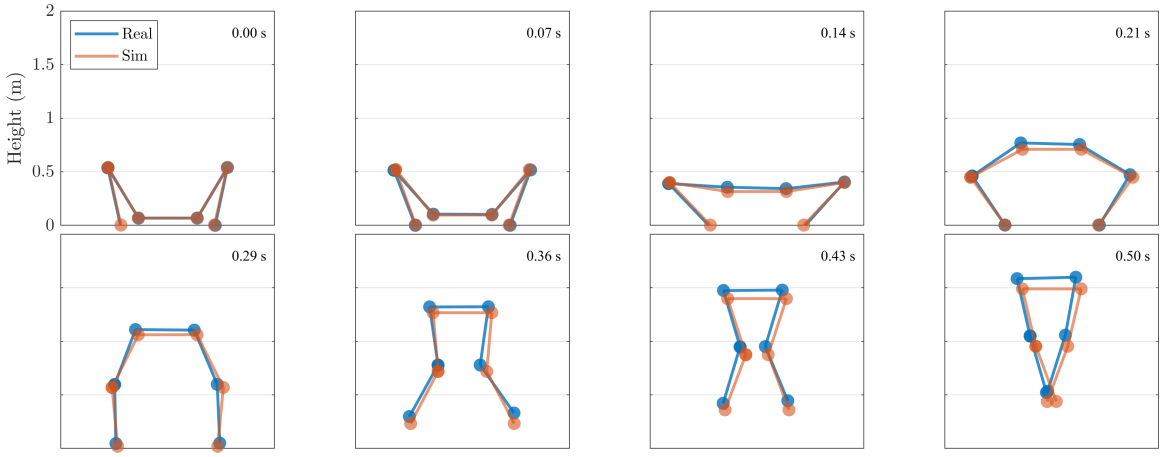

Figure 5.9: Comparison of robot poses in simulated and real jumps at multiple times throughout 0.4-m target jump (1.5-m torso height).

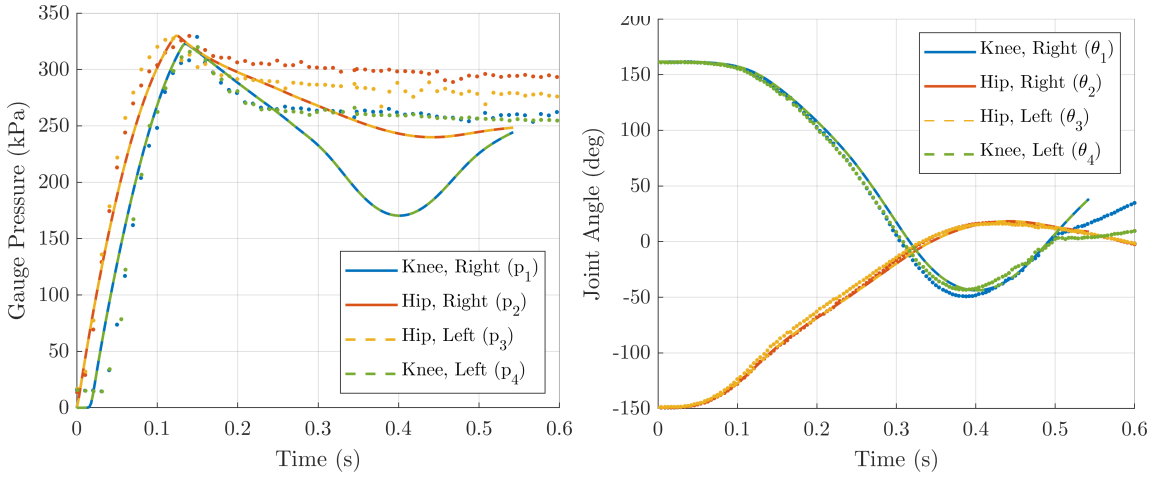

(a) **(b)**

Figure 5.10: Comparison of simulated and real jumps for 0.4-m target jump height: **(a)** Pneumatic muscle pressures, **(b)** robot joint angles. Circle markers represent experimental data and solid/dashed lines represent simulation data—note that simulated pressures and angles are symmetric on the right and left legs, so simulated data for knee joints and hip joints, respectively, overlap.

measured jump heights, most significantly for larger target jump heights. The maximum jump height error was 15.6 cm, for the 0.4-m target jump height. The average muscle pressure RMS error across all jumps was 46.5 kPa, while the average joint angle RMS error was 5.6 deg. Figures 5.9 and 5.10b show agreement between simulated and experimental joint angles for the largest target jump height of 0.4 m. Simulated muscle pressure inflation rates matched experimental data well, but peak pressures

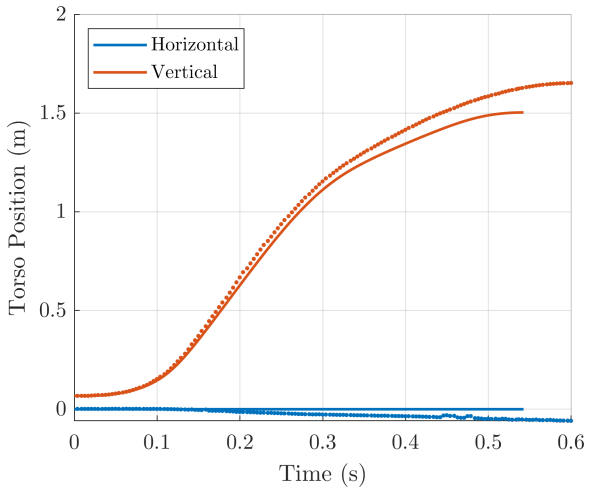

Figure 5.11: Comparison of robot torso trajectory in real and simulated jumps for 0.4-m target jump; circle markers represent experimental data and solid/dashed lines represent simulation data.

in simulation were lower than experimental pressures in many cases, especially for smaller jump heights. For example, in 0.2-m target jump height testing, peak muscle pressures were 25 to 50 kPa higher in experiments, as shown in Figure 5.10a.

For all tests, experimental muscle pressures remained nearly constant after valve closure (as expected), while simulated muscle pressures decreased significantly. This is because the muscle volume versus contraction polynomial fit, Equation 4.15, is only accurate up to the maximum contraction of the muscle. Simulated muscle contraction beyond this range results in a fictitious increase in muscle volume but does not impact the simulated trajectory accuracy, as the muscle model does not generate force beyond the muscle's maximum contraction. However, this muscle volume model simplification results in larger average errors between simulated and real muscle pressures, shown in Table 5.2.

5.3 Discussion

Much of the difference between simulation and experimental results can be attributed to uncertainty in several key model parameters which were manually tuned based on

Table 5.2: Average RMS error between simulated and experimental joint data over three trials for each target jump height.

Target Jump Height (m)	Muscle Pressure RMS Error (kPa)			
	Knee, Right	Hip, Right	Hip, Left	Knee, Left
0.1	55.5	42.4	50.7	51.2
0.2	54.6	41.3	48.9	45.7
0.3	44.3	44.8	53.2	47.1
0.4	52.5	35.7	30.7	45.8
Target Jump Height (m)	Joint Angle RMS Error (deg)			
	Knee, Right	Hip, Right	Hip, Left	Knee, Left
0.1	7.2	4.0	3.6	5.0
0.2	7.2	5.4	4.0	5.8
0.3	6.6	5.5	3.8	4.8
0.4	8.2	3.4	4.3	11.2

Table 5.3: Average error between simulated and experimental trajectories over three trials for each target jump height.

Target Jump Height (m)	Torso Location RMSE (cm)	Jump Height Error (cm)
0.1	4.4	7.6
0.2	4.7	4.7
0.3	5.6	10.3
0.4	6.2	15.3

limited test data. During tuning of the series stiffness parameter (assumed to be the same for both hip and knee joints), it was found that jumping dynamics are quite sensitive to the stiffness value. The stiffness at each joint encompasses the compliance of several mechanical elements, including the webbing and muscle mesh materials that connect the ends of the muscle to the joint pulley and robot link, the mesh attachment feature on the link, the 3D-printed pulley and joint components, and the carbon fiber robot frame. The impact of series stiffness on robot dynamics is further explored in Chapter 6.

Pneumatic system model accuracy is also critical, as pneumatic muscle force is a function of pressure. Although the simulated rate of muscle inflation during verti-

cal jumps matched experimental data well, the pneumatic system dynamics are not independent of other robot parameters, such as series stiffness. This may be the reason simulated peak pressures were generally lower than experimental peak pressures. Thus, in future work, a more robust system identification approach should be used to identify critical system parameters simultaneously.

The existing trajectory factor graph for the robot can be adapted for system parameter identification by including kinematics and pressure data from experiments. Unary measurement factors can be connected to muscle and source tank pressure variables at each trajectory timestep for experimental pressure data. Kinematics information can be included by incorporating the additional graph structure utilized for kinematics extraction from video: camera pose, calibration, and marker location variables, and the correspond projection factors. With this setup, marker pixel location information from video footage can be directly added to the system identification factor graph.

System identification could be extended to incorporate dynamic measurements for a more comprehensive analysis. Ideally, a load cell would be connected in series with each pneumatic muscle on the robot to measure muscle contraction force; however, it may be challenging to incorporate the load cell without extending robot link lengths. A simpler approach is to use force measurement plates at both robot feet to measure ground reaction forces, although this would not capture joint-level information. Force measurement data could then be included in the system identification trajectory graph.

As detailed in the previous chapter, several pneumatic modeling assumptions were used to simplify analysis. Rather than attempting to model all system components and include all physical phenomena, valve-to-muscle tubing diameter was instead treated as a tunable parameter to compensate for unmodeled effects. Simulated muscle inflation rates during vertical jumps were generally consistent with experimental

data, and peak simulated pressures agreed with peak experimental pressures more closely after performing system identification. Nevertheless, it would be beneficial to investigate modeling of additional pneumatic features in future work.

The factor graph approach to trajectory optimization in this chapter provides an intuitive representation of robot states and dynamics as nodes and factors in a graph. Sub-factor graphs are individually constructed for subsets of the robot dynamics—the robot frame kinodynamics and the pneumatic muscle-driven joint dynamics—and connected together to represent the complete robot dynamics. Replicates of the dynamics graph are then connected via collocation constraints to construct a robot trajectory in time, where each graph represents a discretized collocation point.

A notable benefit of the factor graph framework is that the robot factor graph can be utilized for multiple aspects of the research problem. In this work, the entire graph is used to plan jumping trajectories. The robot kinematics portion of the graph is used to improve estimates of experimental robot kinematics extracted from video, with the addition of camera pose/calibration variables and camera-marker projection factors. As described above, source tank and muscle pressure measurements can be incorporated into the overall trajectory graph to perform system identification of key robot parameters from experimental jump data.

In future work, this trajectory planning strategy could be extended to lateral jumping, with additional trajectory phases for single foot-ground contact dynamics. Additionally, more sophisticated optimization objectives that incorporate foot clearance for jumping over obstacles or robot orientation for landing on sloped surfaces and uneven terrain may be explored. An important step will be to incorporate planning for safe robot landing as part of the trajectory optimization. Here, the passive mechanical compliance of pneumatic muscles can be leveraged to compensate for trajectory error and uncertainty in the environment.

5.4 Significance

In this chapter, a factor graph-based trajectory planning approach is formulated for pneumatic muscle-driven robots controlled using burst inflation. A trajectory factor graph is constructed by connecting consecutive robot factor graphs in time via collocation constraints, where each robot graph incorporates the pneumatic system, muscle, and rigid body dynamics models formulated in Chapter 4. After goal constraints representing the trajectory objective function are added to the trajectory graph, optimization of the graph yields valve open and close times corresponding to the target robot trajectory. Additionally, trajectory optimization is extended to hybrid robot dynamics using a multi-phase approach, in which each phase represents a distinct set of dynamics. This burst-inflation trajectory planning approach enables reduced pneumatic control system mass, cost, and complexity.

The trajectory planning approach developed in this work was evaluated on a planar two-legged jumping robot, where valve control times were planned for various vertical jump heights. In the context of trajectory planning for pneumatic muscle-driven legged robots, there is only one other study found that performs jump trajectory optimization [69]. The authors use proportional valves for continuous pressure modulation of pneumatic muscles on a quadruped and achieve an average joint angle RMS error of 2.3 deg across all joints and a max RMS error of 3.4 deg across all joints for one experimental jump. The target jump height and distance are 36 cm and 73 cm, respectively, but the actual height and distance are not provided. For comparison, the average RMS error across all joints in all twelve vertical jumps in this Chapter was 5.6 deg, with a max RMS error of 14.7 deg. Thus, with regard to joint tracking accuracy, the burst inflation approach used in this work is not significantly far off from continuous pressure control. Pneumatic muscle-driven systems controlled via proportional valves are expected to exhibit more precise joint trajectory tracking, as

proportional valves enable continuous feedback pressure control that can compensate for disturbances and model inaccuracies. In contrast, continuous pressure modulation is not possible with burst-inflation via discrete valves, so higher RMS joint error compared to [69] was anticipated for the jumping robot in this work.

In comparison, trajectory planning approaches for motor- and hydraulic-driven legged robots have demonstrated relatively high jump planning accuracy. The quasi direct-drive MIT Cheetah 3 robot executed planned robot jumps onto a 30-inch desk, but the authors did not quantify trajectory error [80]. The SEA-driven StarlETH quadruped robot performed a 30-cm jump relative to its initial squat pose, with around 5 percent jump height error between planned and executed trajectories [81]. A single leg hopper with direct-drive motors demonstrated planned jump height error closer to 10 percent for a 25-cm jump relative to initial squat pose [82]. The hydraulically-actuated HyQ quadruped robot performed a 20-cm jump with around 5 percent error between planned and executed trajectories [83].

While the average jump height error for all jumps performed on the pneumatic muscle-driven jumping robot in this work was around 40 percent, the sensitivity of muscle dynamics and overall jump height to robot joint stiffness—further explored in Chapter 6—suggests that a more robust system identification of a few key system parameters, including series stiffness, can significantly improve planning accuracy. Additionally, note that with the exception of the MIT Cheetah 3 study that did not quantify jumping trajectory error, the jump heights for all other motor and hydraulically-driven robot studies were limited to 30 cm and were measured relative to squatting robot pose, not standing pose; in this work, jumps were performed up to 40 cm relative to the robot's 1.1-m standing pose.

The trajectory planning strategy developed in this work can be applied to any pneumatic muscle-driven robot morphology, enabling execution of agile robot maneuvers while facilitating passive mechanical compliance. Furthermore, the factor

graph-based planner can readily accommodate additional engineering analyses such as kinematics extraction from video, as well as system parameter identification which is central to maximizing trajectory planning accuracy.

CHAPTER 6
DESIGN OPTIMIZATION INSIGHTS & FUTURE DIRECTIONS

In this chapter, a design optimization approach to maximize pneumatic muscle-driven robot dynamic performance using biologically-inspired joint mechanisms is laid out, addressing the final objective of this work. Specifically, the muscle-driven robot model developed in Chapter 4 is used to gain insight into the impacts of series elasticity and joint angle-dependent mechanical advantage on robot performance and how they may compensate for the force-length limitations of pneumatic muscles.

Nature demonstrates that animal morphology can compensate or even leverage biological muscle's force-length and force-velocity limitations, shown in Figure 6.1, to maximize animal agility. For human jumping, several models and experimental studies of the triceps surae muscle-tendon complex suggest that tendon compliance and increasing moment arm versus joint angle allow for high joint angular velocities with large joint moments that would not be possible otherwise, given the corresponding muscle properties [84], [85]. Similar studies have suggested that shorter plantarflexor moment arms are associated with improved dynamic performance in tasks like sprinting, as a smaller muscle shortening velocity is required for a shorter moment arm, resulting in larger muscle forces [86], [87]. In general, the human body uses tendons of various lengths and stiffnesses connecting to joint angle-dependent moment arms to change the shape of each muscle's torque-angle curve. In fact, for muscle-tendon units of the lower body, peak isometric moment generally does not occur at the same angle where peak muscle force is produced, nor at the angle of maximum moment arm [88].

Smaller animals similarly use tendons and variable moment arms to improve dynamic performance. For example, studies on different species of frogs estimate that

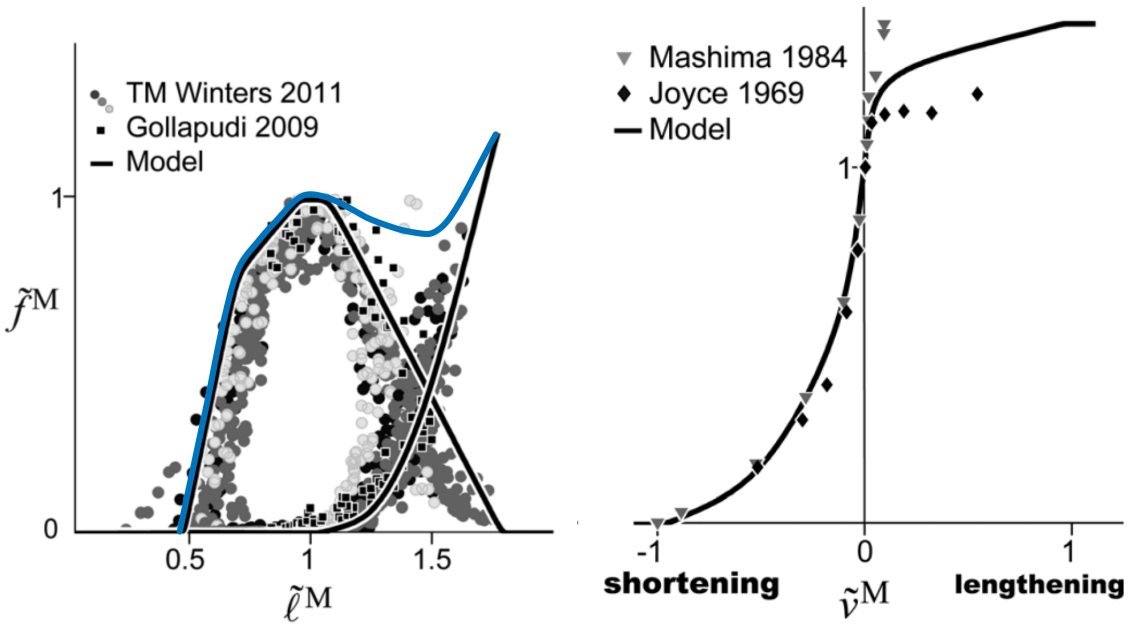

(a) **(b)**

Figure 6.1: **(a)** Active (left), passive (right), and total (blue) biological muscle force-length curves, where $\tilde{l}^M$ is the muscle length at which the muscle develops peak isometric active force $\tilde{f}^M$; **(b)** biological muscle force-velocity curve, where $\tilde{v}^M$ is the muscle lengthening velocity [89].

the power required to achieve observed jump distances is several times greater than the peak power available from jumping muscles. The authors suggest that this energy redistribution in time is achieved via series elasticity and joint angle-dependent mechanical advantage [90]–[92]. Specifically, a tendon stores energy from relatively slow muscle contractions and subsequently releases the energy over a shorter time period later in the jumping motion sequence. Tendon loading in this manner requires that a large muscle force is applied to the tendon before significant leg motion occur. This is enabled by a skeletal moment arm configuration that provides a smaller mechanical advantage at joint angles early in the jump sequence, producing less joint torque, and thus, less frog motion. This 'inertial catch mechanism' essentially decouples muscle displacement from leg displacement, allowing pre-loading of the tendon. An increase in mechanical advantage throughout joint rotation increases joint velocity, facilitating the release of tendon energy later in the jump.

Inspired by biology, this chapter investigates whether series elasticity and joint angle-dependent moment arm mechanisms can similarly improve the dynamic performance of pneumatic muscle-driven robots, as they do for biological muscle-driven animals. The pneumatic muscle (Figure 6.2) and biological muscle (Figure 6.1a) have similar (total) force-length curves, in that they both generally increase with muscle length. In contrast to biological muscle, pneumatic muscles are not force-limited by contraction velocity; however, pneumatic muscle contraction velocity is limited by pneumatic system configuration (source pressure and airflow restriction).

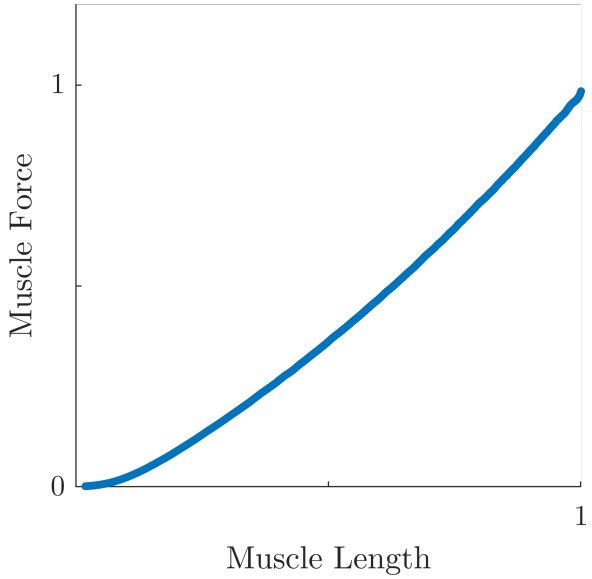

Figure 6.2: Pneumatic artificial muscle force-length curve.

Previous work has examined the effects of adding series elasticity and variable mechanical advantage to improve the performance of both traditional and muscle-driven robots. In the context of traditional motor-driven systems, one study developed a servo-driven mechanism to adjust the torque-angle curve of a hinge joint [93]. A spring was configured in series with a second servo driving the joint and the torque-angle curve mechanism was used to adjust stiffness for a one-legged hopping robot. However, the authors did not optimize spring stiffness nor torque-angle curve, but mentioned only that it is possible. In another study, the authors optimized the design

of a motor-driven four-bar linkage with an elastic link (link length, spring stiffness, and spring tension) to maximize vertical jump height for drop jumping of quadruped hind limbs [94].

With regard to pneumatic muscle-driven robots, one group sought to expand joint torque capacity over a larger workspace for a single joint manipulator actuated by an antagonistic muscle pair, though high-speed movement was not a focus this work [95]. Another group developed an adjustable torque-angle profile mechanism and explored effects of varying joint torque-angle curves for quadrupedal robot jumping [66]. The authors explored muscle pressurization timing optimization in simulation and evaluated jumping performance for only four torque-angle configurations—they did not perform an overall design optimization.

In this chapter, the impacts of series elasticity and variable moment arm on the performance of pneumatic-muscle driven robots is investigated for dynamic tasks. The use of variable moment arm to improve joint torque characteristics is first illustrated in a simple application: a pneumatic knee exoskeleton with a single muscle-actuated joint. The knee exoskeleton assistance torque output is optimized for walking on inclined terrain by tuning the geometry of a lever arm that converts linear muscle force to joint torque. A general design optimization approach is then outlined for a more complex system: the two-legged jumping robot with four muscle-actuated joints detailed in Chapter 5. A sequence of design optimizations are performed in simulation to examine the impacts of series elasticity and angle-dependent mechanical advantage on jumping performance. Results from this work yield valuable design insights for pneumatic-muscle driven robots and motivate future directions for this design optimization approach.

6.1 Knee Exoskeleton Case Study

The use of joint angle-dependent moment arm to improve the performance of pneumatic muscle-driven robots is demonstrated on a relatively simple system: a 1-DOF pneumatic knee exoskeleton. The knee exoskeleton system was developed in collaboration with the EPIC Lab at Georgia Tech to provide assistance during level-ground and inclined walking with the goal of reducing the wearer's metabolic cost. Four pneumatic muscles are attached to each leg of the exoskeleton, with two parallel pairs of muscles connected in series, as shown in Figure 6.3. The exoskeleton is controlled via proportional myoelectric control (PMC), providing assistive knee extension torque at the knee joint in proportion to the muscle activation level of the quadriceps muscle group in the thigh. Discrete solenoid valves are used to inflate, seal, and vent the pneumatic muscles; the valves and control hardware are contained in a backpack worn by the exoskeleton user. The targeted exoskeleton assistance level was 20 percent of

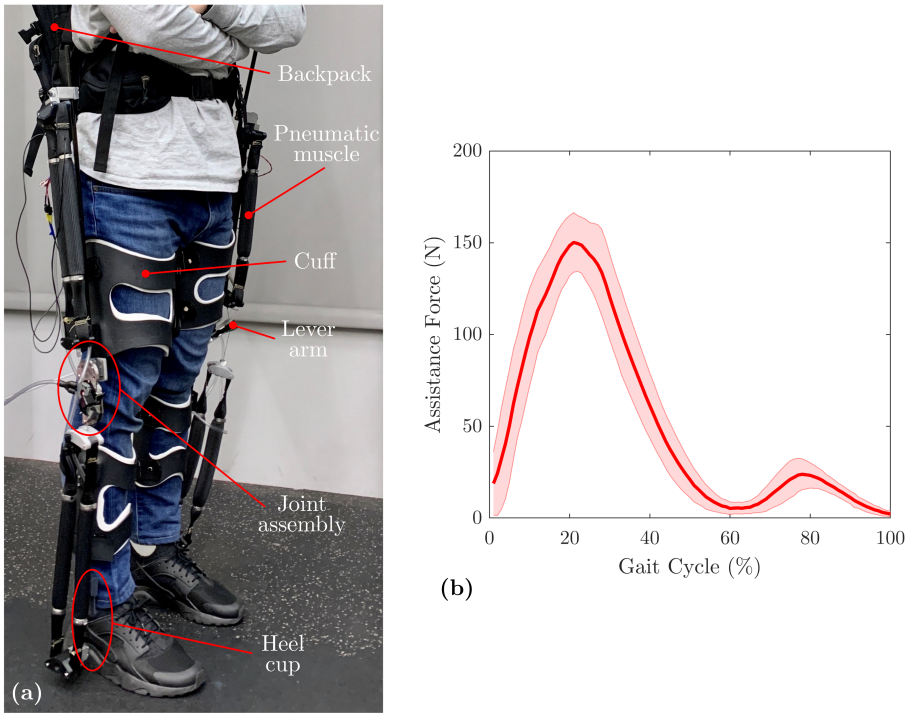

Figure 6.3: **(a)** Bilateral pneumatic knee exoskeleton; **(b)** exoskeleton knee assistance force profile.

biological knee extension torque for a user walking up an inclined surface, approximately 15-20 Nm assistance torque. The corresponding targeted range of motion for knee assistance was 20-0 deg knee flexion [96]–[99]. An additional requirement of the exoskeleton was to allow for 90 deg of knee flexion so that the user can sit or squat while wearing the device; thus, the unpressurized muscles (zero contraction) must attach to the exoskeleton frame at 90 deg knee flexion.

The pneumatic muscle produces maximum force at its full length, and force output decreases nonlinearly as the muscle contracts, as shown in Figure 4.7. Consequently, the maximum exoskeleton force for the 90 to zero deg range of motion is produced at 90 deg and decreases throughout knee extension. With a constant moment arm throughout knee joint rotation, the maximum exoskeleton assistance torque will also be produced at 90 deg. However, the torque-angle curve can be shaped using a joint angle-dependent moment arm to shift peak assistance torque to a different angle. Accordingly, a lever arm was designed for the exoskeleton to shape the torque-angle curve for the targeted assistance range—the lever arm length and mounting angle on the exoskeleton frame were optimized to maximize torque from 20 to zero deg knee extension.

Knee assistance torque versus knee angle was calculated for a range of lever arm mounting angles. As shown in Figure 6.4a, with the muscles connected to a pulley (constant moment arm), the assistance torque curve from 90 to zero deg knee flexion follows the profile of the muscle force versus contraction length curve. By replacing the pulley with a lever arm, the torque-angle curve changes shape and the peak torque can be shifted towards smaller knee angles by adjusting lever mounting angle. Assistance torque is maximized in the 20-0 deg knee flexion range for a mounting angle of zero deg, relative to the horizontal (ground) plane. This intuitively makes sense, as a zero-deg mounting angle produces largest lever arm at zero-deg knee flexion, when muscle force is lowest (largest muscle contraction).

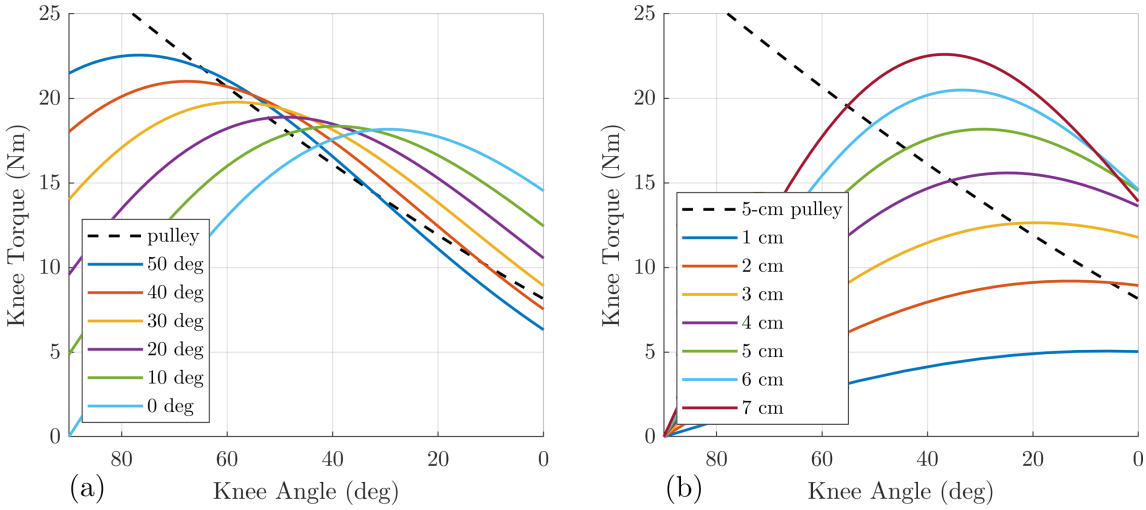

Figure 6.4: Assistance torque versus knee flexion angle comparing 5-cm pulley and lever arm configurations: **(a)** 5-cm lever arm at various mounting angles; **(b)** various lever arm lengths at 0-deg mounting angle.

Knee assistance torque versus knee flexion angle was then calculated for a range of lever arm lengths. As shown in Figure 6.4b, peak assistance torque increases as lever arm length increases; however, peak torque also shifts back in the direction of larger knee flexion angles (away from the target range) for increasing lever arm length. A high average assistance torque is achieved in the 20 to zero deg knee flexion range for a lever arm length of 4 to 5 cm. Therefore, a 5-cm lever arm with zero deg mounting angle was selected for the final exoskeleton design. In the remainder of this chapter, the use of angle-dependent mechanical advantage to optimize robot performance, demonstrated by this knee exoskeleton design example, is investigated for the more complex jumping robot system.

6.2 Methodology

The impacts of both joint angle-dependent mechanical advantage and series elasticity on pneumatic muscle-driven jumping robot performance are explored. In the jumping robot model, the fixed-radius pulley at each joint is replaced by a variable radius cam. A series elastic element was already implemented at each joint in the model in Chapter

5 (Subsection 5.1.4) to model joint-level compliance inherent to the robot hardware. To perform design studies, a particle swarm optimization is set up with cam geometry and series stiffness parameters as decision variables; 5000 jumping robot particles are simulated per iteration, with 50 total optimization iterations. Over a number of design studies, the effects cam and stiffness parameters on vertical jump height and joint-level dynamics are detailed.

6.2.1 Variable moment arm

An angle-dependent moment arm is implemented at each joint using a cam. In this work, the cam is limited to a linear profile

$$r(\phi) = r_0 + m\phi \tag{6.1}$$

with initial cam radius r_0 and profile slope m as the two cam design parameters. The cam profile is parameterized by the angle ϕ, such that at $\phi = 0$, the cam radius is r_0. There are two cam geometry-dependent values at each joint angle that influence overall robot dynamics: the effective moment arm and the linear muscle displacement due to cam rotation.

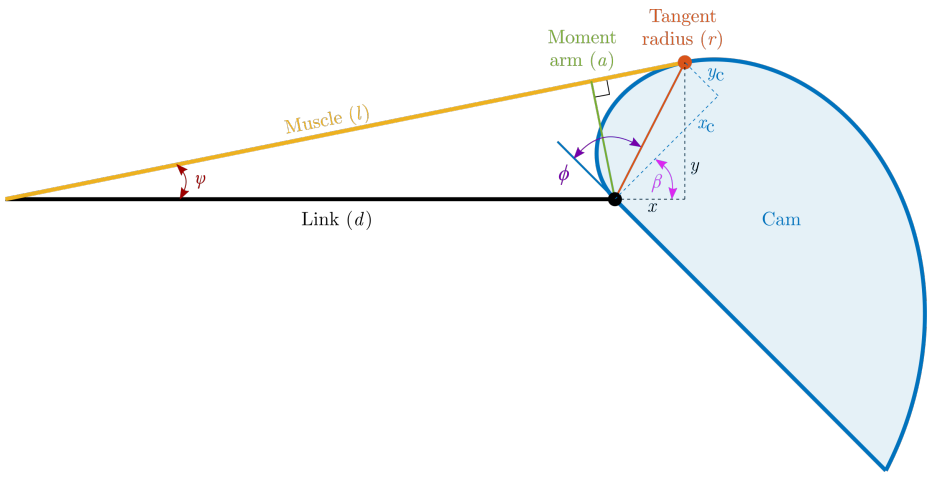

Figure 6.5: Muscle-cam geometry parameters.

Effective moment arm. The effective moment arm of the cam—through which the pneumatic muscle produces joint torque—is calculated by equating the slope of the muscle with the slope of the cam at the muscle-cam tangent point. First, the tangent point, shown in Figure 6.5, is expressed in cam coordinates

$$\begin{aligned} x_c &= r(\phi)\sin(\phi) = (r_0 + m\phi)\sin(\phi) \\ y_c &= r(\phi)\cos(\phi) = (r_0 + m\phi)\cos(\phi). \end{aligned} \tag{6.2}$$

The tangent point is then converted to link coordinates via the relative angle, β, between the cam and the link

$$\begin{aligned} x &= x_c\cos(-\beta) + y_c\sin(-\beta) \\ &= (r_0 + m\phi)\sin(\phi)\cos(\beta) - (r_0 + m\phi)\cos(\phi)\sin(\beta) \\ &= -(r_0 + m\phi)\sin(\beta - \phi) \\ y &= -x_c\sin(-\beta) + y_c\cos(-\beta) \\ &= (r_0 + m\phi)\sin(\phi)\sin(\beta) + (r_0 + m\phi)\cos(\phi)\cos(\beta) \\ &= (r_0 + m\phi)\cos(\beta - \phi). \end{aligned} \tag{6.3}$$

The muscle and cam slopes, s_m and s_c, are then calculated as

$$\begin{aligned} \frac{dx}{d\phi} &= (r_0 + m\phi)\cos(\beta - \phi) - m\sin(\beta - \phi) \\ \frac{dy}{d\phi} &= (r_0 + m\phi)\sin(\beta - \phi) + m\cos(\beta - \phi) \end{aligned} \tag{6.4}$$

$$\begin{aligned} s_m &= \frac{y}{x + d} = -\frac{(r_0 + m\phi)\cos(\beta - \phi)}{(r_0 + m\phi)\sin(\beta - \phi) - d} \\ s_c &= \frac{dy/d\phi}{dx/d\phi} = \frac{(r_0 + m\phi)\sin(\beta - \phi) + m\cos(\beta - \phi)}{(r_0 + m\phi)\cos(\beta - \phi) - m\sin(\beta - \phi)} \end{aligned} \tag{6.5}$$

where d is the robot link length. The cam slope equation can be further simplified

by defining $\theta = \arctan(\frac{m}{r_0+m\phi})$:

$$\begin{aligned} s_c =& \frac{\cos(\theta)\sin(\beta-\phi)+\sin(\theta)\cos(\beta-\phi)}{\cos(\theta)\cos(\beta-\phi)-\sin(\theta)\sin(\beta-\phi)} \\ =& \tan(\theta+\beta-\phi) \\ =& \tan(\psi). \end{aligned} \tag{6.6}$$

After equating the muscle and cam slopes at the tangent point and numerically solving for the cam parameterization angle ϕ, the moment arm a can be computed as

$$\psi = tan^{-1}(s) \tag{6.7}$$

$$a = d\sin(\psi). \tag{6.8}$$

If the angle ϕ solution is outside of the cam parameterization range (meaning that the cam geometry does not exist in that angle range), ϕ is set to the parameterization angle limit

$$\phi < \phi_{min} \rightarrow \phi = \phi_{min}$$

$$\phi > \phi_{max} \rightarrow \phi = \phi_{max}$$

and the slope is then computed from Equation 6.5. These two cases are illustrated in Figure 6.6.

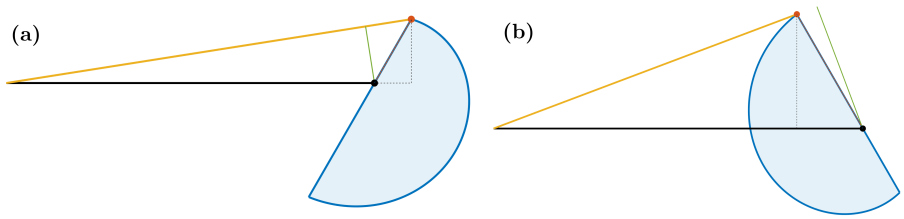

Figure 6.6: (a) Cam moment arm solution for ϕ less than ϕ_{min}; (b) cam moment arm solution for ϕ greater than ϕ_{max}.

Muscle displacement. The linear muscle displacement due to cam rotation dictates how much the corresponding muscle must contract before muscle slack is removed and the muscle begins to apply force to the cam. In order to calculate the linear muscle displacement, the muscle length up to the muscle-cam tangent point and the length of the muscle lead that wraps along the profile of the cam are calculated. The latter is calculated as the length along the cam from the start of the cam profile up to the angle ϕ (corresponding to the muscle-cam tangent point)

$$\begin{aligned} l_{cam} =& \int_0^{\phi} \sqrt{(r_0 + m\phi)^2 + m^2} d\phi \\ =& \frac{m \log(r_0 + \sqrt{(r_0 + m\phi)^2 + m^2} + m\phi)}{2} + \frac{(r_0 + m\phi)\sqrt{(r_0 + m\phi)^2 + m^2}}{2m}. \end{aligned} \tag{6.9}$$

The muscle length up to the muscle-cam tangent point is calculated as

$$\begin{aligned} l_{muscle} =& \sqrt{y^2 + (x + d)^2} \\ =& \sqrt{(r_0 + m\phi)^2 + d^2 - 2d(r_0 + m\phi) sin(\beta - \phi)}. \end{aligned} \tag{6.10}$$

Then, the linear muscle displacement Δc can be computed as the difference between muscle length change and cam wrap length change for two subsequent joint angles

$$\Delta c = \Delta l_{muscle} - \Delta l_{cam}. \tag{6.11}$$

6.2.2 Series elasticity

The series elastic 'tendon' element connected between the pneumatic muscle and the cam at each joint is modeled as a linear spring

$$f_s = k\Delta a \tag{6.12}$$

where k is the spring stiffness and Δa is the spring displacement. A linear spring element was already added in the previous chapter, Figure 5.4, to account for existing muscle connection and robot frame compliance; thus, for the sake of design optimization, the spring stiffness was made a design decision variable.

6.3 Experiments and Results

The effects of series elasticity and joint angle-dependent mechanical advantage on vertical jump height were investigated for the planar two-legged jumping robot model over a number of design optimizations. Optimizations were performed for a squat jump from a static pose with the robot torso approximately 7 cm off the ground. The 1.5-liter source tank pressure was set to 550 kPa. All pneumatic muscles were initially activated (valve opened) at time zero and sealed at 150 ms, unless otherwise noted.

6.3.1 Series elasticity

To investigate the impact of series elasticity on robot jumping performance, jump height was optimized with respect to tendon stiffness. Fixed-radius 4.5-cm pulleys were modeled at all four joints. The tendon stiffnesses at the hip and knee joints were independent and allowable stiffness values ranged from 10 N/cm to 10,000 N/cm. The maximum jump height was achieved for the highest stiffness values (minimum compliance) at both the hip and the knee (Figure 6.7). Jump heights with 10,000 N/cm tendons were nearly 2.4x greater than with 100 N/cm tendons; with 10 N/cm tendons, the robot did not leave the ground.

As shown in Figure 6.8, a compliant tendon unfavorably allows the pneumatic muscle to contract more throughout the beginning of the jump than with a high-stiffness tendon. This results in larger muscle volume during the early stage of the jump, since muscle volume increases with contraction (Equation 4.15). Consequently, with

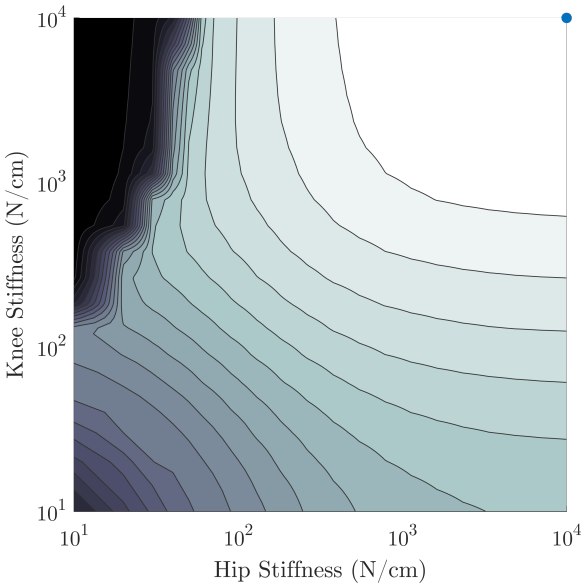

Figure 6.7: Jump height contour plot for varied hip and knee tendon stiffnesses: increasing jump height from dark to light; blue marker indicates maximum jump height.

a larger muscle volume to pressurize, the time to peak muscle pressure is significantly later in the jump, by which point the muscle has already contracted through most of its range. As a result, the muscle is operating lower on its force-length curve (Figure 6.2) when it reaches max pressure, so peak muscle force is significantly lower. Consequently, robot center-of-mass power, Figure 6.9, is significantly lower with compliant tendons and foot liftoff occurs much later in the jump sequence—liftoff is delayed nearly 100 ms.

Next, muscle activation timing was varied with tendon stiffness to determine whether activation timing impacts optimal stiffness values. The offset between knee and hip inflation times was varied from -100 ms (hip muscles activate before knees) to 100 ms (knees before hips). A 150-ms total inflation time was maintained for each muscle (ex: for an activation time of 10 ms, the valve closes at 160 ms).

The highest jump was again achieved with maximum tendon stiffnesses. The optimal activation sequence comprised knee inflation only 5 ms before hip inflation. Interestingly, this is the opposite of human leg muscle activations observed during squat jumps, which show a proximal-distal activation sequence [100], [101]. Plotting

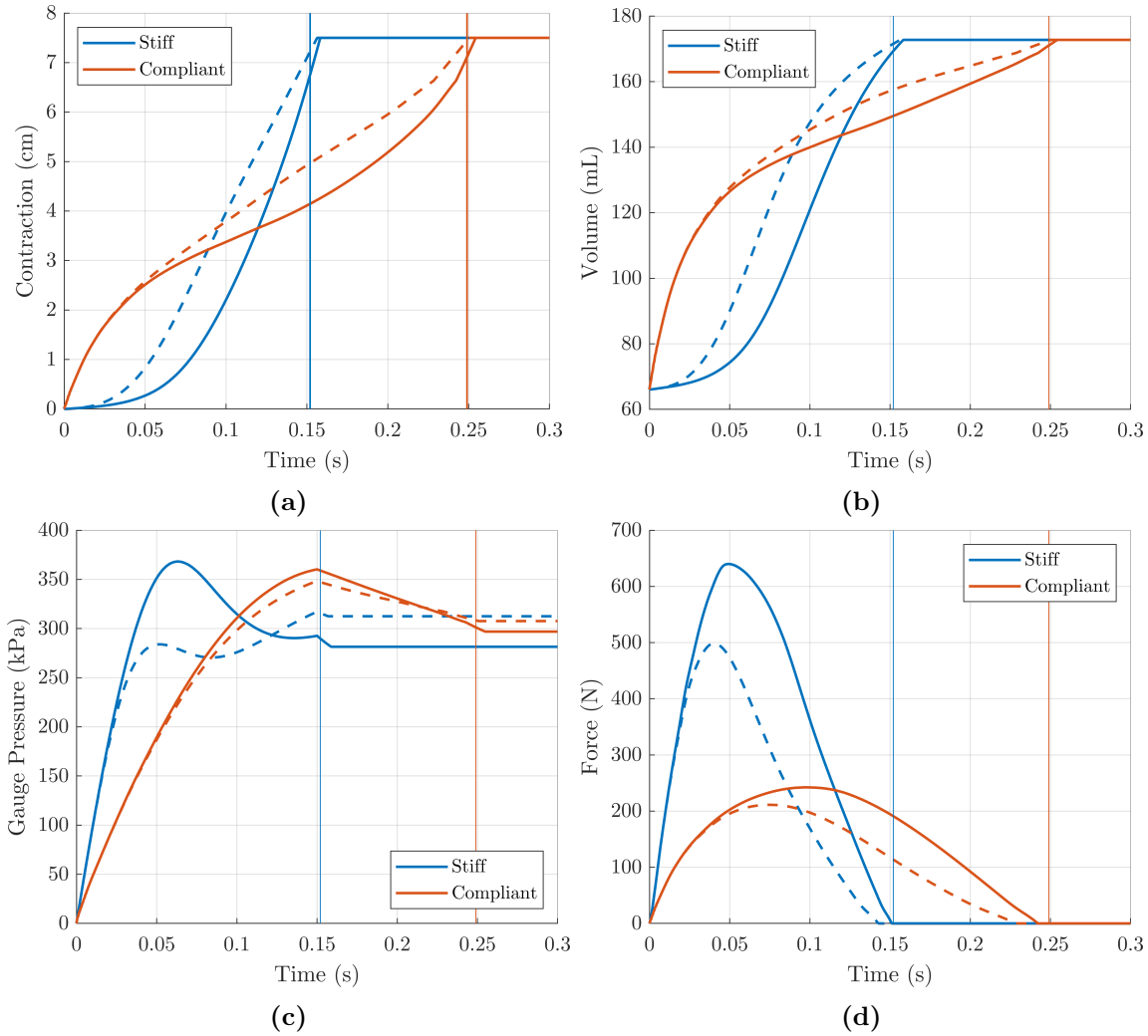

Figure 6.8: Comparison of robot joint dynamics for jump with stiff joint tendons versus jump with compliant tendons: **(a)** knee muscle contraction, **(b)** knee muscle volume, **(c)** knee muscle pressure, **(d)** knee muscle force. Solid lines represent knee joint and dashed lines represent hip joint; vertical lines represent foot liftoff times

jump height versus pneumatic muscle activation timing for maximum stiffness tendons, Figure 6.10, shows that there is a window of hip offset timing corresponding to the highest jumps. From -5 ms to 15 ms hip offset, there is a less than 2 percent change in jump height; outside this window, there is a significant drop-off in jump height.

Closer examination of muscle and joint dynamics reveals why the short hip offset timing window around time zero results in the highest jumps. Figure 6.11 compares

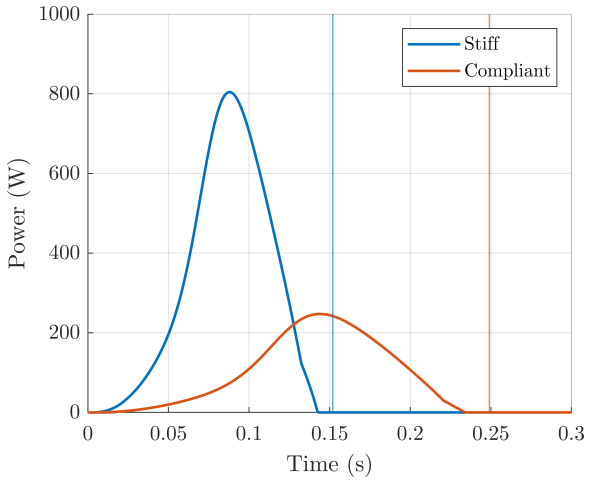

Figure 6.9: Comparison of robot center-of-mass power for jump with stiff joint tendons versus jump with compliant tendons. Vertical lines represent foot liftoff times.

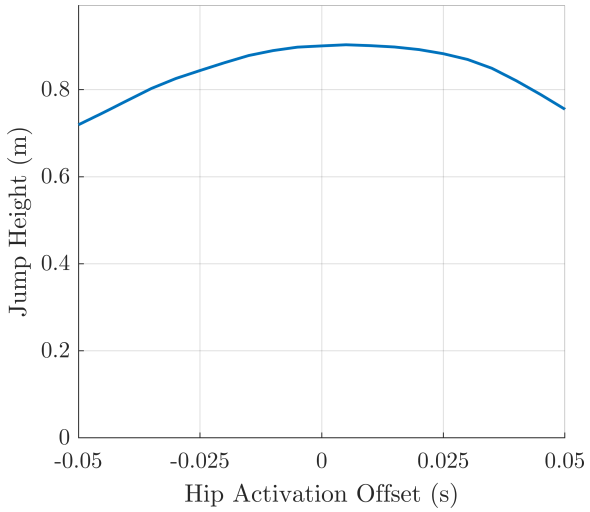

Figure 6.10: Jump height versus hip muscle activation offset time for 10 kN/cm tendon stiffness.

muscle and joint data for hip activation 50 ms before knee activation with stiff tendons to simultaneous hip and knee activation at time zero. For simultaneous activation, the hip and knee muscles reach peak pressures at close to the same time early in the jump, with peak hip pressure just before peak knee pressure; consequently, peak hip and knee forces have a similar timing relationship and are somewhat similar in magnitude (difference of less than 150 N).

However, with a 50-ms delay in knee muscle activation, the gap between peak

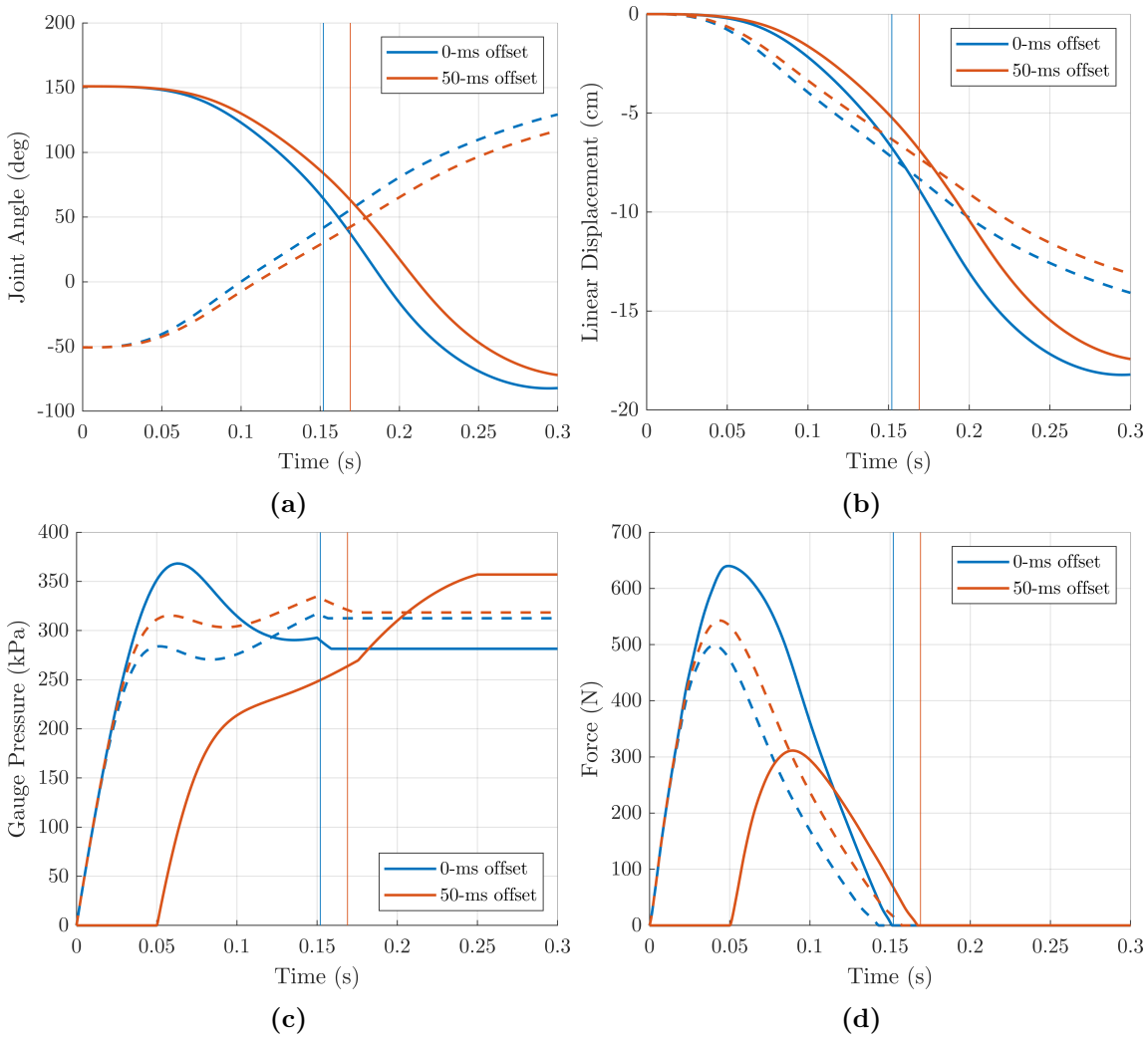

Figure 6.11: Comparison of robot joint dynamics for jump with hip activation 50 ms before knee activation versus jump with simultaneous hip and knee activation at time zero, both with stiff tendons: **(a)** joint angle, **(b)** linear displacement, **(c)** muscle pressure, **(d)** muscle force. Solid lines represent knee joint and dashed lines represent hip joint; vertical lines represent foot liftoff times.

hip and knee forces is larger, and peak knee force is significantly lower. This is due to movement of the robot early in the jump before the knee muscles are engaged. Figure 6.11b shows the linear displacement in direction of muscle contraction due to joint angle rotation (6.11a)—by the time the knee muscle reaches a substantial force-generating pressure of 200 kPa at around 100 ms, the knee joint has already displaced nearly 2 cm. Thus, the knee muscles are operating lower on the muscle force-length curve by the time they are activated, so that they have a significantly lower maximum

force limit. In the case of hip activation 50 ms after knee activation, Figure 6.12, the same is true for the hip muscles, although the effect is less pronounced. Overall, the reduction in muscle force for the activation-delayed muscles, coupled with the timing offset between peak hip and knee forces, reduces jump power, as shown in Figure 6.13.

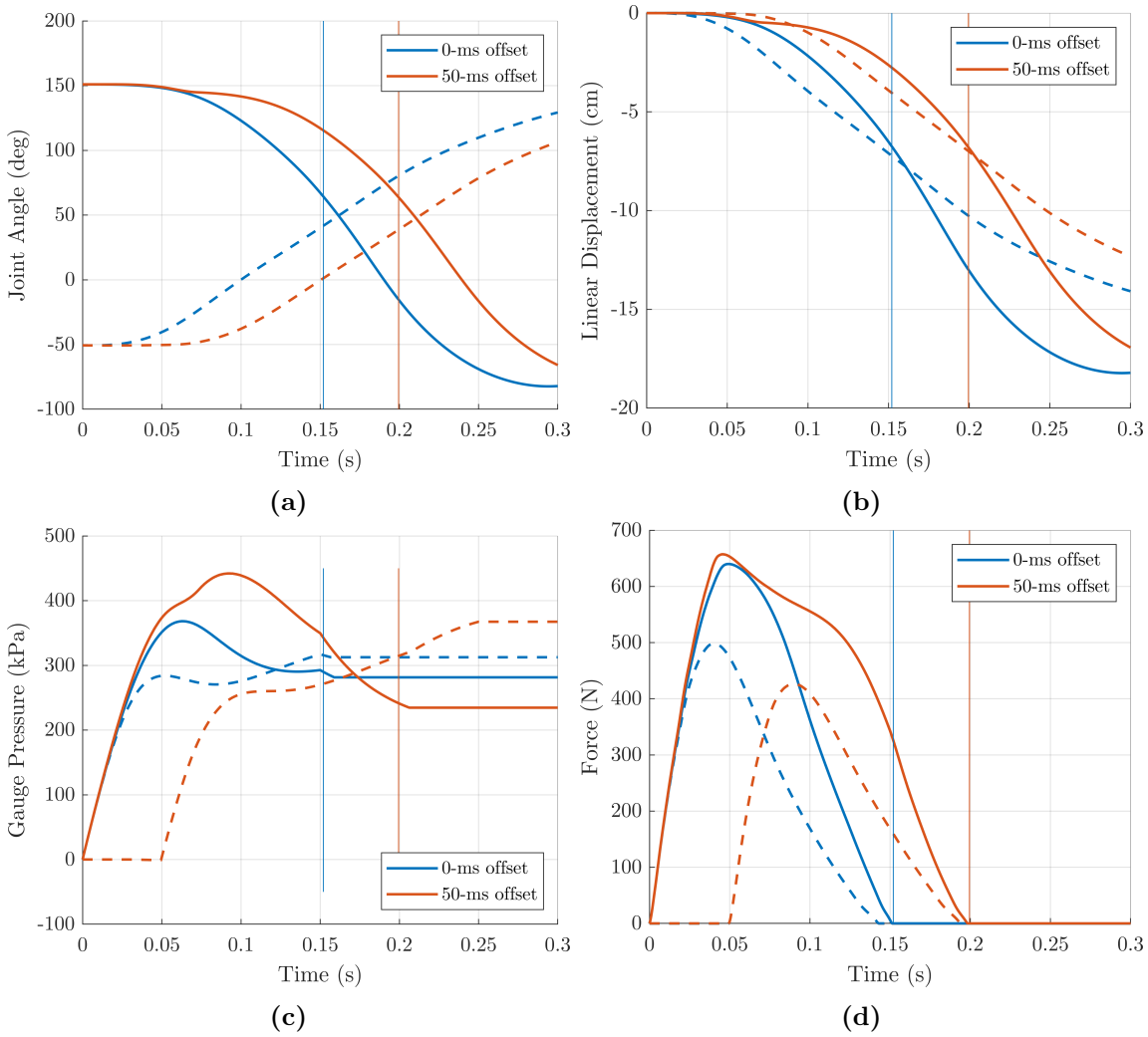

Figure 6.12: Comparison of robot joint dynamics for jump with knee activation 50 ms before hip activation versus jump with simultaneous hip and knee activation at time zero, both with stiff tendons: **(a)** joint angle, **(b)** linear displacement, **(c)** muscle pressure, **(d)** muscle force. Solid lines represent knee joint and dashed lines represent hip joint; vertical lines represent foot liftoff times.

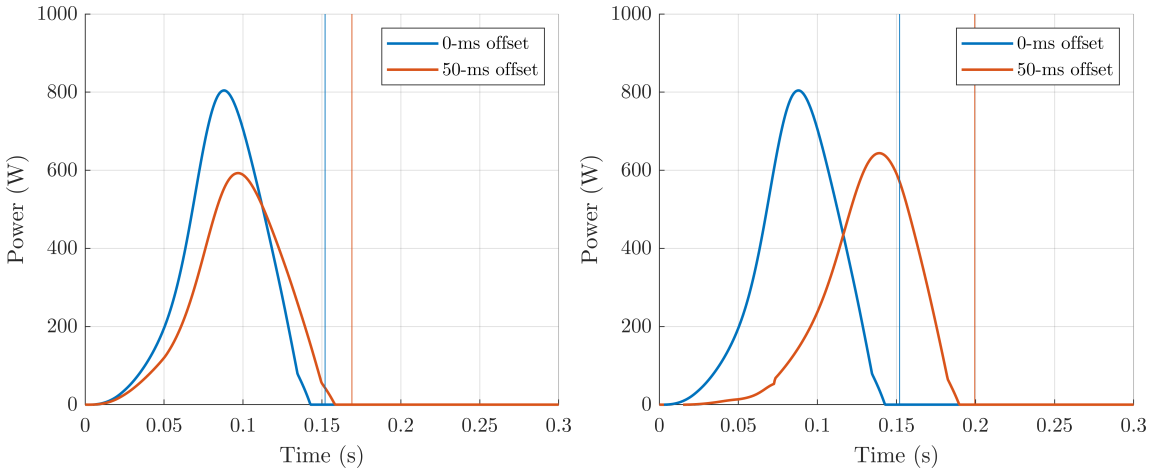

Figure 6.13: Comparison of robot center-of-mass power: **(a)** jump with hip activation 50 ms before knee activation versus jump with simultaneous hip and knee activation at time zero; **(a)** jump with knee activation 50 ms before hip activation vs jump with simultaneous activation. Vertical lines represent foot liftoff times.

Practical considerations. The above results suggest that to maximize squat jump height for the pneumatic muscle-driven robot, tendon stiffness should be maximized. However, the series stiffness characterized for the real jumping robot test platform in Chapter 5 was approximately 80 kN/cm, significantly lower than the upper stiffness range of 10 kN/cm in the aforementioned design optimizations. Consequently, the maximum simulated jump height for the same control timing parameters with the true robot stiffnesses was only 0.33 m, versus a greater-than 0.9-m height for maximum tendon stiffness. Jump height versus hip activation offset timing was still similar for the true stiffness configuration, although the timing window for the highest jumps was broader, as shown in Figure 6.14.

There are multiple sources of compliance on the real robot that contribute to the low series stiffness values, including:

- 3D-printed joint parts
- Tolerance stack-up of joint assemblies
- Metal tubing used to connect muscles to robot frame

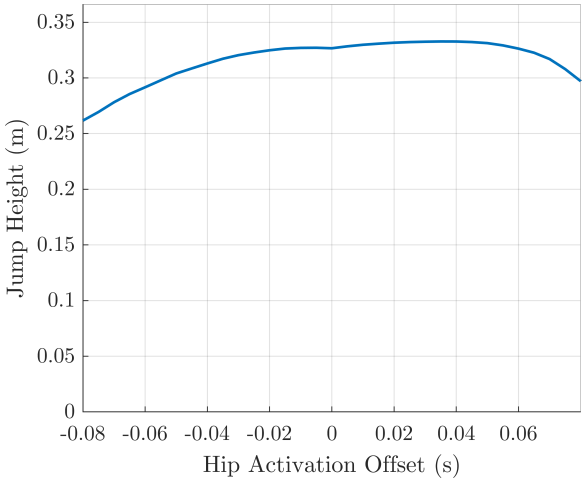

Figure 6.14: Jump height versus hip muscle activation offset time for true robot tendon stiffnesses.

- Thin carbon fiber tubes used for robot links (in fact, these tubes visibly deflect under muscle loading in slow-motion video)
- Connections between muscle and joint/robot frame (expandable polyester fabric sleeving used for muscle mesh and polypropylene webbing to connect mesh leads to joints).

Many of these design choices were made to minimize robot mass, and it would likely be a challenge to increase the effective series stiffness without increasing mass. Possible solutions to balance mass with stiffness include aluminum joint components and a thicker carbon fiber frame.

6.3.2 Angle-dependent moment arm optimization

To investigate the impact of variable mechanical advantage on robot jumping performance, the linear cam parameters—initial cam radius r_0 and slope m—were optimized with respect to jump height. The cam geometries at the hip and knee joints were treated independently. The initial cam radius was bounded from 0 to 8 cm, while the cam slope was bounded from -8 to 8 cm. Similar to the the series elasticity optimizations, all muscles were initially activated at time zero and sealed at 150 ms. The

series stiffness at the hip and knee joints was set to 80 kN/cm, as characterized in Chapter 5.

The optimal hip and knee cam parameters, corresponding to maximum jump height, are shown in Table 6.1: both the hip and knee joint cams start at a small initial radius and increase with joint angle rotation. To quantify the jumping improvement attributed variable mechanical advantage, additional optimizations were performed with fixed-radii pulleys in place of the cams; the same pulley was used for both hip and knee joints, such that the sole decision variable was pulley radius. As shown in Figure 6.15, the maximum jump height was achieved with a 4.5-cm radius. The optimized cams resulted in an 8.6 percent improvement in jump height over the pulley configuration.

Table 6.1: Optimal hip and knee cam parameters for maximum jump height.

Joint	Radius r_0 (cm)	Slope m (cm/rad)
Hip	0.0	3.0
Knee	1.3	3.8

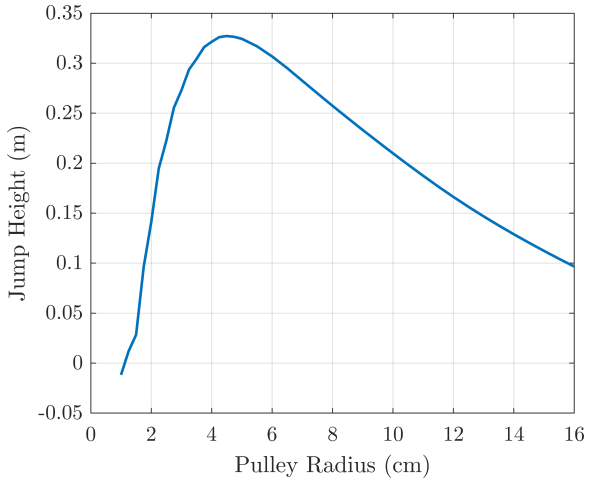

Figure 6.15: Jump height versus pulley radius, with the same pulley for both hip and knee joints.

An increasing moment arm versus joint angle boosts peak muscle forces and shift peak forces and torques later into the jump sequence, as shown in Figure 6.16. While

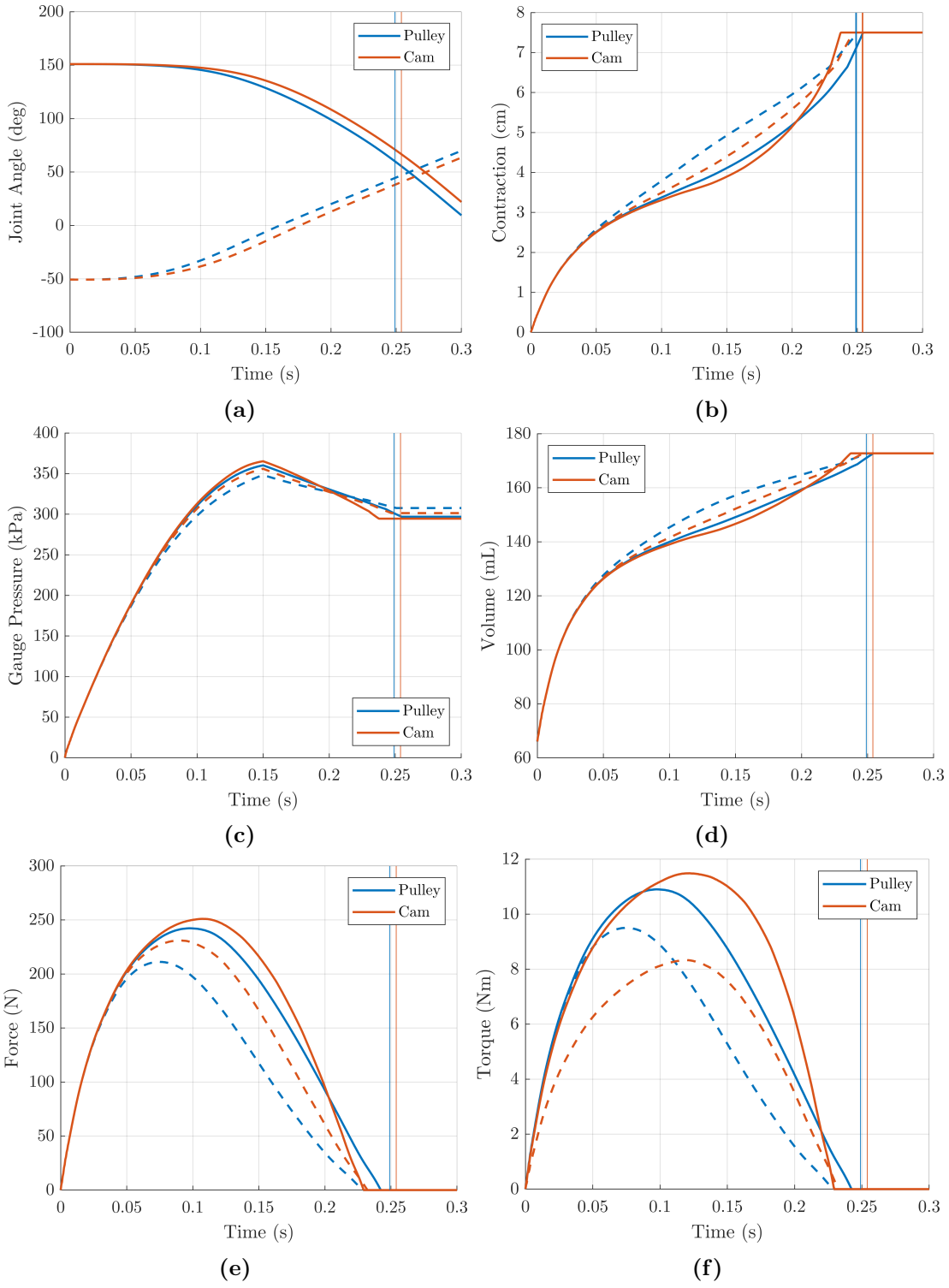

Figure 6.16: Comparison of robot joint dynamics for jump with 4.5-cm pulleys versus jump with optimized cams: **(a)** joint angle, **(b)** muscle contraction, **(c)** muscle pressure, **(d)** muscle volume, **(e)** muscle force, **(f)** joint torque. Solid lines represent knee joint and dashed lines represent hip joint; vertical lines represent foot liftoff times.

muscle forces are similar early in the jump (e), initial joint torques are lower with the optimized cams than with pulleys (f), since the initial radii of both the hip and knee cams are very small. With smaller torques early in the jump, there is less joint rotation at both the hip and knee joints (a), and consequently, there is less muscle contraction (b). This means that each muscle is operating higher on its force-length curve later in the jump. A second effect of reduced muscle contraction in early to mid-jump sequence is that muscle volumes are lower (d), so the muscles inflate more quickly and peak muscle pressures are higher (c). These altered muscle dynamics yield higher forces later in the jump that—combined with increasing moment arm versus joint angle—shift peak torques even further into the jump sequence, closer to foot liftoff; peak knee torque is also higher, while peak hip torque is slightly lower. This results in a higher robot jump power curve that is shifted closer to robot takeoff, as shown in Figure 6.17.

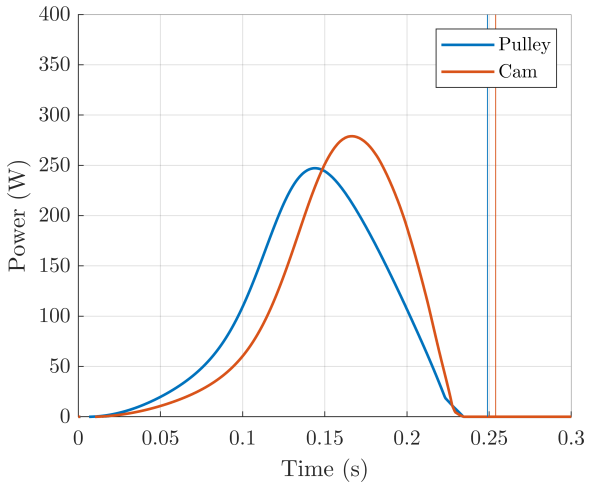

Figure 6.17: Comparison of robot center-of-mass power for jump with 4.5-cm pulleys versus jump with optimized cams. Vertical lines represent foot liftoff times.

From examination of joint angle and muscle force versus time for each jump, it appears that each pneumatic muscle applies force over a relatively small angle range. For the jump with cams in Figure 6.16, peak forces occur around 90-110 ms into the jump; by this time, the knee and hip joints have only rotated through approximately 5

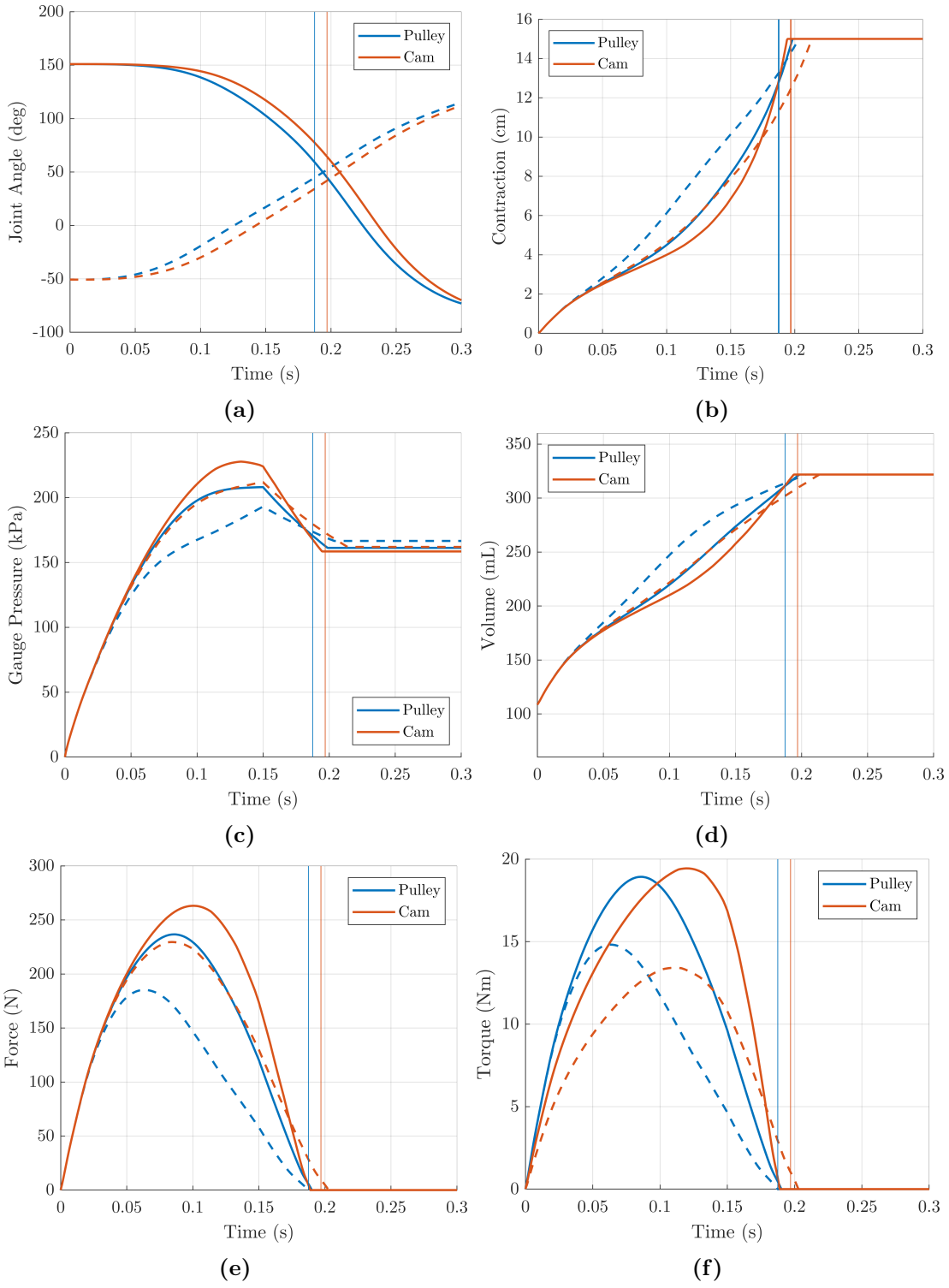

Figure 6.18: Comparison of robot joint dynamics for jumps with pulleys versus optimized cams, with 2x-length muscles: **(a)** joint angle, **(b)** muscle contraction, **(c)** muscle pressure, **(d)** muscle volume, **(e)** muscle force, **(f)** joint torque. Solid lines represent knee joint and dashed lines represent hip joint; vertical lines represent foot liftoff times.

and 10 degrees, respectively. At 230 ms, by which time forces have tapered to zero, the knee and hip joints have rotated approximately 64 and 80 degrees, respectively. This raises the question of whether a longer pneumatic muscle with greater contraction range may better utilize an angle-dependent moment arm by applying force over a larger joint angle range. To explore this, additional design optimizations were run with 1.5x and 2x nominal length muscles, again comparing jump height improvement using optimized cams to optimized constant-radius pulleys. The nominal muscle length—implemented on the experimental jumping robot test platform—is 21 cm, with a contraction range of approximately 7 cm from maximum force to zero force.

Indeed, with 1.5x longer muscles, the vertical robot jump was 12.5 percent higher using cams versus pulleys, and with 2x longer muscles, the jump was 14.7 percent higher. The cam-induced effects of higher force magnitudes and time-shifted peak forces/torques observed for the nominal length muscle study are more pronounced with longer muscles. Figure 6.18 shows the muscle and torque dynamics for the 2x length muscles: there is a larger difference in early muscle contraction between cam and pulley configurations, a larger difference in muscle force magnitudes, and consequently, a more significant joint torque shift closer to takeoff. As hypothesized,

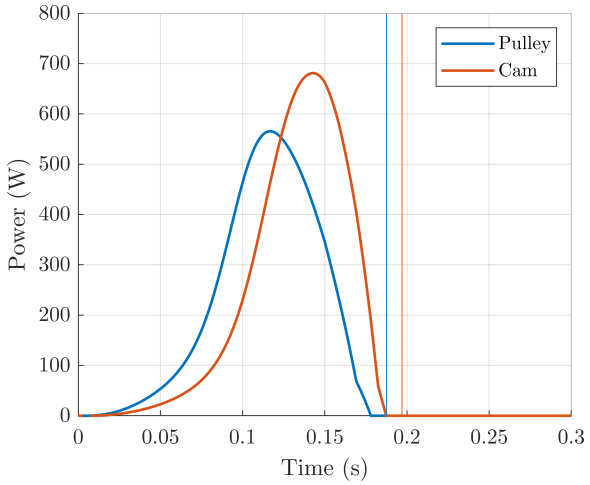

Figure 6.19: Comparison of robot center-of-mass power for jumps with pulleys versus optimized cams, with 2x-length muscles. Vertical lines represent foot liftoff times.

both the hip and knee muscles applied force over broader joint angle ranges (Figure 6.20). The joint angle displacement from time zero to the time at which muscle force decreased from its peak back to zero was 12 degrees larger at the knee and 17 deg larger at the hip for 2x muscle length robot configuration, as compared with the nominal muscle length configuration. Additionally, with longer muscles, there was a larger increase in robot center-of-mass power from pulley configuration to cam configuration, as shown in Figure 6.21.

Interestingly, longer pneumatic muscles also significantly increased jump height versus the nominal length muscles. With 1.5x longer muscles, the vertical jump was 1.8 times higher; with 2x longer muscles, the vertical jump was 2.3 times higher. The use of a longer muscle increases muscle volume, resulting in slower inflation rates and significantly lower peak pressures, as shown in Figure 6.20c. However, increasing muscle length allows each muscle to operate much higher on its force-length curve over a larger linear displacement, outweighing the decrease in muscle pressure. For example, at 100 ms into the jump, the nominal-length knee muscle has contracted 3.3 cm, 47 percent of its full range; the 2x-length knee muscle has contracted 4 cm (more than the nominal case), but this is only 29 percent of its full range. This extended contraction range, in turn, allows for the use of a much steeper increase in moment arm throughout joint rotation, since a higher linear displacement is required with a larger moment arm for the same angular displacement. As shown in Figure 6.20, peak force magnitudes are similar for the nominal and 2x muscle length jumps (e), but peak torques are significantly higher with 2x length muscles (f). Higher peak torques produce a much faster jump sequence, in which the liftoff time is more than 50 ms earlier with 2x-length muscles. As a result, peak jumping power is significantly higher with longer muscles and is shifted much closer to liftoff time.

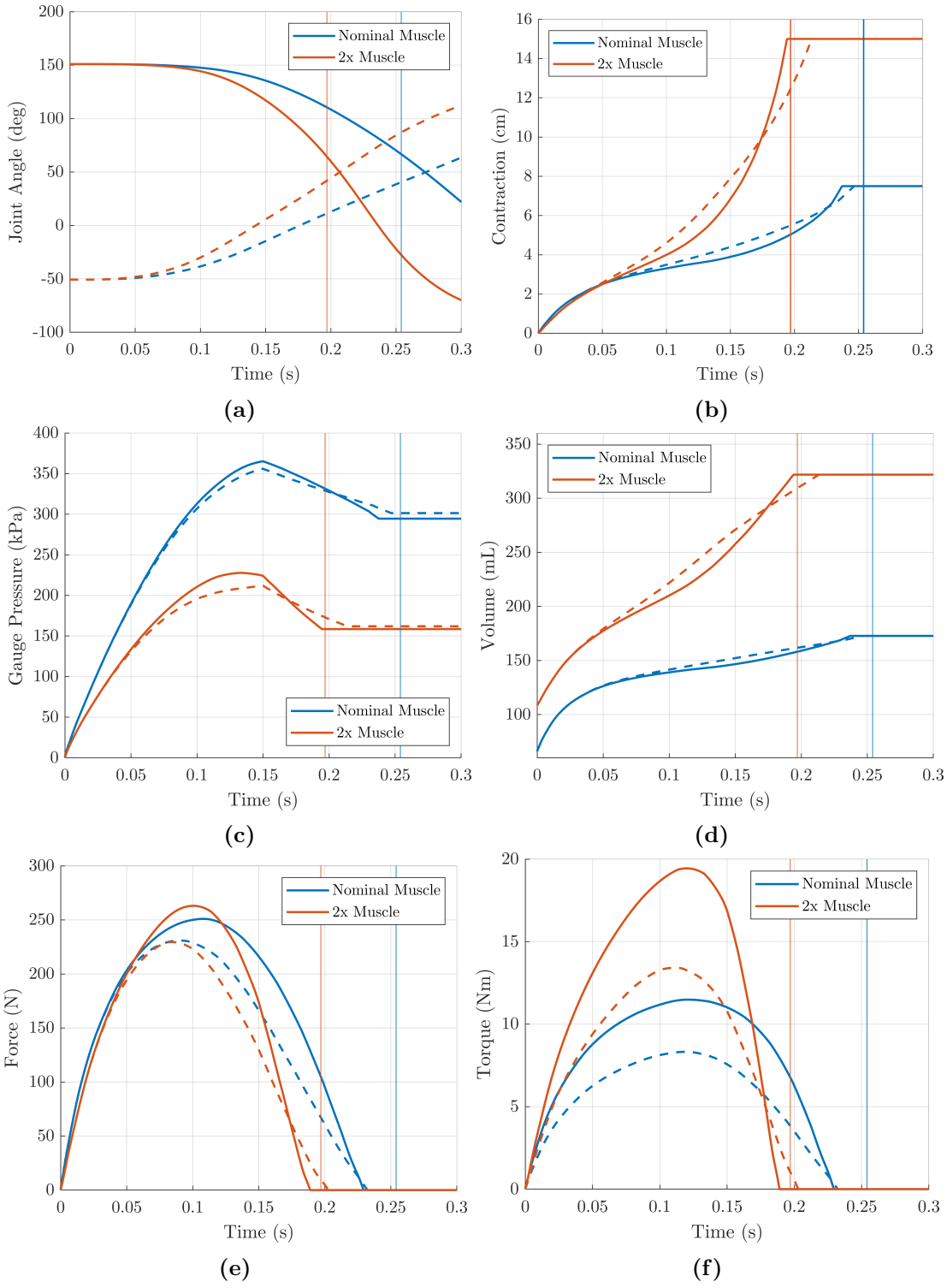

Figure 6.20: Comparison of robot joint dynamics for jump with 2x-length muscles versus jump with nominal-length muscles: **(a)** joint angle, **(b)** muscle contraction, **(c)** muscle pressure, **(d)** muscle volume, **(e)** muscle force, **(f)** joint torque. Solid lines represent knee joint and dashed lines represent hip joint; vertical lines represent foot liftoff times.

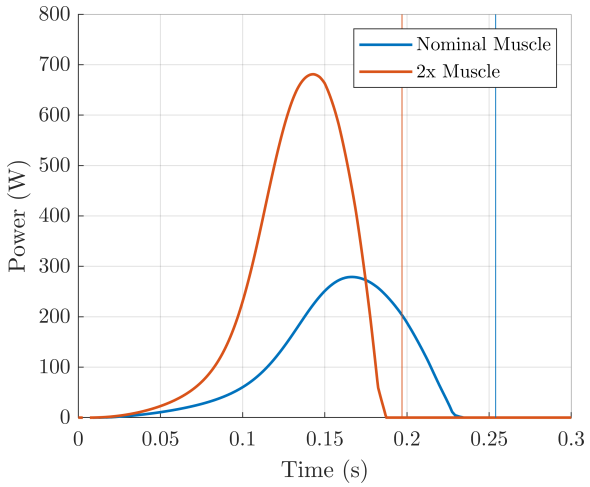

Figure 6.21: Comparison of robot center-of-mass power for jump with 2x-length muscles versus jump with nominal-length muscles. Vertical lines represent foot liftoff times.

Practical considerations. The above results indicate that longer pneumatic muscles can significantly improve jumping performance by allowing each muscle to operate higher along its force-length curve. In fact, additional optimizations showed that pneumatic muscle lengths of 4-5x the nominal muscle length marginally improve jump height, before the increase in muscle volume and corresponding decrease in muscle pressure begin to outweigh the benefits of longer muscle contraction range. In practice, though, it is not necessarily straightforward to implement longer muscles on a physical robot. For mono-articular muscles (acting on one joint), longer link lengths are required to accommodate longer muscles. On the current jumping robot with 0.5-meter links, muscle lengths cannot be extended much further without increasing link length.

A pulley system could potentially be used to add longer muscles without increasing link lengths; however, this would add complexity and weight to the robot. A better idea might be to imitate biology and use bi-articular muscles that span multiple joints and links, in place of, or in parallel with mono-articular muscles. For example, mono-articular knee extensor muscles in the human body have contraction ranges of around 4 to 6 cm—similar to the nominal pneumatic muscle contraction range in this

work—while bi-articular hip-knee muscles have contraction ranges of around 12 to 16 cm [102]. The use of bi-articular muscles would add many additional dimensions to the design optimization of pneumatic muscle-driven robots.

6.3.3 Combined optimization

A combined design optimization study was performed to determine whether series elasticity and angle-dependent moment parameters influence each other when these mechanisms are used together. For maximizing robot squat jump height from a static pose, optimal parameters were consistent with the individual design studies:

- Maximum series elastic stiffness
- Increasing moment arm versus joint angle, starting from small initial radius
- Minimal activation time offset between hip and knee muscles

The same results held true for the 2x muscle length configuration. These results reinforce the analyses of of muscle dynamics in the previous sections, with series elasticity and moment arm treated separately. However, it is likely that for sequential or cyclical robot maneuvers, in which maximum stiffness might not be optimal, there may be a stronger relationship between stiffness and moment arm profile. Therefore, in future work, it is important to again analyze impact of these different joint mechanisms on muscle dynamics and robot performance both individually and together.

6.4 Discussion

Series elasticity. Optimization of series elastic stiffnesses on the jumping robot suggests that for squat jumps from a static pose, maximizing robot stiffness is critical to jumping higher. Any amount of compliance permits each pneumatic muscle to contract more during the first 100 ms of the jump sequence—this increases muscle inflation time, due to the muscle's volume-contraction relationship, and reduces muscle

force range, due to the muscle's force-contraction relationship.

For the jumping robot test platform, the effective series stiffness at each joint is quite low because of the materials and designs chosen to reduce overall mass (carbon fiber links, 3D-printed joints, muscle attachment materials, etc.). A future study could investigate the trade-off between robot stiffness and mass, with regard for jumping performance. This would likely require multiple iterations of robot design, fabrication, and experimental evaluation, as it is difficult to analytically quantify the influences of material and design choices on robot stiffness.

Muscle activation timing did not affect optimal stiffness values. Additionally, it was shown that nearly-simultaneous muscle activation times yield the highest jumps. Any timing offset between hip and knee muscle activations delays peak knee muscle pressures to later in the jump sequence, when muscle contraction is higher and max force capability is lower (muscles operating lower on force-length curve); the same is true for hip muscles when knee muscles are activated first. Thus, it is best for both hip and knee muscles to contract nearly simultaneously to take advantage of higher force output at longer muscle lengths.

Biological muscle has similar force versus length characteristics to the pneumatic muscle, with reduced force output as the muscle contracts (though not necessarily monotonically for biological muscles). However, biological muscle force is also strongly dependent on contraction velocity, whereas the pneumatic muscle is not. This difference may be one reason why series elasticity is not beneficial for pneumatic muscle-driven squat jumps. Nevertheless, biological tendons are evolved for a broad range of animal dynamics, not specifically for squat jumping. Stiffer tendons may be better for squat jumps, while more compliant tendons may be favorable in other activities. Particularly for sequential moves like countermovement jumping (squat down and jump up in a continuous motion) or cyclical tasks like walking, running, and hopping, series elastic elements can recover and redistribute kinetic energy to

improve animal dynamics and energy efficiency [103]–[105]. As shown in many examples across the literature, the same is true for non-pneumatic-muscle-driven jumping robots [52], [59], [93], [106]. Thus, series elasticity still may be advantageous for more complex sequential or cyclical maneuvers on the pneumatic muscle-driven jumping robot.

Variable mechanical advantage. Optimization of joint angle-dependent moment arm showed that an increasing moment arm versus joint angle profile, starting from a small initial moment arm, improves jumping performance. A small initial cam radius allows each muscle to pressurize without generating as much robot movement early in the jump. Less early muscle displacement subsequently allows each muscle to operate higher on its force-length curve later in the jump and displace a larger moment arm through a similar angle, as compared to a fixed-radius pulley configuration. This ultimately increases peak torque later in the jump sequence, maximizing joint power closer to robot liftoff. This effect was more pronounced with longer muscles.

Longer muscles also significantly improved overall jumping performance for a given robot configuration, as the benefits of increased muscle contraction range—operation higher on the force-length curve and angular displacement of a larger moment arm—outweighed the reduced muscle operating pressures related to larger muscle volume. As stated in the experimental section, increasing muscle length marginally improved jump height up to 4-5x nominal muscle length. However, it is not feasible to configure muscles of this length on a real robot; even 1.5x length muscles would be difficult to swap into the robot without increasing link length. This motivates future design explorations using bi-articular muscles in parallel with mono-articular muscles, were bi-articular muscles would provide longer contraction ranges, but with slower pressurization.

A number of studies have explored the use of bi-articular pneumatic muscles on

legged robots, aiming to replicate the musculoskeletal layouts of humans or animals [63], [65], [107], [108]. Rather than trying to precisely match biology, it would be valuable to investigate muscular configurations that maximize robot performance. Mono- and bi-articular muscle configurations, and their corresponding muscle lengths, would be added as design optimization parameters. Mono- and bi-articular muscles could utilize the same cam geometry at each joint or act on separate cam profiles. Based on the above design optimization results for longer mono-articular muscles, optimization of pneumatic muscle configuration may have a significant impact on robot capabilities.

Scope of results. The design optimizations in this chapter focused on a single robot morphology for a squat jump from a specific robot pose. This study could be vastly expanded in several directions. The relationship between robot morphology—link lengths in particular—and design optimization parameters like series elastic stiffness and variable moment arm cam geometry could be investigated; or, link lengths could even be added as design optimization parameters. It would also be insightful to examine how optimal design parameters change for different initial robot poses. This would be particularly important for robot operation in the wild, where the robot would likely rarely jump from perfectly level ground. Additionally, this study focused specifically on maximizing vertical jump height. Further optimization analyses may be expanded to include multiple objectives such as lateral jump distance, countermovement jump height, ground-foot clearance, etc. Finally, the burst inflation control methodology used in this work is not necessarily limited to a single inflation window per muscle. For sequential robot maneuvers, multi-step inflation-seal-deflation sequences could be utilized. Like the other potential research directions discussed here, this would add significant complexity to the design optimization.

6.5 Significance

In this chapter, several design optimization studies were performed to gain insight into impacts of series elasticity, joint angle-dependent mechanical advantage, muscle activation timing, and nominal muscle length on robot jumping performance. While these studies focused on one objective (vertical jump height) for one particular robot, the overall pneumatic muscle-driven robot model and design optimization approach developed in this work can be applied to any muscle-driven robot morphology. It is straightforward to add series elastic elements and variable moment arm cams to any robot morphology in simulation before building the robot. One can then evaluate key performance objectives to inform the design of a muscle-driven robot.

This work also lays out future directions for pneumatic muscle-driven robot design research. Optimization of mono- and bi-articular muscle configurations and muscle lengths may be particularly promising for dynamic tasks like jumping. The muscle-driven robot model and optimization approach in this thesis can be readily utilized for these future studies.

CHAPTER 7
CONCLUSION

7.1 Research contributions

Mechanical compliance brings a host of potential benefits to robotics, from enhanced safety in human-robot interactions, to simplified low-level control, and increased resilience to uncertainty in the world. Soft robot actuators—such as pneumatic artificial muscle—are well-suited for this purpose. However, there exist several core implementation challenges for the pneumatic muscle, including: compatible sensing technologies, limitations in actuation speed and force generation capabilities, and application of conventional high-level planning and control strategies. This thesis makes progress towards solving these challenges, specifically for pneumatic muscle-driven systems, via three main contributions:

1. **Sensing**: A sensorized pneumatic artificial muscle is developed using a novel reflective optical sensor design. This two-in-one sensor-actuator package can be readily incorporated into a robotic system to provide lightweight, compliant actuation with kinematic and dynamic estimation capabilities.

2. **Modeling and planning**: A pneumatic muscle-driven robot model is developed, incorporating pneumatic system dynamics, muscle dynamics, and rigid body robot dynamics. The pneumatic system model is formulated for a 'burst-inflation' control approach that eliminates the requirement for heavier proportional valves which limit system mobility. The overall system model is integrated into a trajectory optimization factor graph framework for planning agile robot maneuvers. The trajectory planning approach accommodates hybrid robot dynamics for modeling robot-environment contacts with known contact sequence.

3. **Design optimization**: The pneumatic muscle-driven robot model is used to investigate how biological mechanisms, such as angle-dependent mechanical advantage, can compensate for pneumatic muscle force-length limitations. This exploration provides insight into the impacts of various design parameters on pneumatic muscle dynamics and their effects on robot performance, using a jumping robot case study.

Building on these contributions, there are a number of potential directions for future work, including:

Sensing

- *Combining sensor-embedded pneumatic muscles with trajectory planning approach*: For example, sensor-embedded muscles could be used on the jumping robot to estimate muscle forces during takeoff, compare actual forces to those of the planned jump, and compensate for trajectory error by adjusting the landing pose of the robot. Furthermore, estimated muscle force could be used to sense robot landing and strategically vent the pneumatic muscles to reduce robot deceleration.

Modeling and planning

- *Investigation of additional pneumatic system models*: On one hand, a more comprehensive pneumatic system model that explicitly includes all components in the flow path and removes assumptions on the fluid dynamics could be evaluated; it would be insightful to determine whether the improvement in accuracy outweighs the significant increase in complexity, as well as to quantify the computational impact on trajectory planning. On the other hand, a fully data-driven approach could explore the performance of various models fit to

experimental data; this would likely require a broader set of experiments to capture the full pneumatic system dynamics.

- *Application of trajectory planning to more complex maneuvers*: It would be valuable to investigate how well the trajectory planning approach in this work performs for sequential robot maneuvers, such as a countermovement squat jump or an immediate second jump upon landing. The ability to perform these types of sequential movements could further improve the agility of pneumatic muscle-driven robots.

- *Incorporation of more sophisticated performance objectives into trajectory planning*: Jumping robot objectives, such as foot-obstacle clearance and landing pose on uneven terrain should be readily accommodated by the trajectory optimization approach in this work.

Design optimization

- *Exploration of potential benefits of series elasticity for sequential robot maneuvers*: Additionally, future work could revisit optimization of series elastic stiffness for these same types of sequential moves, during which kinetic can be stored and released via pneumatic muscle tendons.

- *Investigation of optimal mono- and bi-articular muscle configurations to improve robot performance*: As detailed in Chapter 6, longer muscles can significantly improve theoretical robot performance by allowing each muscle to operate much higher on its force-length curve over a larger joint displacement; however, it is difficult to accommodate longer muscles without changing robot morphology. Taking inspiration from biology, bi-articular muscle configurations can accommodate longer muscles.

7.2 Application of pneumatic muscles

It is important to consider the practical implications of using pneumatic artificial muscles on mobile robots. The main limitation of pneumatic-powered robotic systems, as compared to more common battery-powered motor-driven systems, is energy density—a battery can store more energy per mass than a compressed air tank. However, in the right context, pneumatic muscles may be useful for incorporating mechanical compliance into a robotic system. Consider a simple case study for the two-legged jumping robot, exploring both pneumatic muscle and motor-driven configurations. In each case, the design target is 15-Nm peak torque over a 200-ms jump sequence, with maximum angular joint velocities of 10 rad/s.

For the pneumatic system, a 1.5-L carbon fiber-wrapped aluminum compressed air tank (Ninja Paintball SL2) with 1.1-kg mass is selected to store compressed air. At its maximum operating pressure of 4500 psi (31 MPa), the tank holds just over 0.5 kg of air. The over-designed high-flow valve used for the jumping robot in this work has a mass of 165 g; but, other suitable valves with similar flow rate performance are around 100 g. A small 450-mAh 50-g battery (Venom Fly 3S LiPo) is selected for valve power, with energy storage several orders of magnitude above that required for the number of jumps per air tank. Finally, each pneumatic muscle is approximately 80 g, resulting in a total pneumatic system mass of around 2.4 kg. For muscle pressurization up to 345 kPa, each tank fill-up can supply about 200 jumps.

For the motor-driven system, a small brushless motor (Maxon EC 45) with 50:1 gearbox (Maxon GPX 42) is selected to actuate each joint; the total mass of the motor and gearbox is 0.8 kg. Using a 3600-mAh battery with 0.56-kg mass (Venom Fly 6S LiPo), the robot can jump nearly 2000 times. Yet, the total system mass increases to about 3.8 kg. Thus, there are mass trade-offs between the two systems. The pneumatic system operating time is limited by its energy source (air tank and

compressed air) and the system will incur a significant increase in energy source mass for operating times comparable to motor-driven systems. Conversely, the energy source mass for the motor-driven system is much lower, but the minimum system mass is limited by the larger actuator mass of the motor/gearbox, compared with the pneumatic muscle.

More importantly, the motor/gearbox system provides no mechanical compliance—the large gear ratio gear box is non-backdrivable, resulting in a very stiff robot leg. One alternative to mitigate this disadvantage of motor-driven systems is to use a quasi-direct-drive motor with very low gear ratio (in the range of 5:1), such that torque can be transmitted in reverse from the robot link back to its driving motor. This configuration allows for active control of joint impedance. However, direct-drive motors must be bigger and heavier to achieve useful peak torques. For example, the MIT Cheetah robot motor and gearbox mass is approximately 1.2 kg [109].

Another alternative is to use a series elastic actuator (SEA), in which mechanical compliance is added between a motor's gearbox output and the robot joint. This reduces joint impedance and also allows for very precise torque measurement and control. Like quasi-direct-drive motors though, SEAs are typically heavier; for example, the ANYmal robot SEA is 0.87 kg [58]. Additionally, for both direct-drive and SEA systems, virtual joint impedance requires active motor control, reducing energy efficiency.

Overall, electric motor actuation systems are very efficient and provide extended robot run times, but require higher-mass actuators to produce the torques required for fast robot motion. In contrast, pneumatic muscle actuation systems offer the benefits of low actuator mass and passive compliance, but have limited run times without substantially increasing energy source mass. While several studies have explored using chemical reactions, such as combustion and monopropellant decomposition, to improve energy density, significant development work is still required [110]–[113].

However, conventional compressed air-powered pneumatic muscle systems may still be advantageous, particularly for hybrid drive systems, in which muscles are connected in series with low-power motors. Small motors would be used for slower, energy-efficient robot operation, without the torque and angular velocity capabilities required for fast dynamics. The pneumatic muscle system would then enable a limited number of explosive robot maneuvers using the burst inflation approach presented in this work. Furthermore, the pneumatic muscles would act as tunable stiffness elements, adding passive variable mechanical compliance to the robot. For example, a mobile legged robot might use low-power motors to efficiently explore its environment over an extended period of time, while periodically employing its pneumatic muscle system to leap over large obstacles in its path. This hybrid motor-muscle actuation scheme represents a promising research direction for mobile robots that require fast actuation and mechanical compliance.

7.3 Summary

Mechanical compliance facilitates safe and robust robot adaptation to the surrounding world, which is particularly advantageous in responding to environmental uncertainty and in interacting safely with people. The pneumatic artificial muscle offers a unique solution for passively-compliant robot actuation. However, the pneumatic muscle is limited by a lack of compatible sensor technologies. Thus, a novel pneumatic muscle design with integrated optical sensing is developed to overcome this challenge. Additionally, the pneumatic muscle has limitations in its force and contraction range characteristics, similar to biological muscle. But, like biological muscle in animals, pneumatic muscles can generate fast, dynamic robot motion with appropriate design and control strategies, as demonstrated in this work. Thus it is hoped that this thesis serves as a guide to exploiting the benefits of compliant pneumatic muscle actuation—via integrated muscle sensing, optimized joint mechanism design, and motion planning

for burst-inflation control—while maximizing robot agility.

Appendices

APPENDIX A

JUMPING ROBOT SIMULATION DESCRIPTION FILE

Below is the Simulation Description Format (SDF) file for the planar two-legged jumping robot.

```
<sdf version='1.6'>
  <model name='jumping_robot'>
    <link name='l0'>
      <pose frame=''>0 0 0 0 -0 0</pose>
      <inertial>
        <pose frame=''>0 0 0 0 -0 0</pose>
        <mass>0.0001</mass>
        <inertia>
          <ixx>0.0001</ixx>
          <ixy>0</ixy>
          <ixz>0</ixz>
          <iyy>0</iyy>
          <iyz>0</iyz>
          <izz>0.0001</izz>
        </inertia>
      </inertial>
    </link>
    <link name='l1'>
      <pose frame=''>0 0.437 0 0.148 -0 0</pose>
      <inertial>
        <pose frame=''>0 0 0.275 0 -0 0</pose>
        <mass>0.285</mass>
        <inertia>
          <ixx>0.007212875</ixx>
          <ixy>0</ixy>
          <ixz>0</ixz>
          <iyy>0.007212875</iyy>
          <iyz>0</iyz>
          <izz>0.0001</izz>
        </inertia>
      </inertial>
    </link>
    <link name='l2'>
      <pose frame=''>0 0.356 0.544 0.148 -0 0</pose>
      <inertial>
        <pose frame=''>0 0 0.275 0 -0 0</pose>
        <mass>0.428</mass>
        <inertia>
```

```
      <ixx>0.010831966666667</ixx>
      <ixy>0</ixy>
      <ixz>0</ixz>
      <iyy>0.010831966666667</iyy>
      <iyz>0</iyz>
      <izz>0.0001</izz>
    </inertia>
  </inertial>
</link>
<link name='l3'>
  <pose frame=''>0 0 1.088 0 -0 0</pose>
  <inertial>
    <pose frame=''>0 0 0 0 -0 0</pose>
    <mass>0.883</mass>
    <inertia>
      <ixx>0.022347258333333</ixx>
      <ixy>0</ixy>
      <ixz>0</ixz>
      <iyy>0.0001</iyy>
      <iyz>0</iyz>
      <izz>0.022347258333333</izz>
    </inertia>
  </inertial>
</link>
<link name='l4'>
  <pose frame=''>0 -0.356 0.544 -0.148 0 0</pose>
  <inertial>
    <pose frame=''>0 0 0.275 0 0 0</pose>
    <mass>0.428</mass>
    <inertia>
      <ixx>0.010831966666667</ixx>
      <ixy>0</ixy>
      <ixz>0</ixz>
      <iyy>0.010831966666667</iyy>
      <iyz>0</iyz>
      <izz>0.0001</izz>
    </inertia>
  </inertial>
</link>
<link name='l5'>
  <pose frame=''>0 -0.437 0 -0.148 0 0</pose>
  <inertial>
    <pose frame=''>0 0 0.275 0 0 0</pose>
    <mass>0.285</mass>
    <inertia>
      <ixx>0.007212875</ixx>
      <ixy>0</ixy>
      <ixz>0</ixz>
      <iyy>0.007212875</iyy>
```

```
      <iyz>0</iyz>
      <izz>0.0001</izz>
    </inertia>
  </inertial>
</link>
<joint name='j0' type='revolute'>
  <pose frame='world'> 0 0.437 0 0 0 0</pose>
  <child>l1</child>
  <parent>l0</parent>
  <axis>
    <xyz>1 0 0</xyz>
    <limit>
      <lower>0</lower>
      <upper>0</upper>
      <effort>1000</effort>
      <velocity>0.5</velocity>
    </limit>
    <dynamics>
      <damping>500</damping>
      <friction>0</friction>
      <spring_reference>0</spring_reference>
      <spring_stiffness>0</spring_stiffness>
    </dynamics>
  </axis>
</joint>
<joint name='j1' type='revolute'>
  <pose frame='world'> 0 0.356 0.544 0 0 0</pose>
  <child>l2</child>
  <parent>l1</parent>
  <axis>
    <xyz>1 0 0</xyz>
    <limit>
      <lower>0</lower>
      <upper>0</upper>
      <effort>1000</effort>
      <velocity>0.5</velocity>
    </limit>
    <dynamics>
      <damping>500</damping>
      <friction>0</friction>
      <spring_reference>0</spring_reference>
      <spring_stiffness>0</spring_stiffness>
    </dynamics>
    <use_parent_model_frame>1</use_parent_model_frame>
  </axis>
</joint>
<joint name='j2' type='revolute'>
  <pose frame='world'> 0 0.275 1.088 0 0 0</pose>
  <child>l3</child>
```

```
  <parent>l2</parent>
  <axis>
    <xyz>1 0 0</xyz>
    <limit>
      <lower>-1.57</lower>
      <upper>1.57</upper>
      <effort>1000</effort>
      <velocity>0.5</velocity>
    </limit>
    <dynamics>
      <damping>500</damping>
      <friction>0</friction>
      <spring_reference>0</spring_reference>
      <spring_stiffness>0</spring_stiffness>
    </dynamics>
    <use_parent_model_frame>1</use_parent_model_frame>
  </axis>
</joint>
<joint name='j3' type='revolute'>
  <pose frame='world'> 0 -0.275 1.088 0 0 0</pose>
  <child>l3</child>
  <parent>l4</parent>
  <axis>
    <xyz>-1 0 0</xyz>
    <limit>
      <lower>-1.57</lower>
      <upper>1.57</upper>
      <effort>1000</effort>
      <velocity>0.5</velocity>
    </limit>
    <dynamics>
      <damping>500</damping>
      <friction>0</friction>
      <spring_reference>0</spring_reference>
      <spring_stiffness>0</spring_stiffness>
    </dynamics>
    <use_parent_model_frame>1</use_parent_model_frame>
  </axis>
</joint>
<joint name='j4' type='revolute'>
  <pose frame='world'> 0 -0.356 0.544 0 0 0</pose>
  <child>l4</child>
  <parent>l5</parent>
  <axis>
    <xyz>-1 0 0</xyz>
    <limit>
      <lower>-1.57</lower>
      <upper>1.57</upper>
      <effort>1000</effort>
```

```
          <velocity>0.5</velocity>
        </limit>
        <dynamics>
          <damping>500</damping>
          <friction>0</friction>
          <spring_reference>0</spring_reference>
          <spring_stiffness>0</spring_stiffness>
        </dynamics>
        <use_parent_model_frame>1</use_parent_model_frame>
      </axis>
    </joint>
    <joint name='j5' type='revolute'>
      <pose frame='world'> 0 -0.437 0 0 0 0</pose>
      <child>l5</child>
      <parent>l0</parent>
      <axis>
        <xyz>-1 0 0</xyz>
        <limit>
          <lower>0</lower>
          <upper>0</upper>
          <effort>1000</effort>
          <velocity>0.5</velocity>
        </limit>
        <dynamics>
          <damping>500</damping>
          <friction>0</friction>
          <spring_reference>0</spring_reference>
          <spring_stiffness>0</spring_stiffness>
        </dynamics>
      </axis>
    </joint>
  </model>
</sdf>
```

REFERENCES

[1] C. Majidi, *Soft Robotics: A Perspective - Current Trends and Prospects for the Future*, Mar. 2014.

[2] D. Rus and M. T. Tolley, *Design, fabrication and control of soft robots*, May 2015.

[3] C. Laschi, B. Mazzolai, and M. Cianchetti, "Soft robotics: Technologies and systems pushing the boundaries of robot abilities," *Science Robotics*, vol. 1, no. 1, eaah3690, 2016.

[4] C. D. Onal, "System-level challenges in pressure-operated soft robotics," in *Micro- and Nanotechnology Sensors, Systems, and Applications VIII*, T. George, A. K. Dutta, and M. S. Islam, Eds., vol. 9836, SPIE, May 2016, p. 983 627.

[5] P. Polygerinos, N. Correll, S. A. Morin, B. Mosadegh, C. D. Onal, K. Petersen, M. Cianchetti, M. T. Tolley, and R. F. Shepherd, "Soft Robotics: Review of Fluid-Driven Intrinsically Soft Devices; Manufacturing, Sensing, Control, and Applications in Human-Robot Interaction," *Advanced Engineering Materials*, vol. 19, no. 12, p. 1 700 016, Dec. 2017.

[6] P. Boyraz, G. Runge, and A. Raatz, "An Overview of Novel Actuators for Soft Robotics," *Actuators*, vol. 7, no. 3, p. 48, Aug. 2018.

[7] S. Wakimoto, K. Suzumori, and T. Kanda, "Development of Intelligent McKibben Actuator," in *2005 IEEE/RSJ International Conference on Intelligent Robots and Systems*, 2005, pp. 487–492, ISBN: 2153-0858.

[8] S. Kuriyama, M. Ding, Y. Kurita, T. Ogasawara, and J. Ueda, "Flexible Sensor for Mckibben Pneumatic Actuator," in *Sensors, 2009 IEEE*, 2009, pp. 520–525, ISBN: 1930-0395.

[9] Y.-L. Park and R. J. Wood, "Smart pneumatic artificial muscle actuator with embedded microfluidic sensing," in *SENSORS, 2013 IEEE*, 2013, pp. 1–4, ISBN: 1930-0395.

[10] J. Misumi, S. Wakimoto, and K. Suzumori, "Experimental investigation of conductive fibers for a smart pneumatic artificial muscle," in *2015 IEEE International Conference on Robotics and Biomimetics (ROBIO)*, 2015, pp. 2335–2340.

[11] W. Felt, K. Y. Chin, and C. D. Remy, "Contraction Sensing with Smart Braid McKibben Muscles," *IEEE/ASME Transactions on Mechatronics*, vol. 21, no. 3, pp. 1201–1209, 2016.

[12] O. Erin, N. Pol, L. Valle, and Y. L. Park, "Design of a bio-inspired pneumatic artificial muscle with self-contained sensing," in *2016 38th Annual International Conference of the IEEE Engineering in Medicine and Biology Society (EMBC)*, 2016, pp. 2115–2119.

[13] T. Akagi, S. Dohta, Y. Kenmotsu, F. Zhao, and M. Yoneda, "Development of Smart Inner Diameter Sensor for Position Control of Mckibben Artificial Muscle," *Procedia Engineering*, vol. 41, pp. 105–112, 2012.

[14] B. Jamil, S. Lee, and Y. Choi, "Conductive Knit-covered Pneumatic Artificial Muscle (k-PAM) Actuator," in *2018 IEEE/RSJ International Conference on Intelligent Robots and Systems (IROS)*, 2018, pp. 1476–1481, ISBN: 9781538680933.

[15] W. Felt, K. Y. Chin, and C. D. Remy, "Smart Braid Feedback for the Closed-Loop Control of Soft Robotic Systems," *Soft Robotics*, vol. 4, no. 3, soro.2016.0056, Sep. 2017.

[16] S. Wakimoto, J. Misumi, and K. Suzumori, "New concept and fundamental experiments of a smart pneumatic artificial muscle with a conductive fiber," *Sensors and Actuators A: Physical*, vol. 250, pp. 48–54, Oct. 2016.

[17] W. Felt and C. D. Remy, "Smart braid: Air muscles that measure force and displacement," in *IEEE International Conference on Intelligent Robots and Systems*, IEEE, Sep. 2014, pp. 2821–2826, ISBN: 9781479969340.

[18] L. Tiziani, T. Cahoon, and F. Hammond, "Sensorized pneumatic muscle for force and stiffness control," *Proceedings - IEEE International Conference on Robotics and Automation*, pp. 5545–5552, 2017.

[19] N. Farrow and N. Correll, "A soft pneumatic actuator that can sense grasp and touch," *IEEE International Conference on Intelligent Robots and Systems*, vol. 2015-Decem, no. Ecoflex 0030, pp. 2317–2323, 2015.

[20] R. A. Bilodeau, E. L. White, and R. K. Kramer, "Monolithic fabrication of sensors and actuators in a soft robotic gripper," *IEEE International Conference on Intelligent Robots and Systems*, vol. 2015-Decem, pp. 2324–2329, 2015.

[21] J. Morrow, H. S. Shin, C. Phillips-Grafflin, S. H. Jang, J. Torrey, R. Larkins, S. Dang, Y. L. Park, and D. Berenson, "Improving Soft Pneumatic Actuator fingers through integration of soft sensors, position and force control, and

rigid fingernails," *Proceedings - IEEE International Conference on Robotics and Automation*, vol. 2016-June, pp. 5024–5031, 2016.

[22] J. H. So, J. Thelen, A. Qusba, G. J. Hayes, G. Lazzi, and M. D. Dickey, "Reversibly deformable and mechanically tunable fluidic antennas," *Advanced Functional Materials*, vol. 19, no. 22, pp. 3632–3637, 2009.

[23] B. Tondu and P. Lopez, "Modeling and control of McKibben artificial muscle robot actuators," *IEEE Control Systems Magazine*, vol. 20, no. 2, pp. 15–38, 2000.

[24] D. P. Holland, E. J. Park, P. Polygerinos, G. J. Bennett, and C. J. Walsh, "The Soft Robotics Toolkit: Shared Resources for Research and Design," *Soft Robotics*, vol. 1, no. 3, pp. 224–230, 2014.

[25] I. D. Joshipura, H. R. Ayers, C. Majidi, and M. D. Dickey, "Methods to pattern liquid metals," *Journal of Materials Chemistry C*, vol. 3, no. 16, pp. 3834–3841, 2015.

[26] H. Zhao, K. O'Brien, S. Li, and R. F. Shepherd, "Optoelectronically innervated soft prosthetic hand via stretchable optical waveguides," *Science Robotics*, vol. 1, no. 1, 2016.

[27] C. To, T. L. Hellebrekers, and Y. Park, "Highly stretchable optical sensors for pressure, strain, and curvature measurement," in *2015 IEEE/RSJ International Conference on Intelligent Robots and Systems (IROS)*, 2015, pp. 5898–5903, ISBN: VO -.

[28] F. Caralt, J. L. Molnar, J. P. Stingel, T. W. Cahoon, and F. L. Hammond, "Diffusion-based optical sensors for multimodal strain measurement in soft devices," in *2017 IEEE SENSORS*, IEEE, Oct. 2017, pp. 1–3, ISBN: 978-1-5090-1012-7.

[29] J. L. Molnar, C. A. Cheng, L. O. Tiziani, B. Boots, and F. L. Hammond, "Optical sensing and control methods for soft pneumatically actuated robotic manipulators," in *Proceedings - IEEE International Conference on Robotics and Automation*, IEEE, May 2018, pp. 3355–3362, ISBN: 9781538630815.

[30] I. M. Van Meerbeek, C. M. De Sa, and R. F. Shepherd, "Soft optoelectronic sensory foams with proprioception," *Science Robotics*, vol. 3, no. 24, eaau2489, Nov. 2018.

[31] L. O. Tiziani and F. L. Hammond, "Optical Sensor-Embedded Pneumatic Artificial Muscle for Position and Force Estimation," *Soft Robotics*, vol. 7, no. 4, pp. 462–477, Feb. 2020.

[32] A. M. Hart, L. O. Tiziani, J. H. Jung, F. L. Hammond, and F. L. H. Iii, "Deformable Reflective Diaphragm Sensors for Control of Soft Pneumatically Actuated Devices," in *IEEE International Conference on Soft Robotics*, IEEE, 2018, pp. 132–139, ISBN: 9781538645161.

[33] C. P. Chou and B. Hannaford, "Measurement and modeling of McKibben pneumatic artificial muscles," *IEEE Transactions on Robotics and Automation*, vol. 12, no. 1, pp. 90–102, 1996.

[34] S. Davis, N. Tsagarakis, J. Canderle, and D. G. Caldwell, "Enhanced modelling and performance in braided pneumatic muscle actuators," *International Journal of Robotics Research*, vol. 22, no. 3-4, pp. 213–227, 2003.

[35] T. Kerscher, J. Albiez, J. M. Zöllner, and R. Dillmann, "Evaluation of the dynamic model of fluidic muscles using quick-release," *Proceedings of the First IEEE/RAS-EMBS International Conference on Biomedical Robotics and Biomechatronics, 2006, BioRob 2006*, vol. 2006, pp. 637–642, 2006.

[36] A. Hošovský, J. Piteľ, K. Židek, M. Tóthová, J. Sárosi, and L. Cveticanin, "Dynamic characterization and simulation of two-link soft robot arm with pneumatic muscles," *Mechanism and Machine Theory*, vol. 103, pp. 98–116, 2016.

[37] R. W. Colbrunn, G. M. Nelson, and R. D. Quinn, "Modeling of braided pneumatic actuators for robotic control," *IEEE International Conference on Intelligent Robots and Systems*, vol. 4, pp. 1964–1970, 2001.

[38] B. S. Kang, C. S. Kothera, B. K. S. Woods, and N. M. Wereley, "Dynamic modeling of mckibben pneumatic artificial muscles for antagonistic actuation," *Proceedings - IEEE International Conference on Robotics and Automation*, pp. 182–187, 2009.

[39] N. Tsagarakis and D. Caldwell, "Improved modelling and assessment of pneumatic muscle actuators," in *Proceedings 2000 ICRA. Millennium Conference. IEEE International Conference on Robotics and Automation. Symposia Proceedings (Cat. No.00CH37065)*, vol. 4, IEEE, 2000, pp. 3641–3646, ISBN: 0-7803-5886-4.

[40] A. Hildebrandt, O. Sawodny, R. Neumann, and A. Hartmann, "Cascaded control concept of a robot with two degrees of freedom driven by four artificial pneumatic muscle actuators," in *Proceedings of the 2005, American Control Conference, 2005.*, 2005, 680–685 vol. 1, ISBN: 0743-1619 VO -.

[41] Y. A. Cengel and J. M. Cimbala, *Fluid Mechanics Fundamentals and Applications, Second Edition*. McGraw-Hill, 2010, ISBN: 139780073529264.

[42] G. K. Klute and B. Hannaford, "Accounting for elastic energy storage in mckibben artificial muscle actuators," *Journal of Dynamic Systems, Measurement and Control, Transactions of the ASME*, vol. 122, no. 2, pp. 386–388, 2000.

[43] C. S. Kothera, M. Jangid, J. Sirohi, and N. M. Wereley, "Experimental characterization and static modeling of McKibben actuators," *Journal of Mechanical Design, Transactions of the ASME*, vol. 131, no. 9, pp. 0 910 101–09 101 010, 2009.

[44] C. Ferraresi, W. Franco, and A. M. Bertetto, "Flexible Pneumatic Actuators: A Comparison between The McKibben and the Straight Fibres Muscles," *Journal of Robotics and Mechatronics*, vol. 13, no. 1, pp. 56–63, 2001.

[45] E. G. Hocking and N. M. Wereley, "Analysis of nonlinear elastic behavior in miniature pneumatic artificial muscles," *Smart Materials and Structures*, vol. 22, no. 1, 2013.

[46] D. B. Reynolds, D. W. Repperger, C. A. Phillips, and G. Bandry, "Modeling the dynamic characteristics of pneumatic muscle," *Annals of Biomedical Engineering*, vol. 31, no. 3, pp. 310–317, Mar. 2003.

[47] G. K. Klute, J. M. Czerniecki, and B. Hannaford, "McKibben artificial muscles: Pneumatic actuators with biomechanical intelligence," *IEEE/ASME International Conference on Advanced Intelligent Mechatronics, AIM*, pp. 221–226, 1999.

[48] K. C. Wickramatunge and T. Leephakpreeda, "Study on mechanical behaviors of pneumatic artificial muscle," *International Journal of Engineering Science*, vol. 48, no. 2, pp. 188–198, Feb. 2010.

[49] R. M. Robinson, C. S. Kothera, R. M. Sanner, and N. M. Wereley, "Nonlinear Control of Robotic Manipulators Driven by Pneumatic Artificial Muscles," *IEEE/ASME Transactions on Mechatronics*, vol. 21, no. 1, pp. 55–68, Feb. 2016.

[50] M. Martens, A. Passon, and I. Boblan, "A sensor-less approach of a torque controller for pneumatic muscle actuator driven joints," in *2017 3rd International Conference on Control, Automation and Robotics (ICCAR)*, 2017, pp. 477–482, ISBN: VO -.

[51] K. M. Lynch and F. C. Park, *Modern Robotics Mechanics, Planning, and Control*. 2017, ISBN: 9781107156302.

[52] M. Raibert, *Legged Robots That Balance*. Cambridge, MA: The MIT Press, 1986, p. 250.

[53] I. Poulakakis, J. A. Smith, and M. Buehler, "Modeling and experiments of untethered quadrupedal running with a bounding gait: The scout II robot," *International Journal of Robotics Research*, vol. 24, no. 4, pp. 239–256, 2005.

[54] J. Pratt and B. Krupp, "Design of a bipedal walking robot," *Unmanned Systems Technology X*, vol. 6962, no. April 2008, 69621F, 2008.

[55] J. W. Grizzle, J. Hurst, B. Morris, H. W. Park, and K. Sreenath, "MABEL, a new robotic bipedal walker and runner," *Proceedings of the American Control Conference*, pp. 2030–2036, 2009.

[56] C. Semini, N. G. Tsagarakis, E. Guglielmino, M. Focchi, F. Cannella, and D. G. Caldwell, "Design of HyQ -A hydraulically and electrically actuated quadruped robot," *Proceedings of the Institution of Mechanical Engineers. Part I: Journal of Systems and Control Engineering*, vol. 225, no. 6, pp. 831–849, 2011.

[57] M. Hutter, C. Gehring, M. Bloesch, M. A. Hoepflinger, C. D. Remy, and R. Siegwart, "Starleth: A compliant quadrupedal robot for fast, efficient, and versatile locomotion," *Adaptive Mobile Robotics - Proceedings of the 15th International Conference on Climbing and Walking Robots and the Support Technologies for Mobile Machines, CLAWAR 2012*, pp. 483–490, 2012.

[58] M. Hutter, C. Gehring, D. Jud, A. Lauber, C. D. Bellicoso, V. Tsounis, J. Hwangbo, K. Bodie, P. Fankhauser, M. Bloesch, R. Diethelm, S. Bachmann, A. Melzer, and M. Hoepflinger, "ANYmal - A highly mobile and dynamic quadrupedal robot," *IEEE International Conference on Intelligent Robots and Systems*, vol. 2016-Novem, pp. 38–44, 2016.

[59] D. W. Haldane, M. M. Plecnik, J. K. Yim, and R. S. Fearing, "Robotic vertical jumping agility via Series-Elastic power modulation," *Science Robotics*, vol. 1, no. 1, 2016.

[60] J. Estremera and K. J. Waldron, "Thrust control, stabilization and energetics of a quadruped running robot," *International Journal of Robotics Research*, vol. 27, no. 10, pp. 1135–1151, 2008.

[61] U. Saranli, M. Buehler, and D. E. Koditschek, "RHex: A simple and highly mobile hexapod robot," *International Journal of Robotics Research*, vol. 20, no. 7, pp. 616–631, 2001.

[62] R. Niiyama, A. Nagakubo, and Y. Kuniyoshi, "Mowgli: A Bipedal Jumping and Landing Robot with an Artificial Musculoskeletal System," in *Proceedings 2007 IEEE International Conference on Robotics and Automation*, 2007, pp. 2546–2551, ISBN: 1050-4729 VO -.

[63] K. Hosoda, Y. Sakaguchi, H. Takayama, and T. Takuma, "Pneumatic-driven jumping robot with anthropomorphic muscular skeleton structure," *Autonomous Robots*, vol. 28, no. 3, pp. 307–316, 2010.

[64] S. Nishikawa, K. Tanaka, K. Shida, T. Fukushima, R. Niiyama, and Y. Kuniyoshi, "A musculoskeletal bipedal robot designed with angle-dependent moment arm for dynamic motion from multiple states," *Advanced Robotics*, vol. 28, no. 7, pp. 487–496, 2014.

[65] M. Li, X. Wang, W. Guo, P. Wang, and L. Sun, "System design of a cheetah robot toward ultra-high speed," *International Journal of Advanced Robotic Systems*, vol. 11, no. 1, pp. 1–11, 2014.

[66] S. Nishikawa, K. Shida, and Y. Kuniyoshi, "Musculoskeletal quadruped robot with Torque-Angle Relationship Control System," *Proceedings - IEEE International Conference on Robotics and Automation*, vol. 2016-June, pp. 4044–4050, 2016.

[67] R. Niiyama and Y. Kuniyoshi, "Design principle based on maximum output force profile for a musculoskeletal robot," *Industrial Robot*, vol. 37, no. 3, pp. 250–255, 2010.

[68] T. Kaneko, M. Sekiya, K. Ogata, S. Sakaino, and T. Tsuji, "Force control of a jumping musculoskeletal robot with pneumatic artificial muscles," in *IEEE International Conference on Intelligent Robots and Systems*, vol. 2016-Novem, Institute of Electrical and Electronics Engineers Inc., Nov. 2016, pp. 5813–5818, ISBN: 9781509037629.

[69] J. Zhong, M. Luo, J. Fan, and J. Zhao, "Trajectory planning of an intermittent jumping quadruped robot with variable redundant and underactuated joints," *Complexity*, vol. 2018, 2018.

[70] E. Todorov, C. Hu, A. Simpkins, and J. Movellan, "Identification and control of a pneumatic robot," in *2010 3rd IEEE RAS and EMBS International Conference on Biomedical Robotics and Biomechatronics, BioRob 2010*, 2010, pp. 373–380, ISBN: 9781424477081.

[71] C. M. Best, M. T. Gillespie, P. Hyatt, L. Rupert, V. Sherrod, and M. D. Killpack, "A New Soft Robot Control Method: Using Model Predictive Control for a Pneumatically Actuated Humanoid," *IEEE Robotics and Automation Magazine*, vol. 23, no. 3, pp. 75–84, 2016.

[72] T. Teramae, T. Noda, and J. Morimoto, "Optimal control approach for pneumatic artificial muscle with using pressure-force conversion model," *Proceed-*

ings - IEEE International Conference on Robotics and Automation, pp. 4792–4797, 2014.

[73] G. K. H. S. L. Das, B. Tondu, F. Forget, J. Manhes, O. Stasse, and P. Soueres, "Performing explosive motions using a multi-joint arm actuated by pneumatic muscles with quasi-DDP optimal control," in *2016 IEEE Conference on Control Applications (CCA)*, Institute of Electrical and Electronics Engineers (IEEE), Oct. 2016, pp. 1104–1110.

[74] Y. Nakamura, I. Karino, S. Mori, K. Tanaka, S. Nishikawa, R. Niiyama, and Y. Kuniyoshi, "Control of pneumatic cylinders using iterative linear quadratic regulator with deep local linear dynamics for explosive motions," in *CLAWAR 2019: 22nd International Conference on Climbing and Walking Robots and the Support Technologies for Mobile Machines*, 2019.

[75] F. Dellaert and M. Kaess, "Factor Graphs for Robot Perception," *Foundations and Trends in Robotics*, vol. 6, no. 1-2, pp. 1–139, 2017.

[76] F. Dellaert, "Factor Graphs and GTSAM: A Hands-on Introduction," Georgia Institute of Technology, Tech. Rep. GT-RIM-CP&R-2012-002, 2012, pp. 1–27.

[77] M. Kelly, "An introduction to trajectory optimization: How to do your own direct collocation," *SIAM Review*, vol. 59, no. 4, pp. 849–904, 2017.

[78] D. Pardo, M. Neunert, A. Winkler, R. Grandia, and J. Buchli, "Hybrid direct collocation and control in the constraint-consistent subspace for dynamic legged robot locomotion," *Robotics: Science and Systems*, vol. 13, 2017.

[79] L. Tiziani, Y. Zhang, F. Dellaert, and F. L. Hammond III, "Factor Graph-Based Trajectory Optimization for a Pneumatically-Actuated Jumping Robot," in *IEEE International Conference on Robotics and Automation (ICRA)*, 2021.

[80] Q. Nguyen, M. J. Powell, B. Katz, J. D. Carlo, and S. Kim, "Optimized jumping on the MIT cheetah 3 robot," *Proceedings - IEEE International Conference on Robotics and Automation*, vol. 2019-May, pp. 7448–7454, 2019.

[81] C. Gehring, S. Coros, M. Hutter, C. Dario Bellicoso, H. Heijnen, R. Diethelm, M. Bloesch, P. Fankhauser, J. Hwangbo, M. Hoepflinger, and R. Siegwart, "Practice Makes Perfect: An Optimization-Based Approach to Controlling Agile Motions for a Quadruped Robot," *IEEE Robotics Automation Magazine*, vol. 23, no. 1, pp. 34–43, 2016.

[82] J. Carius, R. Ranftl, V. Koltun, and M. Hutter, "Trajectory optimization with implicit hard contacts," *IEEE Robotics and Automation Letters*, vol. 3, no. 4, pp. 3316–3323, 2018.

[83] M. Neunert, F. Farshidian, A. W. Winkler, and J. Buchli, "Trajectory Optimization Through Contacts and Automatic Gait Discovery for Quadrupeds," *IEEE Robotics and Automation Letters*, vol. 2, no. 3, pp. 1502–1509, 2017. arXiv: 1607.04537.

[84] M. F. Bobbert, P. A. Huijing, and G. J. van Ingen Schenau, "A model of the human triceps surae muscle-tendon complex applied to jumping," *Journal of Biomechanics*, vol. 19, no. 11, pp. 887–898, 1986.

[85] S. Kurokawa, T. Fukunaga, and S. Fukashiro, "Behavior of fascicles and tendinous structures of human gastrocnemius during vertical jumping," *Journal of Applied Physiology*, vol. 90, no. 4, pp. 1349–1358, 2001.

[86] J. R. Baxter, T. A. Novack, H. van Werkhoven, D. R. Pennell, and S. J. Piazza, "Ankle joint mechanics and foot proportions differ between human sprinters and non-sprinters," *Proceedings of the Royal Society B: Biological Sciences*, vol. 279, no. 1735, pp. 2018–2024, 2012.

[87] A. Nagano and T. Komura, "Longer moment arm results in smaller joint moment development, power and work outputs in fast motions," *Journal of Biomechanics*, vol. 36, no. 11, pp. 1675–1681, 2003.

[88] M. G. Hoy, F. E. Zajac, and M. E. Gordon, "A musculoskeletal model of the human lower extremity: The effect of muscle, tendon, and moment arm on the moment-angle relationship of musculotendon actuators at the hip, knee, and ankle," *Journal of Biomechanics*, vol. 23, no. 2, pp. 157–169, 1990.

[89] M. Millard, T. Uchida, A. Seth, and S. L. Delp, "Flexing computational muscle: Modeling and simulation of musculotendon dynamics," *Journal of Biomechanical Engineering*, vol. 135, no. 2, pp. 1–11, 2013.

[90] M. M. Peplowski and R. L. Marsh, "Work and power output in the hindlimb muscles of Cuban tree frogs Osteopilus septentrionalis during jumping.," *The Journal of Experimental Biology*, vol. 200, no. 22, 2861 LP –2870, Nov. 1997.

[91] T. J. Roberts and R. L. Marsh, "Probing the limits to muscle-powered accelerations: Lessons from jumping bullfrogs," *Journal of Experimental Biology*, vol. 206, no. 15, pp. 2567–2580, 2003.

[92] H. C. Astley and T. J. Roberts, "The mechanics of elastic loading and recoil in anuran jumping," *Journal of Experimental Biology*, vol. 217, no. 24, pp. 4372–4378, 2014.

[93] B. Vanderborght, N. G. Tsagarakis, R. Van Ham, I. Thorson, and D. G. Caldwell, "MACCEPA 2.0: Compliant actuator used for energy efficient hopping robot Chobino1D," *Autonomous Robots*, vol. 31, no. 1, pp. 55–65, 2011.

[94] R. Sato, E. Kazama, A. Ming, M. Shimojo, F. Meng, H. Liu, X. Fan, X. Chen, Z. Yu, and Q. Huang, "Design and control of robot legs with bi-articular muscle-tendon complex," *2017 IEEE International Conference on Robotics and Biomimetics, ROBIO 2017*, vol. 2018-Janua, pp. 2605–2610, 2018.

[95] D. Shin, X. Yeh, and O. Khatib, "Variable radius pulley design methodology for pneumatic artificial muscle-based antagonistic actuation systems," *IEEE International Conference on Intelligent Robots and Systems*, pp. 1830–1835, 2011.

[96] D. A. Winter, "Kinematic and kinetic patterns in human gait: Variability and compensating effects," *Human Movement Science*, vol. 3, no. 1-2, pp. 51–76, 1984.

[97] G. Bovi, M. Rabuffetti, P. Mazzoleni, and M. Ferrarin, "A multiple-task gait analysis approach: Kinematic, kinetic and EMG reference data for healthy young and adult subjects," *Gait and Posture*, vol. 33, no. 1, pp. 6–13, 2011.

[98] J. R. Montgomery and A. M. Grabowski, "The contributions of ankle, knee and hip joint work to individual leg work change during uphill and downhill walking over a range of speeds," *Royal Society Open Science*, vol. 5, no. 8, 2018.

[99] J. Camargo, A. Ramanathan, W. Flanagan, and A. Young, "A comprehensive, open-source dataset of lower limb biomechanics in multiple conditions of stairs, ramps, and level-ground ambulation and transitions," *Journal of Biomechanics*, vol. 119, p. 110 320, 2021.

[100] F. C. Anderson and M. G. Pandy, "Storage and utilization of elastic strain energy during jumping," *Journal of Biomechanics*, vol. 26, no. 12, pp. 1413–1427, 1993.

[101] A. J. van Soest, A. L. Schwab, M. F. Bobbert, and G. J. van Ingen Schenau, "The influence of the biarticularity of the gastrocnemius muscle on vertical-jumping achievement," *Journal of Biomechanics*, vol. 26, no. 1, pp. 1–8, 1993.

[102] J. J. Visser, J. E. Hoogkamer, M. F. Bobbert, and P. A. Huijing, "Length and moment arm of human leg muscles as a function of knee and hip-joint angles," *European Journal of Applied Physiology and Occupational Physiology*, vol. 61, no. 5-6, pp. 453–460, 1990.

[103] F. E. Zajac, "Muscle Coordination of Movement: A Perspective," *Journal of Biomechanics*, vol. 26, no. 1, pp. 109–124, 1993.

[104] P. Aerts, "Vertical jumping in Galago senegalensis: The quest for an obligate mechanical power amplifier," *Philosophical Transactions of the Royal Society B: Biological Sciences*, vol. 353, no. 1375, pp. 1607–1620, 1998.

[105] K. Kubo, Y. Kawakami, and T. Fukunaga, "Influence of elastic properties of tendon structures on jump performance in humans," *Journal of Applied Physiology*, vol. 87, no. 6, pp. 2090–2096, 1999.

[106] J. Aguilar, A. Lesov, K. Wiesenfeld, and D. I. Goldman, "Lift-off dynamics in a simple jumping robot," *Physical Review Letters*, vol. 109, no. 17, pp. 1–5, 2012. arXiv: 1208.6289.

[107] T. Takuma, S. Hayashi, and K. Hosoda, "3D bipedal robot with tunable leg compliance mechanism for multi-modal locomotion," *2008 IEEE/RSJ International Conference on Intelligent Robots and Systems, IROS*, pp. 1097–1102, 2008.

[108] D. Sulistyoutomo, S. Nishikawa, R. Niiyama, and Y. Kuniyoshi, "Sequential Jumping-Stepping Motion on Musculoskeletal Humanoid Robot for Agile Locomotion," *2018 IEEE International Conference on Robotics and Biomimetics, ROBIO 2018*, pp. 2328–2333, 2018.

[109] S. Seok, A. Wang, M. Y. Chuah, D. Otten, J. Lang, and S. Kim, "Design principles for highly efficient quadrupeds and implementation on the MIT Cheetah robot," *Proceedings - IEEE International Conference on Robotics and Automation*, pp. 3307–3312, 2013.

[110] R. F. Shepherd, A. A. Stokes, J. Freake, J. Barber, P. W. Snyder, A. D. Mazzeo, L. Cademartiri, S. A. Morin, and G. M. Whitesides, "Using explosions to power a soft robot," *Angewandte Chemie - International Edition*, vol. 52, no. 10, pp. 2892–2896, 2013.

[111] M. Wehner, M. T. Tolley, Y. Mengüç, Y. L. Park, A. Mozeika, Y. Ding, C. Onal, R. F. Shepherd, G. M. Whitesides, and R. J. Wood, "Pneumatic Energy Sources for Autonomous and Wearable Soft Robotics," *Soft Robotics*, vol. 1, no. 4, pp. 263–274, 2014.

[112] M. T. Tolley, R. F. Shepherd, M. Karpelson, N. W. Bartlett, K. C. Galloway, M. Wehner, R. Nunes, G. M. Whitesides, and R. J. Wood, "An untethered jumping soft robot," in *IEEE International Conference on Intelligent Robots and Systems*, IEEE, 2014, pp. 561–566, ISBN: 9781479969340.

[113] C. D. Onal, X. Chen, G. M. Whitesides, and D. Rus, "Soft mobile robots with on-board chemical pressure generation," *Springer Tracts in Advanced Robotics*, vol. 100, pp. 525–540, 2017.